Investigation of the structure and properties of

$(K_xNa_{1-x})NbO_3$-based piezoelectric ceramics using both conventional and high-throughput experimentation (HTE) methods

Vom Promotionsausschuss der
Technischen Universität Hamburg-Harburg
zur Erlangung des akademischen Grades
Doktor-Ingenieur (Dr.-Ing.)
genehmigte Dissertation

von
Henry Ekene Mgbemere (M.Sc)
aus
Mbano, Nigeria

Hamburg 2012

1. Gutachter:	Prof. Dr. rer. nat. Gerold A. Schneider
2. Gutachter:	Prof. Dr. rer. nat. Michael J. Hoffmann

Tag der mündlichen Prüfung: 12.06.2012

Danksagung / Acknowledgement

The contents of this report are based on the research work that was carried out during my stay as a research assistant at the Institute of Advanced Ceramics, Technische Universität Hamburg-Harburg in Germany.

I would like to express my sincere gratitude to Prof. Dr. rer. nat. Gerold A. Schneider, my project supervisor for giving me the opportunity to do this work in his research group. I would also like to thank him for his scientific guidance and encouragement while also giving me the freedom to develop my research skills during this period.

Special thanks also to Prof. Dr. rer. nat. Michael J. Hoffmann for accepting to be my second supervisor.

I am equally grateful to both my colleagues and students at the Institute for the excellent working environment throughout the period of this work. Your friendly nature and help made my stay during this period a happy and fruitful one. Special thanks to Dr. Ing. Manuel Hinterstein, the instrument contact person at the beamlime B2 of the synchrotron facility "DESY/HASYLAB" in Hamburg for his help and collaboration in acquiring the synchrotron diffraction data, analysis, interpretation of the results and other useful suggestions.

I would also like to thank my Nigerian friends in Hamburg and around the world for their encouragement and sound advice about how to survive and achieve something worthwhile in a foreign land. I would like to thank my brothers and sisters and the entire Mgbemere family members for their encouragement throughout the period of this work.

Finally, I would like to thank my wife *Akudo* for her patience and encouragement especially during the final stages of this work.

Table of Contents

Symbols and Abbreviations

d_{33}	Piezoelectric charge coefficient (from low signal measurement)
d^*_{33}	Piezoelectric charge coefficient (from high signal measurement)
ε_o	Permittivity of free space (8.85×10^{-12} F/m)
ε_r	Relative dielectric constant/Permittivity
D_i	Dielectric displacement
χ	Dielectric susceptibility
P	Polarization
E	Electric field
Tj_k	Stress
S_{ij}	Strain
k	Coupling constant
T_c	Curie temperature
$T_{r\text{-}o}$	Rhombohedral to orthorhombic phase transition temperature
$T_{T\text{-}O}$	Tetragonal to orthorhombic phase transition temperature
N_P	Frequency constant
P_s	Saturation polarization
P_r	Remanent polarization
S_r	Remanent strain
d_{ijk}	Piezoelectric charge coefficient (in tensor notation)
t	Tolerance factor
A	Surface area of the sample
d	Distance between the electrodes
C	Capacitance

W_P	Weight fraction of the phases
β	Pseudo-monoclinic angle
E_c	Coercive field
Q_m	Quality mechanical factor
tan δ	Dielectric loss
f_a, f_r	Antiresonance and resonance frequency respectively
G.O.F	Goodness of fit
R_p	Profile factor
R_{wp}	Weighed profile factor
R_{exp}	Expected refinement profile factor
χ^2	Chi square test
σ	Electrical conductivity
J	Angular frequency
C_m	Measured capacitance
P	Density
V	Volume
a_{pc}	Psedo-cubic cell parameter
η	Lattice distortion parameter
a, b, c	Lattice parameters of the unit cell
MPB	Morphotropic phase boundary
PPT	Polymorphic phase transition
HTE	High-throughput experimentation
OES/ICP	Optical emission spectroscopy/Inductive coupled plasma
EDX	Energy dispersive spectroscopy
PDF	Powder diffraction file
SEM	Scanning electron microscope
XRD	X-ray diffraction

1 Introduction

Lead zirconate titanate (PZT) based piezoelectric ceramics are currently the most used for manufacturing actuators, sensors, resonators, transducers and other electromechanical devices due to a combination of excellent piezoelectric properties, wider operating temperature range and a variety of other characteristics [1].

The major component for these piezoelectric ceramics which contributes about 60 wt% is the element lead (Pb). It is a soft element which is classified as a heavy metal and is also toxic. It has been used from as far back as the second century B.C in Rome when lead (II)-acetate [($Pb(CH_3COO)_2$] was used for making wine because of its sweet flavor. Its harmful effects have been known for a long time ago because most of the deaths at the time were traced to it. Children are more susceptible to Pb attacks than adults because their central nervous system is more vulnerable. Lead has the ability to attach itself strongly to sulfhydryl group on proteins and distort the enzymes and structural proteins. It can also cleave to the ribophosphate backbone of transfer Ribonucleic acid (tRNA) catalytically with no evidence of a threshold and mimics or competes with calcium in the body. Some of the consequences of lead poisoning for children include; behavioral disorders, learning difficulties, low intelligence quotient etc. while hypertension and renal failure are some of the consequences of acute lead poisoning. Some of the sources of exposure to lead include leaded dishware, lead workers, electronics, paints, cosmetics etc. Recent studies indicate that there is no threshold for lead but 10µg/dL is seen to be the acceptable blood levels. The primary way of prevention is the avoidance of contact with leaded materials [2].

Considering all these health problems posed by using lead-containing materials, multinational governments like the European parliament have enacted laws that ban their use for manufacturing many products [3]. Other governments are either considering similar laws or tightening controls on how these toxic materials can be used. In the field of electronic ceramics, concessions which will soon be subject to review were made because

the lead-free ferroelectric replacements still have inferior piezoelectric and electromechanical properties compared to those of lead-based ceramics.

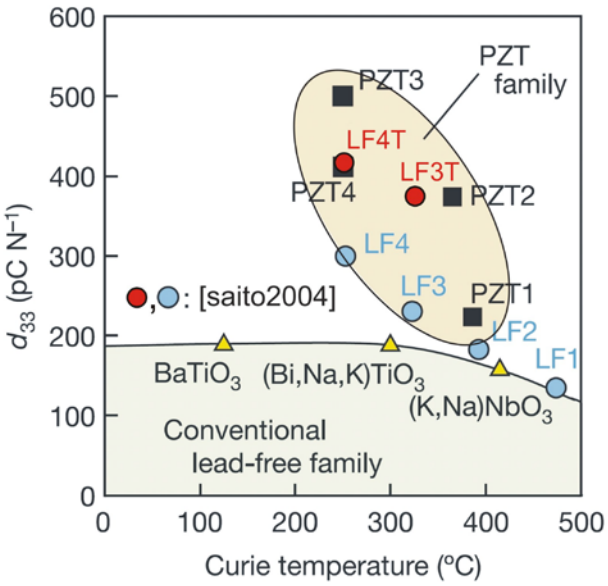

Fig 1.1 Comparison of the piezoelectric charge coefficient d_{33} at 25 °C among lead-free (LF) ceramics and conventional PZT ceramics as a function of Curie temperature [4].

Research on lead-free piezoelectric ceramics has been on-going for more than 50 years but in the last 10 years, there has been more interest on the subject such that more than 75 % of all published works in the field have been reported in this period. The lead-free piezoelectric ceramics being researched on include $(Bi_{0.5}Na_{0.5})TiO_3$ based ceramics [5], tungsten bronze ceramics [6], bismuth layered titanates ceramics [7] and $(K_xNa_{1-x})NbO_3$ based ceramics [8]. $(K_xNa_{1-x})NbO_3$ abbreviated as KNN which is a solid solution of ferroelectric $KNbO_3$ and antiferroelectric $NaNbO_3$ appears to be among the most promising because of its comparably high piezoelectric properties, large electromechanical coupling coefficients and high Curie temperature (≈ 420 °C) [8]. The graph in Fig. 1.1 shows a comparison of the piezoelectric charge coefficient (d_{33}) values as a function of Curie temperature for lead-free piezoelectric ceramics and selected lead-based piezoelectric ceramics. It is clear that the d_{33} values close to those containing lead and are even better when the samples are textured. The improvement in the piezoelectric properties of these KNN ceramics is attributed to the introduction of other elements in the form of dopants which leads to phase coexistence and increases the total number of possible polarization

directions. KNN modified with Li, Ta and Sb which was reported by Saito et al. [4] has one of the highest piezoelectric properties for lead-free ceramics. This was initially attributed to the existence of a morphotropic phase boundary (MPB) but later reports have shown that the increase in the piezoelectric activity is closely related to the decrease in the phase transition temperatures. The term “polymorphic phase transition” (PPT) was considered to be more appropriate.

Theoretical materials science has made very big progress in the last couple of years but experimental materials science will continue to be essential for discovering new promising compositions in a couple of years to come. This is because the complexity of material compositions currently being studied requires that more computing infrastructure than presently available is needed [9]. The one at a time approach used in conventional ceramics processing though necessary is a slow method to discover new promising material compositions and so a faster method which applies robotics called “High-throughput experimentation” (HTE) has been introduced. It has been defined as “the use of miniaturization, robotics and parallel techniques to increase the productivity of the research process while the screening/analysis involves using a parallel characterization technique to rapidly asses the properties of the samples produced through this process” [10]. The need to discover new material compositions with better properties while also limiting the amount of raw materials and time used is the driving force for this new process [11]. This process was first used in pharmaceutical research but is now also used for materials research like polymers [11] and catalysts [12]. It has been used for research on thin film-based ceramics [13] and even bulk ceramics [14, 15] where certain properties like the piezoelectric coefficient (d_{33}), doping effects, grain size effects are better determined using samples in their bulk form.

Synchrotron radiation has revolutionized X-ray diffraction of crystalline substances. The ability to select wavelengths, as well as moving one of the diffractometer angles makes it possible to exploit anomalous scattering for phase determination. The experimental setup is flexible and can be adjusted to measure substances over a wide range of temperatures. Because new synthesized lead-free ceramics cannot be unambiguously characterized by standardized X-ray diffraction data, synchrotron radiation offers the possibility to analyse the crystal structures of the new materials in detail.

The objective of this research work was to investigate into the structure and properties of of KNN-based ceramics. The strategy applied here is to use multiple sites doping to improve the properties of KNN ceramics and it is explained in detail in chapter 3.2. High resolution X-rays were used to determine the structure of modified KNN ceramics.

2 Fundamentals

2.1 Foreword

The interaction between two different atoms with both positive and negative charges can be used to explain polarization in a dielectric material. Due to this interaction between the opposing charges, an electric dipole moment is established. When an electric field is applied, this dipole moment $\vec{p}$ will orient with the applied field thereby deforming the electron clouds and this alignment phenomenon is called polarization.

The main polarization mechanisms which can occur within a dielectric material include electronic polarization, ionic polarization, orientation polarization, space charge polarization and domain wall polarization. Electronic polarization is based on the displacement of the negatively charged electron shell against the positively charged core; ionic polarization describes the displacement of the positive and negative sublattices with an applied field; orientational polarization which deals with alignment of permanent dipoles; space charge polarization is caused by accumulation of mobile charges at the interfaces and surfaces of materials; domain wall polarization occurs in ferroelectric materials.

Dielectric ceramic materials are divided into single crystals, thin films, thick films and bulk polycrystalline ceramics. Single crystal concepts are well developed and will be used to describe some piezoelectric concepts but this work is concerned only with bulk polycrystalline ceramics.

Crystals are classified into 32 point groups based on their symmetry. These 32 point groups are subdivisions of 7 basic crystal systems that in ascending order of symmetry include; triclinic, monoclinic, orthorhombic, tetragonal, rhombohedral (trigonal), hexagonal, and cubic. These point groups are divided into two classes which include those with a center of symmetry and those without. There are 21 non-centrosymmetric point groups, 20 (except point group *432*) of which exhibit piezoelectricity. Of the 20 point groups, 10 of the crystal classes contain a unique axis where the dipole moment is oriented in the unstrained condition i.e. they exhibit spontaneous polarization.

Crystals whose direction of spontaneous polarization can be reversed by the application of an external electric field are called ferroelectrics. There are basically four different types of ferroelectric ceramics. They include the tungsten–bronze group (AB_2O_6), the oxygen octahedral group (ABO_3), the pyrochlore group ($A_2B_2O_7$), and the bismuth layer–structure group ($A_4B_3O_{12}$). The main difference between these ceramics lies in the structure of their respective unit cells. The oxygen octahedral group (ABO_3 type) which has the perovskite structure is the most important economically and will be further discussed in this report. The ABO_3 type ferroelectric ceramics are further divided into $BaTiO_3$, $Pb(Zr_xTi_{1-x})O_3$, $(Bi_{0.5}Na_{0.5})TiO_3$ and $(K_xNa_{1-x})NbO_3$ family of compositions [16].

2.2 Dielectric constant and loss

When an electric field is applied to a dielectric material, partial charge compensation is achieved by polarization. Polarization $\vec{P}$ is defined as the sum of all dipole moments ($\vec{p}$) per unit volume (V) and is represented with equation 2.1

$$\vec{P} = \frac{\sum_i \vec{p}_i}{V} \tag{2.1}$$

When a dielectric material is located between the plates of a capacitor, the capacity of the capacitor C is increased by a factor ε_r which is the dielectric constant or relative permittivity of the material. The relationship between the capacitance C and ε_r is shown in equation 2.2

$$C = \varepsilon_o \varepsilon_r \frac{A}{d} \tag{2.2}$$

where ε_o is the permittivity of free space (8.85 x 10^{-12} F/m), ε_r is the relative permittivity, A is the surface area of the sample and d the distance between the electrodes

This increase in the capacitance is due to the polarization of the material due to the applied field $\vec{E}$. The higher the field applied, the higher is the distorting force of the dipoles such that the dielectric polarization is proportional to the applied field. The constant of proportionality here is called electric susceptibility χ and is a measure of how easily the dielectric material polarizes in response to the electric field. It is related to the polarization in the material with equation 2.3

$$\vec{P} = \chi \varepsilon_0 \vec{E} \tag{2.3}$$

The total amount of charges stored in a capacitor is a combination of the polarization charge and the charge without a dielectric.

The loss tangent of a dielectric material quantifies its inherent dissipation of electromagnetic energy. When the voltage is alternating, the charge stored in a dielectric material has both real (in phase) and imaginary (out of phase) components as a result of resistive leakage or dielectric absorption [17]. The dielectric loss or dissipation factor ($\tan\delta$) is the ratio of the imaginary component (ε'') to the real component (ε') in an a.c circuit. Mathematically it is represented with equation 2.4

$$\tan\delta = \frac{\varepsilon''}{\varepsilon'} \tag{2.4}$$

For polycrystalline ceramics, there are possible contributions of conductivity to the value of the loss tangent. The conduction loss is due to flow of charge through the material while the dielectric loss is due to movement of charges due to changes in polarization direction [18]. When there is a substantial contribution of conduction loss, the loss tangent can be calculated through the relation in equation 2.5

$$\tan\delta = \frac{\sigma}{J\varepsilon'} \tag{2.5}$$

Where σ represents the electrical conductivity and J represents the angular frequency.

2.3 The piezoelectric effect

When some crystals are subjected to stress in certain directions, they develop positive and negative charges at opposite ends. This phenomenon is called piezoelectric effect and was discovered by the Curie brothers in 1880. Some crystals undergo dimensional changes when subjected to an electric field and this phenomenon is called converse piezoelectric effect [19]. This occurrence is a thermodynamic consequence of the piezoelectric effect. Some of the earliest discovered piezoelectric crystals include; quartz, tourmaline and Rochelle salt. A necessary condition for piezoelectricity is the absence of a center of symmetry and from a chemical point of view, chemical bonds between the atoms in the crystal must be heteropolar [20]. A schematic representation of the direct and converse piezoelectric effect is shown in Fig. 2.1. For a single crystal, these polar axis lie in one direction while in a polycrystal, different regions within the material have different polar axes.

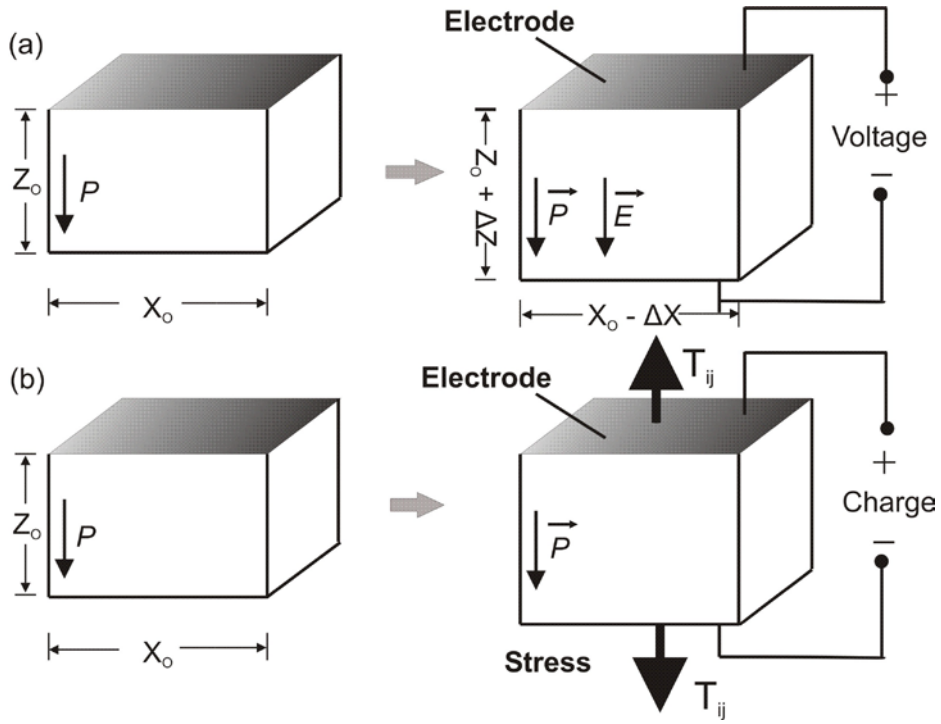

Fig. 2.1 Schematic representations of the direct and inverse piezoelectric effect: (a) an electric field $\vec{E}$ applied to the material changes its shape; (b) a stress on the material yields to surface charges.

The direct piezoelectric effect can be represented in Tensor notation by equation 2.6.

$$P_i = d_{ijk} T_{jk} \tag{2.6}$$

$$S_{ij} = d_{kij} E_k \tag{2.7}$$

where P_i is the polarization generated along the *i*-axis direction in response to the stress T_{jk} while d_{ijk} is the piezoelectric coefficient. The formula for the converse piezoelectric effect is shown in equation 2.7 and describes the induced strain (S_{ij}) which is proportional to an applied electric field (E_k). The proportionality constant (d_{ijk}) is identical in both cases and is called the piezoelectric coefficient with units (C/N or m/V) [17]. The piezoelectric coefficient is a third rank tensor which implies that it has 27 components and therefore complex. To simplify things, the matrix notation is normally used to replace the tensor notation and consequently reduce the number of components to 18.

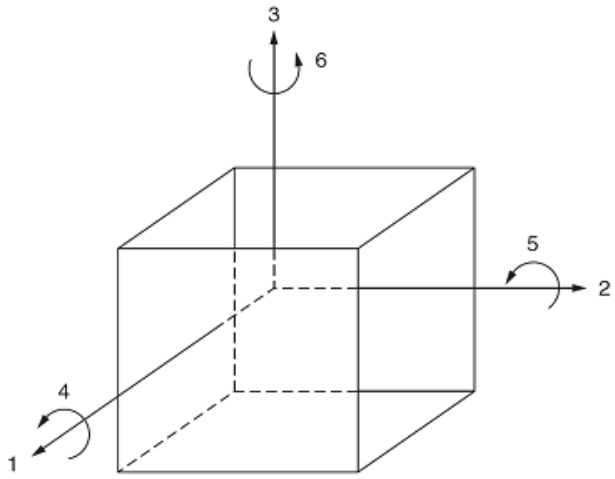

Fig. 2.2 Notation of axis and direction of deformation.

The reference axis for representing the properties of crystals in the *x*, *y* and *z* component is shown in Fig. 2.2. To simplify the resulting equation, the tensor notation is replaced with the matrix notation as shown in Table 2.1.

Table 2.1 Replacing the tensor notation of crystals with matrix notation

Tensor (ij or jk)	11	22	33	23 or 32	31 or 13	12 or 21
Matrix (i or j)	1	2	3	4	5	6

The conditions used in changing the tensor notation to matrix notation are;

$d_{ijk} \equiv d_{ij}$ *if* $j = k = 1, 2$ *or* 3

$d_{ijk} + d_{ikj} \equiv d_{ij}$ *if* $j = 4, 5,$ *or* 6

Equations 2.6 and 2.7 now become

$$P_i = d_{ij} T_j . \tag{2.8}$$

$$S_j = d_{ij} E_i . \tag{2.9}$$

The convention is that the subscript *i* in equations 2.8 and 2.9 indicate the *z* axis or 3 which is perpendicular to the plane of the electrodes and the subscribt *j* the direction of the applied stress or piezoelectrically induced strain [21]. The piezoelectric coefficient (d_{33}) is easier to measure in polycrystalline ceramics and will be used mainly in this report.

2.4 Ferroelectricity

A material is said to be ferroelectric if it possesses spontaneous polarization whose direction can be reversed by the application of an external electric field within a certain temperature range. Another characteristic feature of ferroelectrics is the presence of domains which is the orientation of dipole moments within the grains of the material.

2.4.1 Domains

Spontaneous polarization in a material is as a result of small displacements of positive ions in one direction and negative ions in the the opposite direction which creates a net dipole moment in the unit cell. A ferroelectric domain is a region in a ferroelectric crystal that exhibits homogenous and spontaneous polarization [22]. The symmetry of the unit cell determines the directions of spontaneous polarization within each domain and is limited to a small number of directions. The boundary region between two ferroelectric domains is called a domain wall. For a single crystal with tetragonal structure, there are two possible domain orientations (90° and 180°) as shown in Fig. 2.3. 180° domains mainly occur to minimize both the surface charge density and free energy of the system when the material is polarized while 90° domains form to minimize stresses within the grains during phase transition [21]. The domain structure in polycrystalline ceramics is complex and consists of many domains each with different polarization orientation.

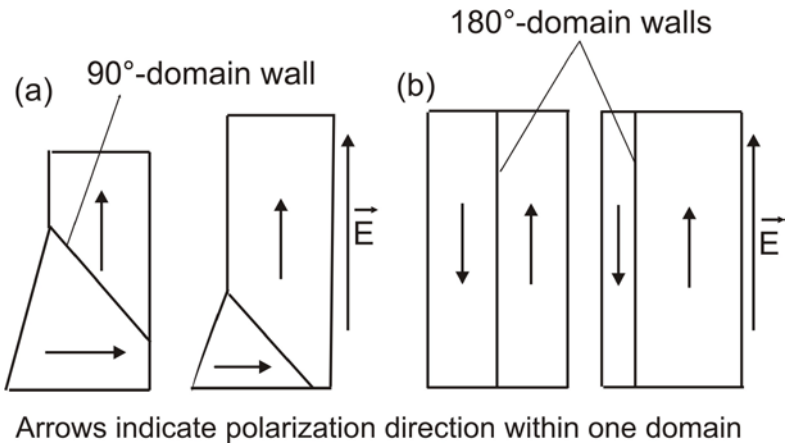

Fig. 2.3 Ferroelectric behavior in a single crystal: When applying an electric field, the growth of favorably orientated domains is supported at the expense of non-favorable domains (a) case of 90°-domains (b) case of 180°-domains.

2.4.2 Poling of ferroelectrics

Polycrystalline ceramics have crystallites which are randomly oriented giving rise to zero net polarization. Fig. 2.4a is a schematic of the orientation of crystallites in the unpoled state.

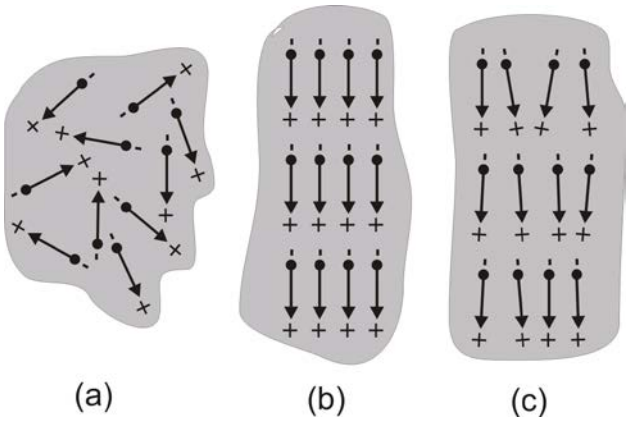

Fig. 2.4 Crystallite orientation at the: (a) initial state, (b) re-orientation of the crystallites after poling, (c) on removing the electric field, some crystallites revert to more energetically favourable positions.

Poling of ferroelectrics involves the application of a direct current electric field which is higher than the coercive field of the material to obtain a net remanent polarization. It is mainly applied at elevated temperatures to enhance the alignment of the domains in the field direction. A complete orientation in the direction of the field is shown in Fig. 2.4b. When the applied field is removed, most of the crystallites remain in their imposed direction while others try to return to more energetically favourable positions (Fig. 2.4c). Electrodes are applied on the surfaces of the samples for the poling process to be successful. Poling is also necessary for single-crystal ferroelectric bodies because they contain a multiplicity of randomly oriented domains [23].

2.4.3 Ferroelectric hysteresis

The most commonly accepted feature of ferroelectricity is the dielectric hysteresis which shows the nonlinearity in the relation between the polarization $\vec{P}$ and the applied electric field $\vec{E}$. Dielectric displacement $\vec{D}$ is approximately equal to polarization and is the physical quantity that corresponds to the stored electric charge per unit area. It is related to the electric Field $\vec{E}$ by the expression in equation 2.10 in plane capacitor geometry.

$$\vec{D} = \frac{Q}{A} = \frac{C_m U_m}{A} = \varepsilon_o \vec{E} + \vec{P} \approx \vec{P} \tag{2.10}$$

Where Q is the charge on the capacitor, A is the surface area of the capacitor; C_m is the reference capacitance and U_m is the measured voltage.

When an electric field is applied to a ferroelectric material, the dipoles begin to align with the field. Saturation polarization P_s is reached when there is no further increase in polarization with increasing field. If the field is reduced to zero, the polarization will decrease but will not fall back to zero rather to a value lower than P_s known as the remanent polarization P_r. To reduce the value of polarization to zero, it is necessary to apply a field in the opposite direction. The field at which polarization is zero is called the coercive field E_c. If the field is further increased in the opposite direction, it will reach saturation polarization P_s. When the electric field is reduced again to zero, there is remanent polarization P_r but in the negative direction. Further increase of the field will bring the polarization back to P_s. A schematic representation of the experimental setup for hysteresis measurement is shown in Fig. 2.5a while a typical polarization-field hysteresis curve is shown in Fig. 2.5b.

The strain hysteresis loop can also be observed when the material is subjected to electric field. A typical strain hysteresis loop is shown in Fig. 2.5c and the characteristic parameter is the remanent strain S_r. The strain at each point is determined from the ratio of the elongation to that of the sample thickness.

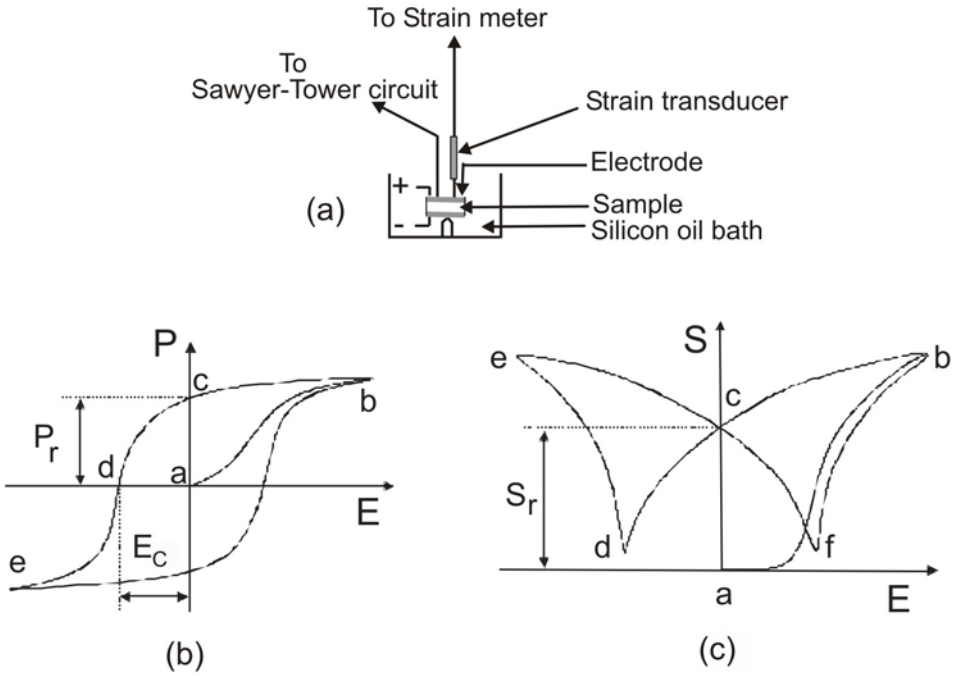

Fig. 2.5 Schematic representation of (a) experimental setup for hysteresis measurement (b) polarization-field hysteresis curve and (c) strain-field hysteresis curve (also called Butterfly loop). The alphabets a, b, c, d and e represent different orientations of the domains as the electric field is applied.

2.4.4 Role of defects in ferroelectrics

An understanding of the effect of adding dopants to ferroelectric ceramics has not been well understood and is still a matter of research. Donor dopants are those elements which have higher valency charge than the elements they are to replace while acceptor dopants are those with lower valency than those to be replaced. Isovalent dopants have the same charge with the element to be replaced. In $BaTiO_3$ ceramics, donor and acceptor dopants introduce defects to the lattice which can be explained using the Kröger-Vink notation as shown in equations 2.11-2.13.

$$La_2O_3 \xrightarrow{3BaTiO_3} 2La_{Ba}^{\bullet} + 3O_O^{\times} + V_{Ba}^{''} \tag{2.11}$$

$$La_2O_3 \xrightarrow{2BaTiO_3} 2La_{Ba}^{\bullet} + \frac{1}{2}O_2(g)\uparrow + 2e' + 2O_O^{\times} \tag{2.12}$$

$$Al_2O_3 \xrightarrow{2BaTiO_3} 2Al_{Ti}^{'} + 3O_O^{\times} + V_O^{\bullet\bullet} \tag{2.13}$$

where the superscripts "•", " ´ " and "×" represent an excess charge, a negative charge and a neutral charge respectively.

When La is used to replace Ba on the A-site of the lattice, it acts as a donor dopant and leads to the creation of cation vacancies (equation 2.11). Another possibility could be the injection of electrons into the lattice (equation 2.12). The symmetry of the lattice is altered by this valence defect and this implies that certain possible orientations of the spontaneous polarization will be preferred locally. The appearance of Frenkel type interstitial dopants appears less likely in a perovskite lattice based on atomistic simulation which showed that interstitials are energetically unfavourable [24]. Donor doping as for example $La_{Ba}^{\bullet}$ leads to soft ferroelectric properties which are characterized by high values of permittivity, dielectric loss and mechanical loss with low coercive field due to easy mobility of the domain wall.

When Al is used to replace Ti on the B-site, it acts as an acceptor dopant and leads to the creation of oxygen vacancies as shown in equation 2.13. Acceptor doping for instance $Al_{Ti}^{\prime}$ leads to hard ferroelectric properties which are characterized by reduced domain wall mobility, low values of dielectric constant and loss and increase in both mechanical quality factor and the coercive field. Softening and hardening also depend on the crystal structure and unintentional doping through impurities or defects which can form at high sintering temperatures. A table showing the possible donors and acceptors that can be used to dope $BaTiO_3$ is shown in Table 2.2

Table 2.2 Common aliovalent substituents for $BaTiO_3$ ceramics

A-site donors	La^{3+}, Bi^{3+}
B-site donors	Nb^{5+}, Ta^{5+}, Sb^{5+}
A-site acceptors	K^{+}, Rb^{+}
B-site acceptors	Co^{3+}, Fe^{3+}, Sc^{3+}, Ga^{3+}, Cr^{3+}, Mn^{3+}, Mn^{2+}, Mg^{2+}, Cu^{2+}

2.4.5 Antiferroelectricity

Antiferroelectric crystals have zero net switchable dipole moment per unit cell, and consequently exhibit no macroscopic polarization hysteresis in their low-signal polarization versus electric field characteristics as shown in Fig. 2.6 [22]. Some have a high dielectric constant peak and even obey the Curie-Weiss law above the inversion point (when $T > T_c$) but are non-polar below that inversion. Kittel [25] postulated that an antiferroelectric is a material whose subcells have a polar arrangement but the adjacent

cells are oppositely polarized leading to a zero net polarization and a center of symmetry. If a high enough electric field is applied as shown in Fig. 2.6, ferroelectric-antiferroelectric phase transition is observed with E_a and E_f representing decreasing and increasing field respectively. $PbZrO_3$ is a typical antiferroelectric material and the arrangement is anti-polar in two directions however, a net polarity is reported for the third direction.

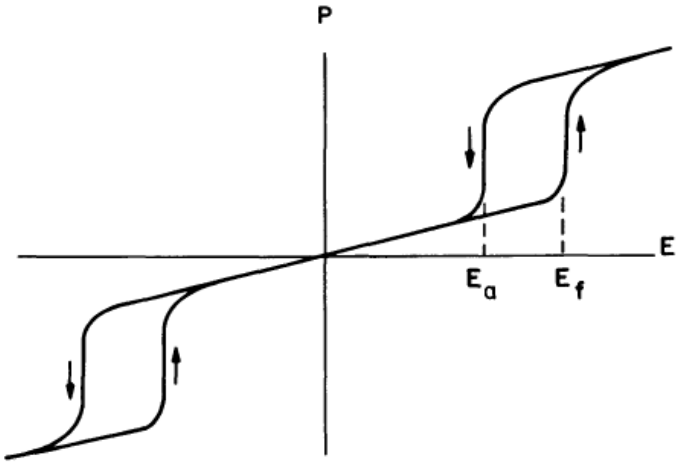

Fig. 2.6 Polarization-Electric field characteristic for an antiferroelectric material [22].

2.5 The Perovskite structure

The perovskite structure named after the mineral $CaTiO_3$ is the most important structure for ferroelectric materials. It has the general formula, ABO_3 and a typical unit-cell structure is shown in Fig. 2.7. The A-site is occupied by Ca while the octahedral sites are occupied by the corner sharing O. Ti occupies the B-site which is the center of the unit cell. In an ideal cubic perovskite structure, the atoms are just touching one another. For a material to be classified as having the perovskite structure, Goldschmidt [26] postulated that the relation in equation 2.13 needs to be satisfied

$$t = \frac{\left(R_A + R_O\right)}{\sqrt{2}\left(R_B + R_O\right)} \tag{2.13}$$

where R is the radius of the atom and *t* is the tolerance factor. *t* is equal to 1 for an ideal structure but the tolerance limit is between $0.75 \leq t \leq 1.05$.

2.6 Temperature dependent phase transformation

Changes in temperature significantly affect the properties of a material due to the effect of heat on orientational polarization. There is a transition temperature above which ferroelectric materials are non-polar and below which they are polar. This temperature is called the Curie temperature T_c. This transition temperature will be illustrated with the Perovskite structure shown in Fig. 2.7. Above the T_c, the sample is cubic in structure and non-polar and below the T_c, the material develops polarization. When an electric field is applied to the unit cell, the central atom (Ti) is displaced in the direction of the field. The crystallites are randomly distributed and the individual ionic movements which take place leads to polarization. The direction of polarization in the material will depend on the crystal structure present. For a tetragonal structure it is [001], [101] for an orthorhombic structure and [111] for a rhombohedral structure.

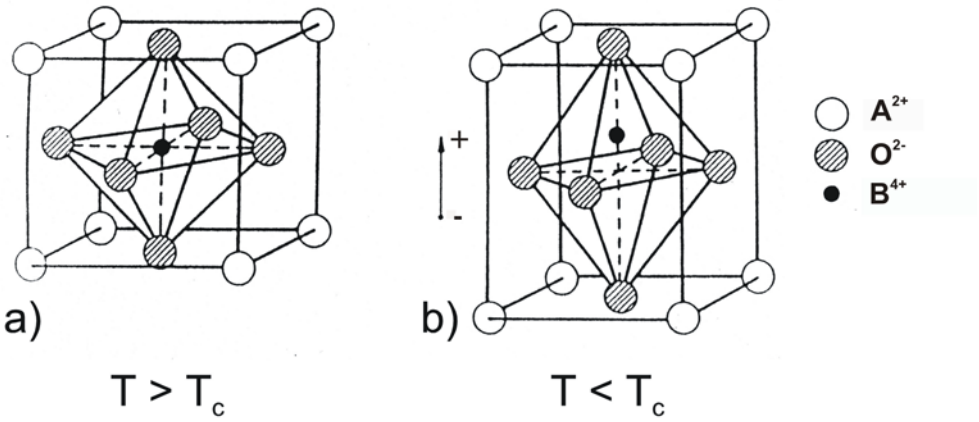

Fig. 2.7 Schematic representation of the Perovskite lattice (ABO_3) for (a) a cubic unit cell and (b) a tetragonal unit cell.

Most ferroelectric materials obey the Curie-Weiss law and the relationship between the dielectric constant and T_c is shown in equation 2.14 where C is the Curie constant.

$$\varepsilon_r - 1 = \frac{C}{T - T_c} \tag{2.14}$$

Discontinuities in the dielectric, elastic and piezoelectric properties of ferroelectric materials are indications of the phase changes taking place. Some of these discontinuities occur at the T_c of these materials and at this temperature, the coupling factors and polarization due to poling are reduced to zero. At the ferroelectric-ferroelectric transition,

two structures are equally stable and the dipoles have more degrees of freedom than with one structure alone.

Fig. 2.8 shows the temperature dependent phase transitions that take place in a $BaTiO_3$ crystal. The phase transitions are of first order leading to discontinuities in polarization, lattice constants, relative permittivity and other properties. Upon cooling of the crystal, 3 phase transitions occur and the sequence is from cubic to tetragonal phase; from tetragonal to orthorhombic and finally from orthorhombic to the rhombohedral phase. Thermal hysteresis could also be observed at the phase transition regions and these depend on parameters like the rate of temperature change, crystal imperfections, stresses etc [18].

At the Curie temperature, the polarization in the crystal drops to zero while the dielectric constant reaches its peak value. $(K_xNa_{1-x})NbO_3$ ceramics also undergo similar series of phase transitions just like in $BaTiO_3$. The properties of $BaTiO_3$ are highly anisotropic as shown in the dielectric constant values for crystals with a-axis (ε_a) and c-axis orientation (ε_c) (Fig. 2.8c). The properties are better with certain crystallographic orientations than with others but the phase transition temperature remains the same regardless of orientation or the property being measured.

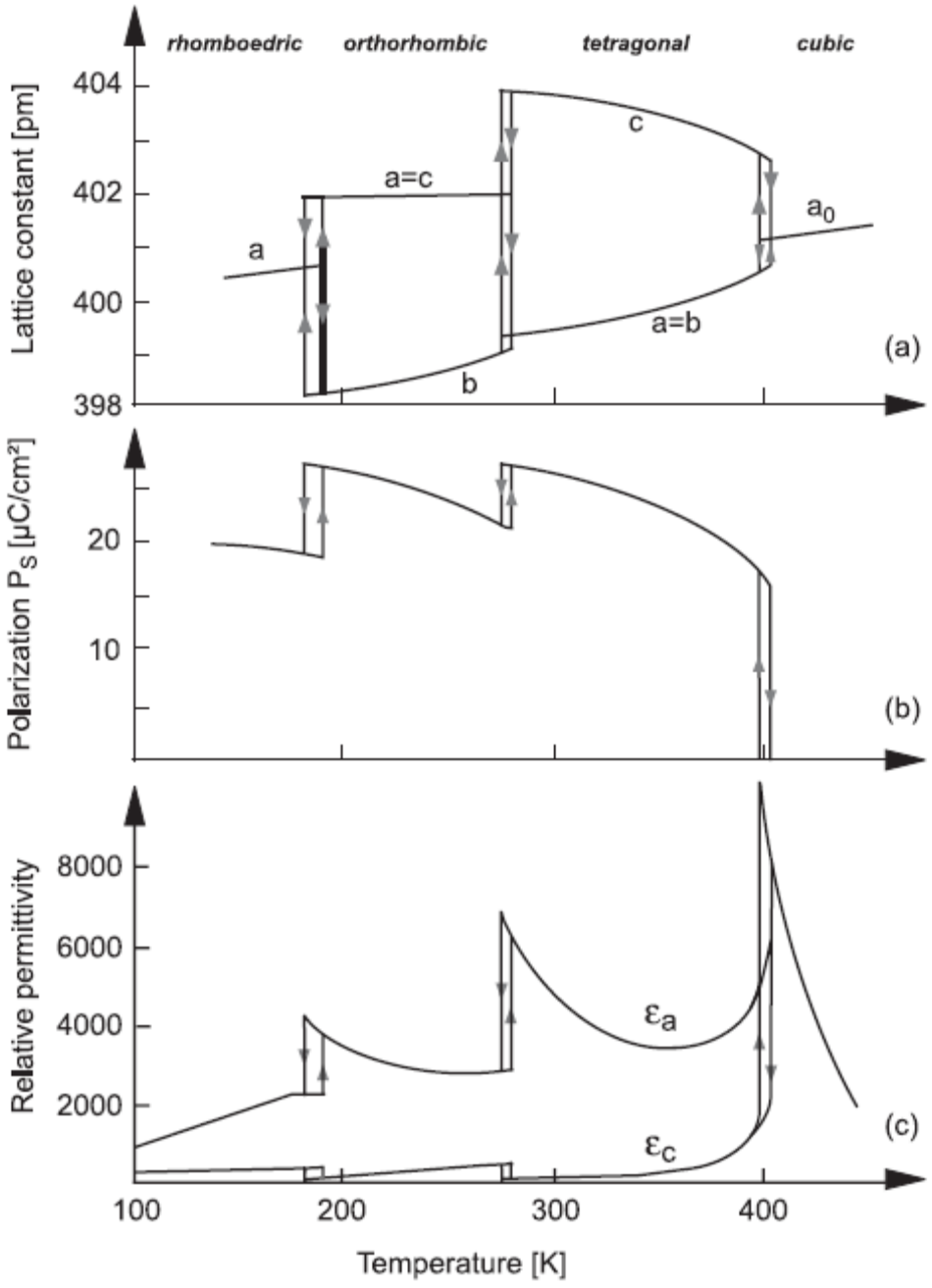

Fig. 2.8 Phase transitions versus temperature in a $BaTiO_3$ crystal. Anisotropic properties are shown with respect to the lattice direction. (a) Lattice constants, (b) spontaneous polarization P_s and (c) relative permittivity where the ε_a and ε_c represent single crystals with a and c-axis orientation [18].

2.7 Combinatorial/High-throughput experimentation

Combinatorial experimentation refers to those experiments where elements or groups of different materials such as solvents, additives or other components are combined. The nature of the parameters are varied instead of the value of the parameters [27]. It has been defined as “the synthesis of a library of compounds to create new compounds by combining a set of basic building blocks in many different ways” [28]. The variation of parameters like composition, temperature, pressure in a systematic manner to explore a wide space is termed high-throughput experimentation (HTE) [27]. Miniaturization, robotics and parallel techniques are used to increase productivity [10]. High-throughput screening has been defined as “a set of techniques for creating a multiplicity of compounds and testing them for activity. It is widely applied in pharmaceutical research but is now also used for materials research” [29]. The pioneers in this research field include Thomas Edison (1878), Mitasch (1909) as well as Ciamician (1912).

High-throughput experimentation has been applied to a wide variety of materials which include; luminescent materials, optically functional oxides, dielectric and ferroelectric materials, battery materials, magnetic materials ($La_{1-x}Ca_xMnO_3$), fuel cell materials, coating materials, membranes, polymers, gas sensors and heterogeneous catalysis [27]. It has had tremendous success in materials research with high quantum-efficiency phosphor, new zeolites, catalysts, sensor materials, dielectric materials etc. being discovered. It is now being routinely applied for the synthesis and characterization of materials at a much faster rate than would have been imagined a couple of years ago [27].

2.7.1 Design of experiment

With high-throughput methods, the ability to generate a large number of experiments arises so it is necessary that a systematic approach to design these experiments is carefully developed. In materials research, large processing parameters, broad range of compositions and structural variables make the dimensionality of the experiment daunting [30]. It is therefore necessary that prior knowledge of the system (solubility limits, phase transitions etc.) to be investigated using HTE be known so that the experimental space to be investigated is reduced while the efficiency is increased.

Design of experiment is a technique that minimizes experimental effort while maximizing information output. This can be grouped into three major parts; mapping, screening and optimization. Mapping is the first step in the process with the goal of developing knowledge of the relationship that exists between materials and experimental parameters. Screening aims to efficiently identify the leads through search of the paramter space for getting the desired property [10].

2.7.2 High-throughput synthesis of ceramic materials

It is estimated that in advanced ceramics, less than 1% of possible ternary compounds and even less than 0.01% of quaternary compounds have been investigated [28]. High-throughput synthesis are carried out mainly on thin films but the problem is that sometimes the result from thin film samples differs from that of bulk ceramics. In the characterization of piezoelectric ceramics, properties like the piezoelectric coefficient (d_{33}), doping effects, grain size effects can be better determined using samples in their bulk form. Physical vapor deposition, pulsed laser deposition, molecular beam epitaxy, chemical vapor deposition and solution deposition techniques are some of the techniques used. Some of the approaches employed in materials development include;

1. Gradient arrays are closely related to the continuous composition spread (CCS) developed mainly for studying electronic thin-film materials and used for identifying phase regions with suitable properties. An example is the Ni-Cr-Fe pseudo-ternary phase diagram is shown in Fig. 2.3

CCS was initially introduced by Hanak [33] where he explained both 1-dimensional (1-D) and 2-dimensional (2-D) CCS. For complex materials like piezoelectric ceramics, it is difficult to apply 2-D CCS approach. 1-D CCS method is suitable for studies where the goal is to investigate the properties as a function of composition in a known system. The advantage is that very fine compositional resolution can be achieved.

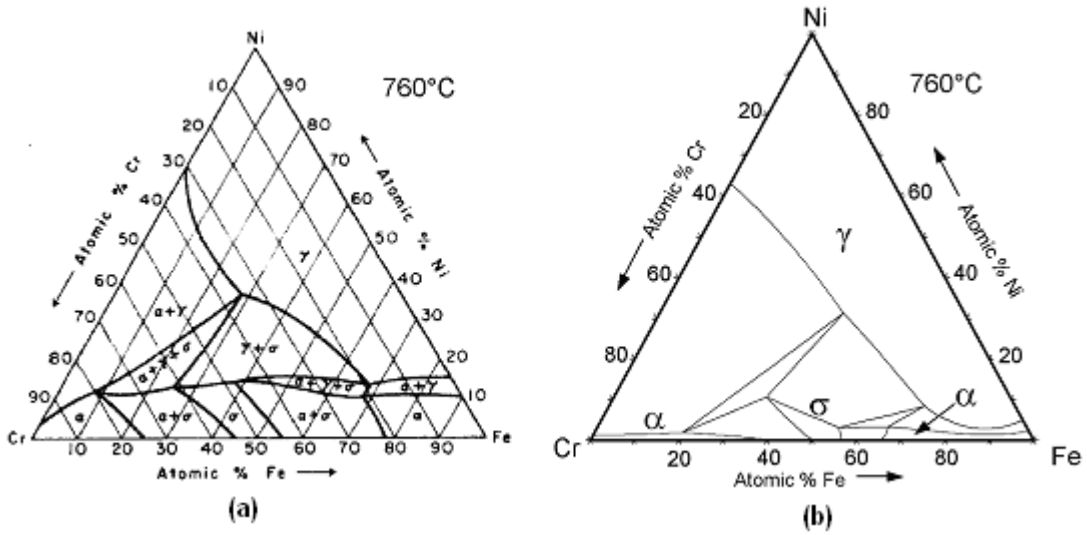

Fig. 2.3 Combinatorial/high-throughput determination of the Cr–Fe–Ni ternary phase diagram at 760 °C by Kennedy et al. in 1965 [31] (b) the Cr–Fe–Ni isothermal section at 760 °C determined from gradient thin films using X-ray fluorescence for composition determination and X-ray diffraction for crystal structure identification [32].

2. Quartenary mask arrays are mainly suited for metal oxides which have the perovskite structure. $A_mB_nO_x$ is a dopant for two atoms although dopants for three atoms or more can be applied.

3. High speed version of conventional experimental designs is known as nexting [29]. This method is the closest to the high-throughput setup in our institute and uses dosing robots, handlers and plate readers. It is a well-based technology where the wells need to be moved physically and mixed by hand. It has the capability to synthesize using solution techniques (hydrothermal, ink-jet printing) and dry powder synthesis.

2.7.3 High-throughput characterization of ceramic materials

The availability of characterization tools determine the level of success that can be achieved with high-throughput experimentation. If the characterization tool is not adequate, the synthesis will not amount to anything. The tools used should have very high precision and accuracy and every tool in the process has to be automated to prevent a bottleneck in the whole process [34]. Some of the tools that have been used to

characterize/screen libraries produced by this method include mass spectrometer, gas chromatography, X-ray diffraction, capacitance measurement etc.

3 $(K_xNa_{1-x})NbO_3$ ceramics and research objectives

3.1 $(K_xNa_{1-x})NbO_3$ solid solution

3.1.1 $(K_xNa_{1-x})NbO_3$ phase diagram

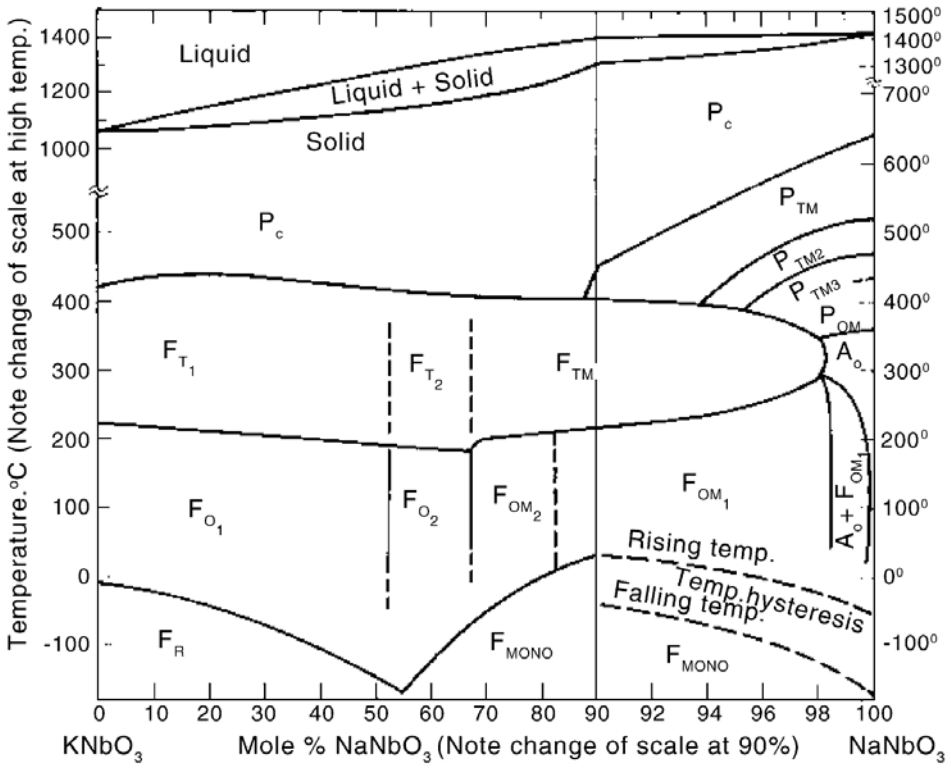

Fig. 3.1 Phase diagram for $KNbO_3$-$NaNbO_3$ solid solution [17].

$(K_xNa_{1-x})NbO_3$, abbreviated KNN is a solid solution of $NaNbO_3$ and $KNbO_3$. $KNbO_3$ is ferroelectric while $NaNbO_3$ is antiferroelectric but ferroelectricity can be induced either by the application of an electric field or doping. Like $BaTiO_3$, both compositions undergo a

series of phase transformations with temperature: On cooling, $KNbO_3$ transforms from the paraelectric cubic phase (P_C) to the ferroelectric tetragonal phase (F_T) at ~435 °C; from F_T to the ferroelectric orthorhombic phase (F_O) at ~225 °C; from the F_O to the ferroelectric rhombohedral phase (F_R) at ~-10 °C. The phase transition in $NaNbO_3$ is more complex and not clearly defined. In most cases, there is the coexistence of more than one phase at the same time. The subscripts "1" and "2" used for the same phase in the phase diagram represent differences in the oxygen octahedral tiltings. The composition with approximately equal amounts of $KNbO_3$ and $NaNbO_3$ represented as $(K_{0.5}Na_{0.5})NbO_3$ which is close to the phase boundary is of most interest to researchers. This is because the properties at this composition are slightly better than in other compositions. Some of the reported properties include d_{33} ~80 pC/N, T_c is ~420 °C, k_p ~0.36 for air sintered samples and d_{33} ~160 pC/N, T_c is ~420 °C, k_p ~0.45 for hot-pressed samples [63]. The theoretical density at this composition is ~4.51 g/cm^3.

3.1.2 Processing of $(K_xNa_{1-x})NbO_3$ ceramics

KNN ceramics are difficult to synthesize because of the very sensitive nature of the starting reagents to the environment. It is very easy to loose the correct stoichiometry and produce something different. There are several methods used to synthesize this ceramic but the most common is through the mixed-oxide synthesis route. In this method, carbonates of Na and K and Nb_2O_5 are mixed, milled, calcined, pressed and then sintered [35]. Some steps have been taken by researchers to make this method to be more efficient. A modified solid state reaction route which reduces the calcination temperature to 550 °C by introducing urea [$CO(NH_2)_2$] has been reported [36, 37]. Addition of excess alkali carbonates [38], leaching of the powders [8], mechanochemical synthesis [39] have been made to optimize the synthesis process. Rochelle salt ($KNaC_4H_4O_6$ $4H_2O$) has also been used as starting reagents and has the advantage of obtaining K and Na in their stoichiometric ratio [40]. Chemical processing routes like microemulsion mediated synthesis have been used to produce powders with average particle sizes that range from 75 nm to 10 µm [41, 42] while alkaline nitrates with a soluble salt $NH_4H_2[NbO(C_2O_4)_3]$ $3H_2O$ as precursors has also been reported [43, 44].

Sintering in furnaces operating under air atmospheres is the most common method to consolidate the samples. The high vapor pressure of the alkali elements necessitates that precautions be taken to reduce the volatility during sintering. The samples are normally placed in a powder bed with the same composition and covered with either a crucible or a

platinum foil. Sintering in different atmospheres (O_2, N_2, air, 75%N_2-25%H_2 and H_2), [45, 46] hot pressing [47, 48], spark plasma sintering (SPS) [49, 50]and microwave sintering [51] have all been used to sinter KNN ceramics.

3.1.3 Modification of $(K_xNa_{1-x})NbO_3$ Ceramics

The sinterability and piezoelectric properties of pure KNN ceramics are not good enough to satisfy industry requirements. Other elements or compounds are therefore incorporated as dopants to improve these properties. There are several reports in the literature with respect to doping of KNN ceramics with other compounds but this review will be restricted to the addition of elements with the same valency on either the A- or B- sites of the perovksite structure and for specific dopants used in this work.

Certain considerations are taken when doping KNN ceramics and the rule of thumb is that the ionic radius and valency of the element to be incorporated determines in theory the position in the lattice. What happens in practice may actually be different because most transition elements have more than one valency and therefore different ionic radii. Also more than one of these dopants is normally added to KNN ceramics thereby complicating how they will react with one another. In order to determine exactly where the elements are incorporated, special analytical techniques like electron paramagnetic resonance (EPR) will have to be used. The theoretical prediction will nonetheless be used to explain the incorporation of these dopants in the structure of KNN ceramics. Elements with valency of +1 are expected to be incorporated into the A-site of the perovskite structure while those with a valency of +5 are incorporated into the B-site. Such elements which have exactly the same valency as the elements they are to replace are called isovalent elements. There are other elements which do not have the same valency as the elements they are to replace. Such elements are called aliovalent elements and in these situations, they either act as donors by giving out electrons or as acceptors by accepting electrons.

Substitution of ceramics with isovalent elements (Li, Ta, Sb etc.) either separately or in combination has been reported to improve their piezoelectric properties [4]. When Li is used to dope KNN (KNN-L), a two-phase boundary between the orthorhombic and the tetragonal phase is observed between 5 and 7 mol% while a second phase ($K_3Li_2Nb_5O_{15}$) is present with more than 7 mol% [52]. Li is expected to be incorporated to the A-site of KNN. Fatigue studies by thermally cycling (20 °C to 140 °C) KNN-L to test it suitablility for use in medical applications showed that the d_{31} and k_p decreased by more than 30 % of

their initial value after the first cycle and is later stabilized [53]. The temperature dependent phase transition of KNN-L ceramics from 0 to 10 mol% studied using Raman spectroscopy, X-ray diffraction and dielectric permittivity showed series of phase changes while a secondary phase was observed with more than 7 mol% Li [54]. A high d_{33} value (405 pC/N) but low dielectric constant value has been reported for (001) oriented single crystal of KNN-L produced using the Bridgman method [55]. To test the suitabliliy of KNN-L ceramics for application purposes, cymbal-shaped actuators have been produced using KNN with 8 mol% Li. Ti alloys were used as endcaps and the properties obtained were comparable to those from PZT ceramics [56].

When Sb is added to KNN ceramics, it is expected to be incorporated to the B-site of the structure. It is difficult to say exactly where manganese will be incorporated in KNN because it has different valencies which can exist either alone or in combination with one another. Some researchers claim that MnO_2 acts only as a sintering aid to KNN but that ascertion has not been experimentally verified [57]. KNN ceramics doped with Sb (KNN-S) together with MnO_2 has been reported to improve the ferroelectric properties of KNN and a phase boundary between an orthorhombic and a tetragonal phase was observed. At the tetragonal side of the phase boundary, the piezoelectric properties and its temperature stability were better than at the orthorhombic side [57].

Tantalum in KNN is expected to be incorporated into the B-site of the lattice. KNN doped with Ta (KNN-T) increases the optimum sintering temperature and a relaxor-like behavior is observed. Ta addition softened the ceramics leading to improvement in d_{33}, k_p, k_t, ε_r and reduction in E_c, quality mechanical factor (Q_m) and frequency constant (N_p) [58]. An electro-holographic crystal from a top seeded solution growth method for optical application has been produced with KNN-T composition for application purposes [59]. KNN-T ceramics doped with CuO which has high Q_m values has also been reported [60].
A comprehensive study of KNN doped with both Li and Ta (KNN-LT) was reported by Saito et al. [61]. Phase boundaries between orthorhombic and tetragonal phases were observed with changing amounts of Li and Ta and the reported highest piezoelectric activity (d_{33} ~230 pm/V) was obtained with $((K_{0.5}Na_{0.5})_{0.97}Li_{0.03})(Nb_{0.8}Ta_{0.2})O_3$ composition. A tetragonal tungsten bronze structure was observed when 6 mol% excess alkali carbonates were added to the system [62]. Abnormal core-shell structure just like in $BaTiO_3$ has also been reported and interpreted using the classical grain growth theory [63].

Excess Na_2O [64] and Li_2O [65] in KNN-LT have led to abnormal grain growth which was explained by interface reaction-controlled nucleation and growth. BaO [66], MnO [67] and CuO have all been added to KNN-LT ceramics to improve either the sinterability or the piezoelectric properties. The effect of K/Na ratio on KNN-LT has been studied using Raman spectroscopy and other characterization techniques [68].

KNN ceramics with Li and Sb (KNN-LS) has been studied and the phase boundary between an orthorhombic and a tetragonal phase was observed between 4 and 6 mol% of the dopant [69]. The effect of varying the amounts of potassium present on the properties of KNN-LS ceramics has been investigated [70]. A precursor coating approach which gives larger grain size and better sinterability was used to study the effect of adding Sb on KNN-LS ceramics [71]. $CaTiO_3$ has been added to KNN-LS ceramics [72] and its aging behavior show that after a hysteresis cycling of 10,000 times, the P_r and S_r values remained almost unchanged [73] Thick films of KNN-LS ceramics have been produced using precursors made by a coating method [74] and aerosol deposition [75]. DC magnetization and dielectric properties dependence has been investigated in Cobalt ferrite ($CoFe_2O_4$) doped KNN-LS ceramics produced using the citrate gel method [76]. As the amount of added $CoFe_2O_4$ increased, the dielectric constant decreased while the magnetic moment increased.

KNN doped with Li, Ta and Sb (KNN-LST) was reported by Saito et al. to have piezoelectric properties comparable to those from PZT ceramics [4]. The d_{33} value for the non-textured ceramics is >300 pC/N while for the textured samples, a d_{33} value >416 pC/N was obtained. Similar compositions have since been investigated by other researchers. The origin of the high piezoelectric activity in this material was studied from -95 °C to 200 °C and the instability at 25 °C was reported to be the reason [77]. The processing relationship in addition to the effect of humidity on the properties using both the mixed-oxide and the perovskite synthesis routes showed that there was no significant difference with both methods [78]. Sintering in oxygen atmosphere at a flow rate of 130–180 cm^3 resulted in the best properties. The effect of varying the amounts of Li [79], Ta [80] and $LiTaO_3$ [81] have all been investigated. Special characterization techniques like Raman spectroscopy has been used to investigate the relationship between the structure of this ceramic and its piezoelectric properties [82]. Piezoresponse force microscopy (PFM) has been used to

show that the domains present are primarily 180° which confirmed the hypothesis of tetragonal crystal structure with predominantly *c*-axis oriented domains [83].

3.1.4 Summary

In the last few years, a lot of work has been done in trying to understand the nature of KNN-based ceramics and subsequently improve both their piezoelectric and electromechanical properties. Doping elements like Li, Ta, Sb, Bi-based compounds, and sintering aids like Cu and Mn were mainly used to improve the piezoelectric properties and the sinterability of the ceramics respectively. There is however no fundamental understanding of the underlying electrochemical and physical mechanisms of KNN based ceramics which allows predicting the effect of dopants on the electromechanical properties and microstructure. Empirical knowledge like the ionic radius of the elements and their valency form the basis in the prediction of the location of the dopants in the perovskite structure. The microstructure of the ceramics via grain orientation has been made more anisotropic by the use of seeds and grain sizes have been engineered to be smaller so that the leakage current is reduced thereby increasing the electric field that can be applied during poling.

Temperature-dependent piezoelectric charge coefficient and other electromechanical coefficients have shown that stable properties (slight decrease with increasing temperature) can be obtained from ambient temperatures to higher temperatures. Fatigue studies on KNN-LS ceramics with $CaTiO_3$ also showed that after an initial drop in properties, stable properties can be obtained over a long period of time just like in PZT-based ceramics [73]. Efforts are steadily being made to produce KNN-based ceramics in single crystal, thin film and thick film forms so that they can be applied industrially. Theoretical studies using ab-initio modelling are gradually being introduced in the investigation of the properties of KNN ceramics [84]. At the moment however, only very simple compositions like $BaTiO_3$ [85] can be investigated as more computing power and complex codes will be required to investigate the more complex compositions that are currently being investigated experimentally.

3.2 Research objectives and strategy

Research on lead-free ferroelectric ceramics in the last few years has focused on modifying these ceramics in different ways to achieve certain objectives. An example is the use of MnO_2 to reduce the dielectric loss in piezoelectric ceramics. The current research is in many ways guided by the experience gained from years of research on both $BaTiO_3$ and PZT single crystals and ceramics.

Pure KNN ceramics has low piezoelectric properties which make them inappropriate for industrial application and so element incorporation is done to improve its sinterability and piezoelectric properties. High-throughput experimentation has been successfully applied in materials research to discover several new catalysts, alloys, phosphors, polymers etc. It has also been used in thin film ceramics research but it is not popular with bulk ceramics research due to reproducibility concerns which is very important for ceramics. Research on KNN ceramics has mainly focused on their electrical properties and where there are structural studies, they are either on pure KNN ceramics or single crystals.

The **objectives** of this research work are therefore to:

1. To search for KNN-based ceramics with high piezoelectric properties.
2. To investigate if the effect of some dopants on PZT ceramics is similar to KNN ceramics.
3. To show that with high-throughput experimentation method, bulk polycrystalline ceramics can be produced and that the properties of these ceramics can be compared with those from conventional ceramic synthesis.
4. To investigate the temperature dependence of the crystal structures of KNN ceramics modified with isovalent elements.

The **strategy** employed to achieve these objectives include:

1. To modify the properties of KNN ceramics through element incorporation on both the A- and B sites of the structure.
2. To apply the knowledge gained over the years in researching PZT and $BaTiO_3$ ceramics on KNN ceramics.

3. To combine conventional ceramic synthesis method with high-throughput experimentation method.
4. To use high resolution X-ray diffraction to investigate the structure of KNN ceramics.

4 Materials and Methods

4.1 Sample preparation

The raw materials used for this research are mainly commercial powders whose level of purity and source are shown in Table 4.1.

Table 4.1 Raw powders used in the synthesis of KNN-based piezoelectric ceramics

Chemical name	Chemical formula	Purity	Source
Potassium carbonate	K_2CO_3	>99+%	ChemPur Feinchemikalien, Alfa Aesar
Sodium carbonate	Na_2CO_3	>99+%	ChemPur Feinchemikalien, Alfa Aesar
Lithium carbonate	Li_2CO_3	>99+%	ChemPur Feinchemikalien, Alfa Aesar
Antimony (III) oxide	Sb_2O_3	>99.9%	ChemPur Feinchemikalien, Alfa Aesar
Niobium (V) oxide	Nb_2O_5	>99.9%	ChemPur Feinchemikalien, Alfa Aesar
Tantalum (V) oxide	Ta_2O_5	>99.9%	ChemPur Feinchemikalien, Alfa Aesar
Manganese (II)oxide	MnO_2	>99+%	Merck chemicals
Bismuth (III) oxide	Bi_2O_3	>99+%	MCP-GmbH

Both conventional and high-throughput experimentation methods were used for this work and the compositions investigated include;

a. Conventional methods:

(i) $(K_{0.44}Na_{0.52}Li_{0.04})(Nb_{0.86}Ta_{0.1}Sb_{0.04})O_3$ doped with different amounts of Mn

(ii) $(K_{0.5}Na_{0.5})NbO_3$ doped with different amounts of Sb

b. High-throughput experimentation methods:

(i) $(K_{0.5}Na_{0.5})NbO_3$ abbreviated as KNN,

(ii) $(K_{0.48}Na_{0.48}Li_{0.04})(Nb_{0.9}Ta_{0.1})O_3$ abbreviated as KNN-LT,

(iii) $(K_{0.48}Na_{0.48}Li_{0.04})(Nb_{0.86}Ta_{0.1}Sb_{0.04})O_3$ abbreviated as KNN-LST

Bi_2O_3 was used to dope the samples in the following amounts; x (mol%) = [0; 0.05; 1.0].

c. Synchrotron X-ray diffraction studies of KNN-based ceramics

Temperature-dependent synchrotron X-ray diffraction measurements were made on the following compositions from low temperatures to temperatures above their respective T_c values:

(i) $(K_{0.47}Na_{0.51}Li_{0.03})NbO_{3.01}$

(ii) $(K_{0.49}Na_{0.51})(Nb_{0.88}Ta_{0.1})O_3$

(iii) $(K_{0.48}Na_{0.55})(Nb_{0.92}Sb_{0.05})O_3$

(iv) $(K_{0.47}Na_{0.51}Li_{0.025})(Nb_{0.88}Ta_{0.1})O_{3.02}$

(v) $(K_{0.37}Na_{0.52}Li_{0.03})(Nb_{0.87}Ta_{0.1}Sb_{0.03})O_3$

The abbreviation “HTE” will be appended in bracket to any processing step that was exclusively used for high-throughput experimentation.

The general procedure for measuring the amount of each component raw powder in order to obtain a certain ceramic composition is as follows:

(i) The compositions to be synthesized will have to be defined

(ii) The appropriate raw powders needed to obtain these compsoitions are selected

(iii) A balanced equation of chemical reactions involving the reactants (raw powders) and the desired products is written

(iv) The molar mass of each raw powder is calculated and the sum of all molar masses obtained

(v) The fraction of each powder in relation to the whole multiplied by the amount of powder needed is used to obtain the amount of each component raw powder.

4.1.1 Raw powder conditioning

Raw powders like the carbonates are hygroscopic and absorb moisture when left in ordinary conditions. The moisture needs to be removed before the synthesis process begins. The powders were initially dried in an oven at 200 °C for a minimum of 4 h before either dosing using the robot or manual measurement in the case of conventional synthesis. The objective here is to ensure that all absorbed moisture has been removed.

4.1.2 Dosing of raw powders (HTE)

Dosing of raw powders was done only for HTE purposes and was carried out using a laboratory robot (Accelerator VLT-100, Chemspeed Technologies, Augst, Switzerland). Approximately 1,100 mg comprising of different raw powders was dosed for each composition. It is important to emphasize that the powders need to be flowable inorder for this process to go smoothly. Sticky powders were first milled, dried and sieved before dosing was carried out. The solid dispensing unit consists of two parts; a precision balance which can measure a maximum of 10 g with a resolution of 0.1 mg and a carbon polyether ether ketone (PEEK) holder which is driven by a 3.5W D.C motor. A 15 ml polyethylene (PE) bottle fitted with a dispensing funnel made from carbon-loaded high density polyethylene (HDPE) and screw extruder were used.

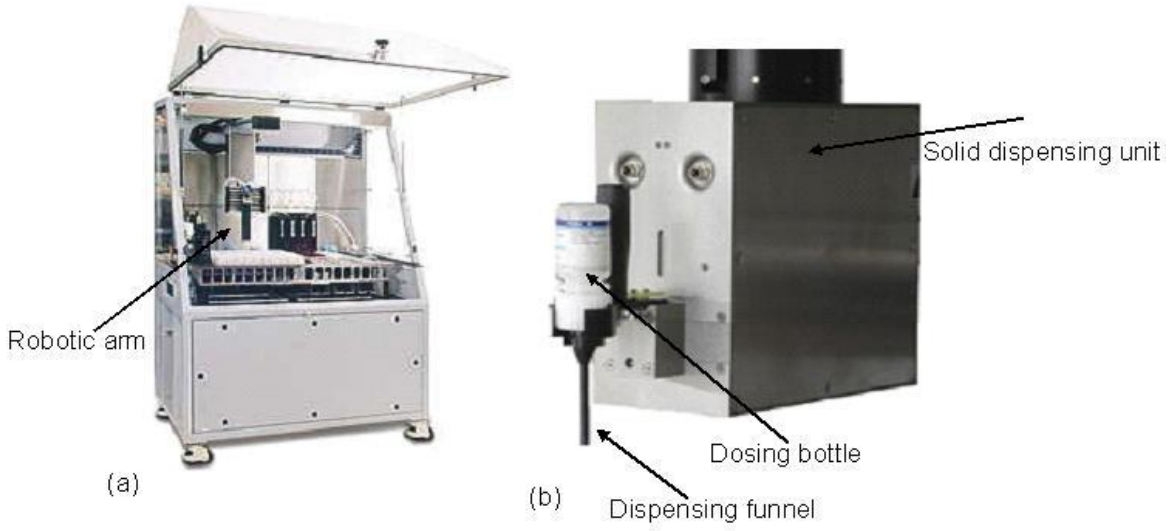

Fig. 4.1 Picture of the (a) VLT-100 dual dispensing station and (b) solid dispensing unit (SDU).

Three different types of extruders were used depending on the flowability of the powders (Fig. 4.2). Type I (narrow thread) extruder is used for powders which are highly flowable while Type II (narrow thread modified with wire for easier dosing) extruder is used for powders which are less flowable while Type III extruder (wide thread) is used for powders with moderate flowability.

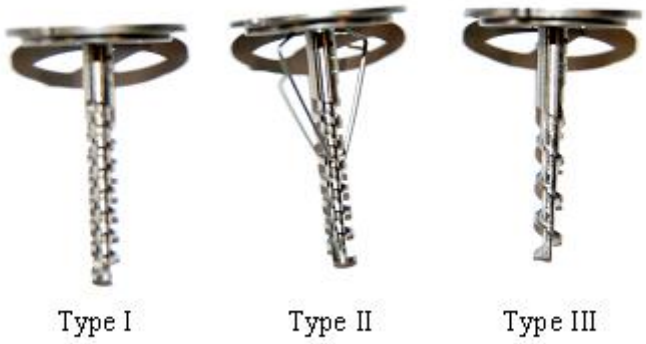

Fig. 4.2 Different types of extruders to suit the property of the powder. Type I (narrow thread), Type II (narrow thread modified with wire for easier dosing), and Type III (wide thread).

The *SWING* program (software from Chemspeed Technologies) has a graphical user interface and there are three major dispensing parameters: the fine dispensing amount (FD amount), the fine dispensing speed (FD speed) and the filter coefficient. An auto-teaching tool that is stored in the database and retrieved whenever needed enabled these parameters to be determined automatically. Fast or slow dosing speeds are allowed during dosing. These parameters are adjusted depending on the nature of the powder being dosed. More details about the operating principles of the robot can be found in the article by Stegk et al. [86].

4.1.3 Speed Mixing (HTE)

The dosed powders are speed-mixed in the dry state to obtain an almost homogeneous powder. This process was carried out at 1600 rpm for 1 min using a speed mixer (Speedmixer DAC 150 FVZ, Hauschild, Germany).

4.1.4 Milling

Attrition milling

This process was used only for conventional solid state synthesis. The importance of this process is underscored by the fact that if the powders are not properly mixed and reduced to the appropriate particle size, all the other steps and ultimately the properties will be affected. The powders were introduced in their stoichiometric amounts to an alumina milling container. Ethanol was used as solvent while yttria stabilized zirconia balls

(3 mmϕ) were used as the grinding media. The milling was done at rotation speeds between 300 and 500 rpm for 2-4 h. The particle size distribution of the powders was measured every hour using the particle size analyzer. After the milling process, the powders were dried using a solvent extractor and it was repeated after calcination of the dried powder.

Planetary milling (HTE)

This process was used for high-throughput synthesis. It was carried out with a conventional planetary mill (Pulverisette, Fritsch, Idar-Oberstein, Germany) which was modified for HTE purposes. The objective here was to obtain a homogeneously mixed suspension with small particle size distribution. Ethanol was used as the solvent while yttria stabilized zirconia balls (3 mmϕ) were used as the grinding media. Milling was carried out at 200 rpm for 3 h. This modified process allowed for simultaneous milling of 16 different powder compositions as shown in Fig 4.3. During the milling process, samples were taken after every hour to determine their particle size distribution using a particle size analyzer. This process was repeated after calcination of the powders.

Fig. 4.3 High-throughput compatible planetary mill. The bigger milling containers were modified to accommodate 16 smaller milling containers to facilitate simultaneousl milling. The smaller milling containers were made from ultra-high-molecular-weight polyethylene (UHMPE).

4.1.5 Particle size analysis

Particle size analysis was carried out using a particle size analyzer (M 2000, Malvern Instruments, UK) which uses laser diffraction to determine the particle sizes. The relation

between particle size and scattering angle is such that large particles scatter light at low angles while small particles scatter light at high angles. The particles were dispersed with an ultrasonic stirrer prior to the measurement. It was ensured during every measurement that the laser power was not below 65 %. The results are normally displayed to show d_{10}, d_{50} and d_{90} which represent the amount of particles within 10, 50 and 90 % of the particle size distribution respectively. The d_{50} which is close to the average of the particle sizes is plotted in Fig. 4.4 to show a typical result from a particle size analysis of our samples. As the milling is carried out, the particle size decreases and after the calcinations, it increases again. The second milling is to ensure that the d_{50} values of the particles is less than 1 µm.

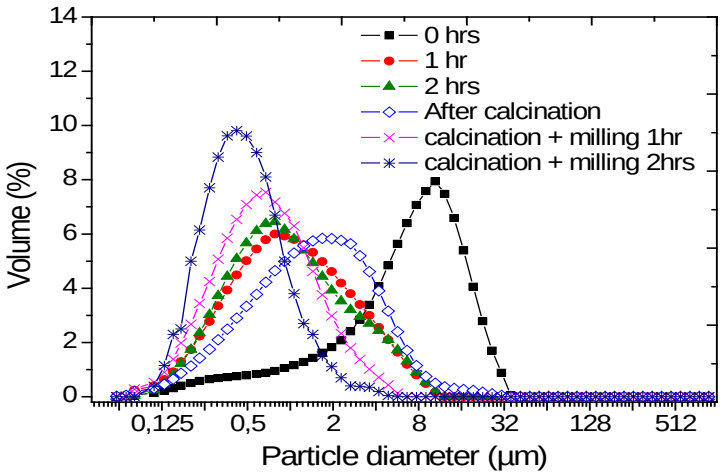

Fig. 4.4 (a) Typical distribution of the mean particle sizes (d_{50}) of the powder suspension during attrition milling which was carried out at 1 h intervals before and after calcination of the powders.

4.1.6 Calcination

Calcination is the first step in the phase formation process and was carried out at temperatures between 750 °C and 950 °C for 4 h at a heating rate of 3 °C/min and a cooling rate of 10 °C/min. A chamber furnace (HT 04/17, Nabertherm, Germany) and a tube furnace were used for the process in air atmosphere. Calcination causes the constituents to interact by interdiffusion of their ions thereby reducing the diffusion time during sintering. A typical example of a reaction that should take place during calcination is shown in equation 4.1.

$$0.25\ X_2CO_3 + 0.25\ Y_2CO_3 + Z_2O_5 \rightarrow (X_{0.5}Y_{0.5})ZO_3 + CO_2\uparrow \qquad (4.1)$$

where X and Y could be be Na, K while Z could be Nb, Ta etc. All the carbon in the powder is expective to be removed as CO_2.

4.1.7 Pressing

Pressing was done to give shape to the powders and two types of presses were used. The first is the uniaxial press (P/O/Weber, Remshalden-Brunbach, Germany) which was used only for samples produced through conventional method. The powders were pressed with 170 MPa for 30 sec (12.5 mm ϕ). The pressure distribution in this process is normally not completely homogenous. A cold isostatic press (KIPP200ES, Paul Weber, Remschalden-Brunbach, Germany) was used to produce a homogeneously dense powder compact by the application of a hydrostatic pressure. The samples were encased in an air-tight polymeric material and introduced to the pressing chamber. An in-house produced silicone mould which allows for parallel pressing of 5 pellets as shown in Fig 4.5 was used for the HTE samples. Pressures between 300 MPa and 500 MPa were applied on the samples for 2 min.

Fig. 4.5 Silicon mould adapted for use in cold isostatic press for both conventional and high-throughput synthesized powders.

4.1.8 Sintering

The aim of sintering is densification of the samples while the driving force is the reduction of the interfacial surface energy as the free surfaces of particles disappear. This was carried out in a chamber furnace (HT 04/17, Nabertherm, Germany) in air atmosphere at a heating rate between 2 and 3 °C/min and a cooling rate of 10 °C/min. The holding time during sintering was varied between 1 h to 4 h while the sintering temperature also varied from 1060 °C to 1150 °C depending on the composition.

4.1.9 Grinding and Polishing

The surfaces of the sample were removed and smoothened through grinding and polishing. The samples were glued to a sample holder and the grinding process was started with a coarse paper (~120 µm) and the thickness was gradually reduced to 1 µm. The polishing was done with a polishing cloth and a diamond paste (Struers, GmbH Dusseldorf, Germany) from 15 µm down to 1 µm while the polishing suspension was used as a lubricating medium. Samples for microstructural analysis were chemically etched for about 5 min using a suspension called Mastermet (colloidal silica polishing suspension).

4.2 Sample characterization

4.2.1 Density determination

The density values for all the samples were determined using the Archimedes method. Two ways of measuring density using this method were applied; distilled water and a mixture of 86 % glycerin and 14 % H_2O. Distilled water is preferable when there are only closed pores in the sample while glycerin-water mixture is used when the sample to be measured has open pores. The mixture therefore serves to reduce the degree of error from the open pores on the density of the sample. For the measurement with distilled water, the samples were first weighed in air and later when immersed in water. The density was determined under normal atmospheric conditions using equation 4.2.

$$\rho_p = \frac{\rho_w M_l - \rho_l M_w}{M_l - M_w} \tag{4.2}$$

Where ρ_p is the density of the pellet, ρ_w is the density of the water as a function of temperature, M_l is the mass of the pellet in air, ρ_l is the density in air (~20 °C) and M_w is the mass of the pellet in water. This method is appropriate only if the materials to be measured have closed porosity. For measurements with the water-glycerin mix, the formula in equation 4.3 was used.

$$\rho_P = \rho_{GW} \frac{M_l}{M_{lf} - M_{GW}} \tag{4.3}$$

where ρ_P is the density of the pellet, ρ_{GW} is the density of the water-glycerin mix at 20 °C (1.223 g/cm^3), M_l is the mass in air, M_{lf} is the mass after immersing in water-glycerin

mix and drying afterwards and M_{GW} is the mass when immersed in the water-glycerin mix.

4.2.2 OES/ICP spectroscopy

Inductively Coupled Plasma (ICP) spectroscopy technique is sometimes called the “wet” sampling method because the samples are introduced in liquid form for analysis. In optical emission spectroscopy (OES), the sample solution is introduced to the core of the inductively coupled argon plasma which generates a temperature of about 8000 °C. The temperature is enough to thermally excite all elements and they emit light at their characteristic wavelengths. The emitted light is then collected by the spectrometer and then passed through a diffraction grating which resolves the light into a spectrum of its constituent wavelengths. The diffracted light is collected by wavelength and amplified to give an intensity measurement that is converted into an elemental concentration by comparison with the calibration standards. The samples were measured with HNO_3-3HCl-HF mixture which was subjected to microwave digestion. The samples were prepared with 2 sub-samples and the results were averaged. The oxygen concentration was calculated from the molecular weight of the sample.

Optical emission spectroscopy/Inductive coupled plasma (OES/ICP (PE-Optima 7000 DV)) equipment was used to determine the actual amount of each element present and possible elements introduced as impurities during sample processing. The result of the chemical analysis is presented in g/kg concentration basis and is converted into mol.

The procedure for converting to mol is as follows:

a) The concentration (g/kg) of each element present is divided with their respective molar masses
b) The resulting quotient for each element is summed
c) The ABO_3 configuration is taken as 5 (1 each for the A-and B-atoms and 3 for oxygen atom)
d) The quotient for each element is divided with the summed value and multiplied by 5 to obtain the concentration in mole for each element

4.2.3 Powder X-ray diffraction

The atomic lattice of materials irradiated with parallel beam of X-rays acts as a three dimensional diffraction grating resulting in the X-ray beam being diffracted to specific

angles. A lot of information about the material is obtained from both intensities of the diffracted beam and position (angles) of the diffraction pattern. The intensity is used to assess the nature and type of atoms while the position is used to calculate the interplanar spacings (d-spacings). The arrangement of the atoms within the lattice can also be obtained from the position of the diffracted peaks [87]. The basis for the measurements is the Bragg law which uses the simple notion of mirror reflection of the incident X-ray beam from a series of crystallographic planes as shown in Fig. 4.6.

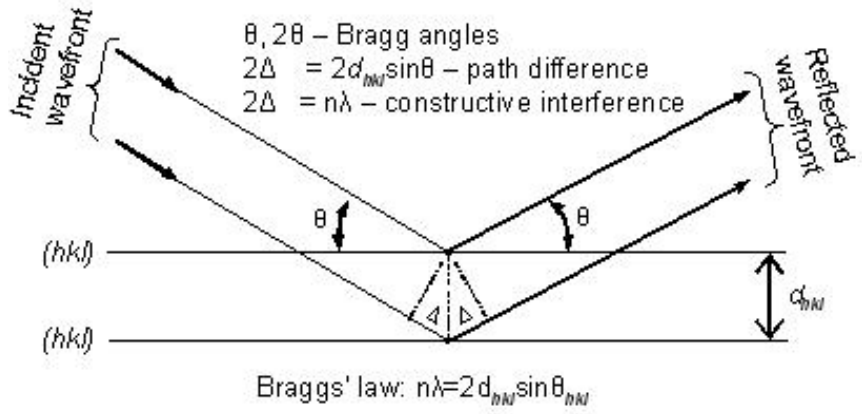

Fig. 4.6 Geometrical illustration of the Braggs' law. Adapted from reference [87].

The powder X-ray diffraction measurements were carried out with a D8 Discover (Bruker AXS, Karlruhe, Germany) equipped with a Göbel mirror to parallelize the incident beam with the general area diffraction detection system (GADDS). With GADDS, it is possible to concurrently detect the 2θ window as against successive scanning with other diffractometers. The measuring time is therefore reduced drastically to a couple of seconds. The X-ray source is from a CuKα (λ=1.54178 Å) and the resolution is 0.020°. Automation of the process was possible because of a movable xyz-table and a script which allowed scanning of many samples at a time. The peak search and match was carried out using the commercial software EVA from Bruker and the reference patterns were from International Centre for Diffraction Data database (ICDD). The crystallographic software TOPAS was also used for some refinements. KNN ceramics crystallizes in the perovskite structure and they can have a lot of phases depending on the composition. A rhombohedral, an orthorhombic, a tetragonal, a cubic and even a two-phase coexistence between the phases are all possible in KNN ceramics.

In order to qualitatively distinguish these different phases which can occur, Fig. 4.7 is presented. All the patterns have a single perovskite phase but the reflections which occur between 44.5°and 47.5° will be used to distinguish them. When the intensity of the double-peak on the left is about 50% higher than that on the right, the phase is classified as orthorhombic. When the peak intensities are similar, there is a two-phase coexistence and when the peak intensity on the right is about 50% higher than that on the left, the phase is tetragonal. When it is not possible to identify if two peaks are present, the phase is either pseudocubic or cubic. It could also mean that the resolution of the XRD is not good enough to resolve the peaks.

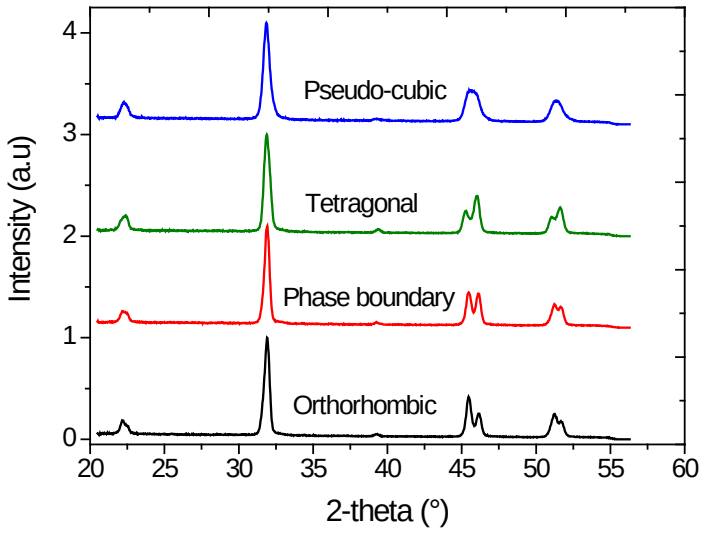

Fig. 4.7 Diffraction patterns showing used to show a qualitative description of the phases observed in $(K_xNa_{1-x})NbO_3$-based ceramics at room temperature.

4.2.4 Synchrotron diffraction data collection

The resolution of the laboratory X-ray is low compared to synchrotron X-ray which has a resolution of 0.004°. Some samples were selected for measurement using the synchrotron X-rays. The synchrotron X-ray diffraction data were collected at the synchrotron facility (beamline B2, HASYLAB/DESY) in Hamburg from -261 °C to 500 °C (well above the T_c) in steps of either 10 °C or 20 °C. Low temperature (-261 °C - 27 °C) measurements were performed in a closed cycle capillary cryostat (Cryophysics) [88] while the high temperature measurements were performed using a capillary furnace from Stoe & Cie type 0.65.3. Data were recorded by a position sensitive image plate detector (OBI, *ortsfest*

auslesbarer Bildplattendetektor) [89] at wavelengths between 0.6880Å - 0.6888Å. More details about the experimental setup at the beamline can be found in the literature [89, 90]. All the collected data were refined by the Rietveld method using the software package Fullprof [91].

4.2.5 Rietveld refinement with Fullprof suite

In Rietveld refinement, the profile is modeled by using the calculated counts Y_i^{calc} as shown in equation 4.9 with each measurement step by adding the contributions from the neighboring reflections plus the background.

$$Y_i^{calc} = \sum_{\phi} S_{\phi} \sum_{h} I_{\phi,h} \Omega\left(T_i - T_{\phi,h}\right) + b_i \tag{4.9}$$

where the vector *h* describes the Bragg reflections, ϕ describes the phases in the model,

$$I_{\phi,h} \text{ is a function of } L_{\phi,h}, A_{\phi,h}, P_{\phi,h}, C_{\phi,h}, F_{\phi,h}^2 \tag{4.10}$$

S_{ϕ} the scale factor of the phase ϕ

$L_{\phi,h}$ contains the Lorentz, polarization and multiplicity factors

$F_{\phi,h}$ the structure factor

$A_{\phi,h}$ absorption correction

$P_{\phi,h}$ the preferred orientation function

Ω the reflection profile function that models both instruments and sample effects

$C_{\phi,h}$ include special corrections (non linearity, efficiencies, special absorption corrections extinction, etc).

T_i a discrete observation at the scattering variable

$T_{\phi,h}$ the scattering variable for Bragg peaks and each phase contributing to the channel

b_i the background intensity

The weighted squared difference between the observed $[Y_i^{obs}]_{i=1,\ldots n}$ and the calculated pattern $[Y_i^{calc}]_{i=1,\ldots n}$.gives a minimum value which is the best least squares fit. The function that is minimized in the Rietveld method is the χ^2 which is calculated using equation 4.11.

$$\chi^2 = \frac{\sum_{i=1}^{n} w_i \left\{Y_i^{obs} - Y_i^{calc}\right\}^2}{n - p} = \left[\frac{R_{wp}}{R_{\exp}}\right]^2 \tag{4.11}$$

where $w_i = \frac{1}{\sigma_i^2}$, σ_i^2 is the variance of the "observation" Y_i^{obs}, n is the number of points in the diffraction pattern with Bragg contribution and p is the number of parameters to be refined which typically varies with the diffraction pattern. The quality of the least square fit is determined by the agreement between observed and calculated profiles also called the agreement factors. Some of the factors include R_p, R_{wp}, R_{exp} and *G.O.F* and they are defined in equations (4.12) - (4.15) respectively.

Profile Factor :
$$R_p = 100 \frac{\sum_{i=1}^{n} \left| Y_i^{obs} - Y_i^{calc} \right|}{\sum_{i=1}^{n} Y_i^{obs}} \tag{4.12}$$

Weighted Profile Factor:
$$R_{wp} = 100 \left[\frac{\sum_{i=1}^{n} w_i \left(Y_i^{obs} - Y_i^{calc} \right)^2}{\sum_{i=1}^{n} w_i \left(Y_i^{obs} \right)^2} \right]^{1/2} \tag{4.13}$$

Expected Weighted Profile Factor:
$$R_{\exp} = 100 \left[\frac{n-p}{\sum_{i=1}^{n} w_i \left(Y_i^{obs} \right)^2} \right]^{1/2} \tag{4.14}$$

Goodness of fit indicator:
$$G.O.F = \frac{R_{wp}}{R_{\exp}} \tag{4.15}$$

All the collected synchrotron data were refined by the Rietveld method using the software FULLPROF [91]. Due to phase coexistence (orthorhombic-tetragonal & rhombohedral-orthorhombic) in some of the collected diffraction patterns over a wide range of temperatures, they were mainly refined using space groups *R3c*, *Amm2*, *P4mm* and $Pm\bar{3}m$ representing the rhomhohedral, orthorhombic, tetragonal and cubic phases respectively. For refinement purposes in *R3c*, it is easier to specify the structural parameters with respect to hexagonal axes.

The background under the peaks was refined using a linear interpolation between points from the regions in which no reflections contributed to the intensity. The model used was based on a Thompson-Cox-Hastings (T-C-H) pseudo-Voigt profile function which is

convoluted with asymmetry due to axial divergence as formulated by Laar et al [92] and using the method of Finger et al. [93, 94]. The atomic positions were refined for the oxygen and B-site cations while the isotropic atomic displacement parameters B_{iso} were refined for all the elements. Efforts to refine the structure using anisotropic displacement parameter were not successful. The anisotropic peak broadening model in the general strain formulation was used to refine the strain in the sample [95]. For more detailed information about this topic, the interested reader is directed to read the FULLPROF manual [91] or other any standard textbook on crystallography.

4.2.6 Grain size determination

Samples selected for microstructural examination with the SEM were thermally etched to reveal their grain boundaries during image acquisition. It was carried out on the samples between 925 °C and 950 °C at a heating and cooling rate of 10 °C/min for about 30 min. The microstructure of the samples was observed using a scanning electron microscope (LEO 1530 FESEM, Gemini/Zeiss, Oberkochen, Germany) with EDX capacities. The average grain size was calculated using mean intercept length method from at-least 6 lines drawn across the image. The average grain size ($\overline{G}$) was calculated using equation 4.4.

$$\overline{G} = 1.5\frac{\sum L}{N} \tag{4.4}$$

where ΣL is the total length of the grains and N is the number of grains that were measured.

4.2.7 Dielectric properties measurement

All the samples for electrical measurement were electroded on both surfaces with a silver paste. For samples produced using the HTE method, the dielectric properties were measured at room temperature using an LCR meter (HP 4284A, Agilent Technologies, Inc., Palo Alto, USA) connected to a measuring robot by measuring the capacitance and dielectric loss at 0.1, 1 and 10 kHz respectively. Resistance measurements were made also for HTE samples with a resistance meter (4339B, Agilent Technologies, Inc., Palo Alto, USA) and the resistivity was calculated using equation 4.5. The measurements were made with a direct current (DC) voltage at 40 V for 10 seconds.

$$\rho = R\frac{A}{l} \tag{4.5}$$

where ρ is the resistivity in Ωcm, R is the resistance, A is the area of the sample and l is the sample thickness.

For selected samples produced using the conventional synthesis method, temperature-dependent dielectric properties measurements were carried out from room temperature to temperatures slightly above their respective T_c values using 5-20 °C measurement steps. The frequency of operation is from 20 Hz to 1 MHz. The LCR meter was connected to a programmable furnace and a schematic diagram of the measurement setup is shown in Fig. 4.7.

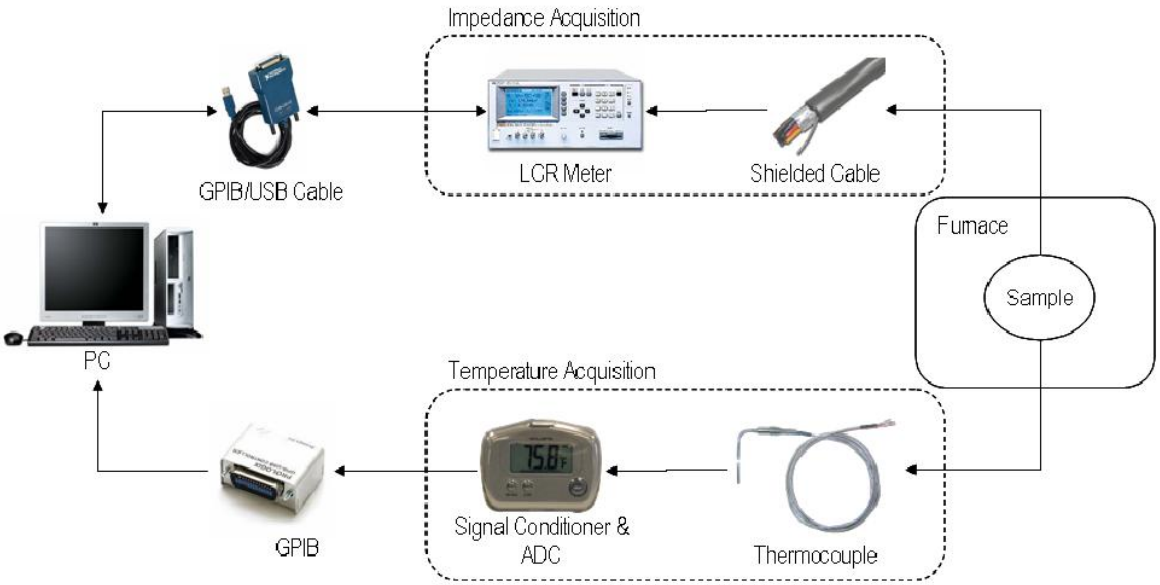

Fig. 4.7 Schematic diagram of the experimental setup for high temperature dielectric properties measurement.

4.2.8 Measurement of polarization hysteresis

The polarization hysteresis measurements were carried out using the standard Sawyer-Tower circuit (Fig. 4.8). The sample to be measured is connected in series with a capacitor C_m with a known capacity. The C_m is much higher than that of the sample to be measured and this causes the measured voltage U_m to be much smaller than the input voltage U_e. In order to avoid dielectric breakdown in air, silicon oil with a high dielectric strength is used to cover the sample. An approximate value of the electric field strength in the sample is obtained with the input voltage and the sample thickness (equation 4.6) since the measurement voltage is much smaller than the applied voltage. The sample surface area is calculated from its geometry, the capacity of the reference capacitor is noted while a

20 kV/cm electric field was used for the measurements. It took approximately 200 seconds to complete a measurement.

$$E = \frac{U_e}{sample \quad thickness} \tag{4.6}$$

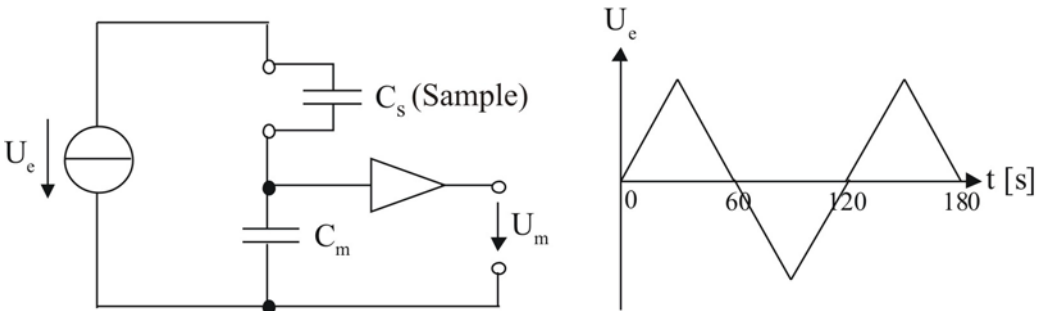

Fig. 4.8 Sawyer-Tower-circuit (simplified), right: Applied voltage - time setup used for the measurements.

The dielectric displacement in the sample is approximately equal to the polarization as shown in equation 4.7

$$D = \frac{Q}{A} = \frac{C_m U_m}{A} = \varepsilon_0 E + P \approx P \tag{4.7}$$

The polarization P is the total of all different polarization mechanisms. The E_c, P_r and P_s were determined from the curve.

4.2.9 Measurement of strain hysteresis

Measurement of strain hysteresis is similar to that of the polarization hysteresis. In this case, the mechanical strain of the sample as a function of the applied electric field is measured. The displacement in the sample is measured with an inductive transducer device (HBM, Hottinger Baldwin Messtechnik, Darmstadt, Germany). The technical strain, S, is calculated from the ratio between the displacement (Δd) and the sample thickness as shown in equation 4.8

$$S = \frac{\Delta d}{sample \quad thickness} \tag{4.8}$$

The remanent strain is determined from the graph as shown in Fig. 2.8. Unipolar and bipolar strain hysteresis curves are obtained by changing the applied voltage versus time

setup in Fig. 4.8. The piezoelectric coefficient d^*_{33} values are calculated from the slope of the unipolar strain hysteresis curves as shown in Fig. 4.9. Some of the precautions that were taken during the measurements include; it was ensured that the contribution from bending or distortion of the sample was as low as possible by making sure that the sample moved freely between the two tips. It was also ensured that the two tips were aligned. The electric field applied to the sample needs to be parallel to the displacement while the sample has to be perpendicular to the induced field.

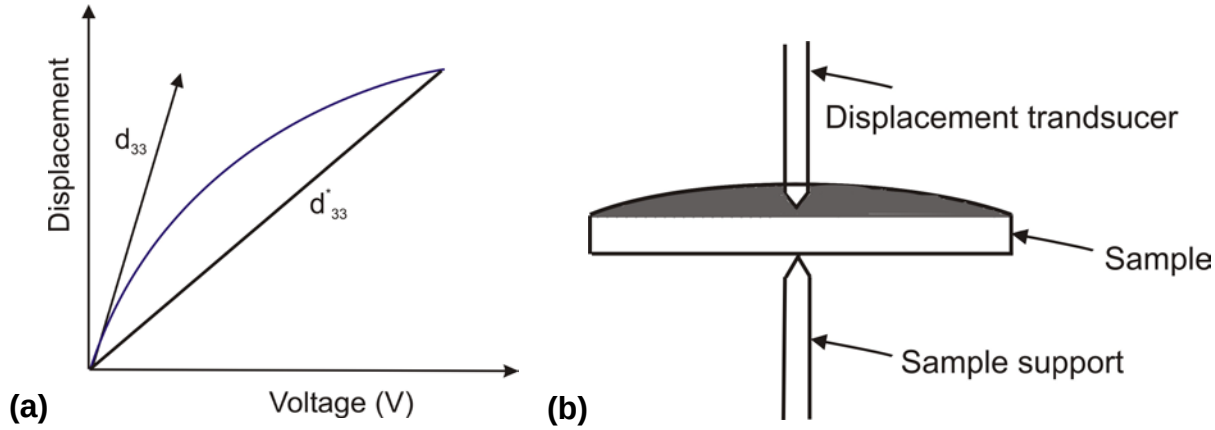

Fig 4.9 (a) Typical displacement versus voltage graph used to calculate the piezoelectric charge coefficient d_{33} implies that the value is from low signal measurement while d^*_{33} implies high signal measurement. (b) Setup for measuring the piezoelectric charge coefficient.

Low signal displacement measurements were used to obtain the piezoelectric coefficient d_{33} for $(K_{0.44}Na_{0.52}Li_{0.04})(Nb_{0.86}Ta_{0.1}Sb_{0.04})O_3$ doped with MnO_2. 65 V was applied to the samples while the amplitude value from the lock-in amplifier was used to calculate the d_{33}.

4.2.10 Impedance measurement

The resonance and antiresonance measurements of the samples were measured with an impedance analyser (HP 4192A). The sample thickness was at-least 10 times less than the diameter to ensure a reliable measurement. The coupling coefficients were obtained by measuring the resonance frequency (f_r) and anti-resonance frequency (f_a) as shown in Fig 4.10a. The geometry of the sample used for the measurements are shown in Fig 4.10b. The planar coupling coefficients, quality factors and frequency constants were calculated using equations (4.9)-(4.11) respectively.

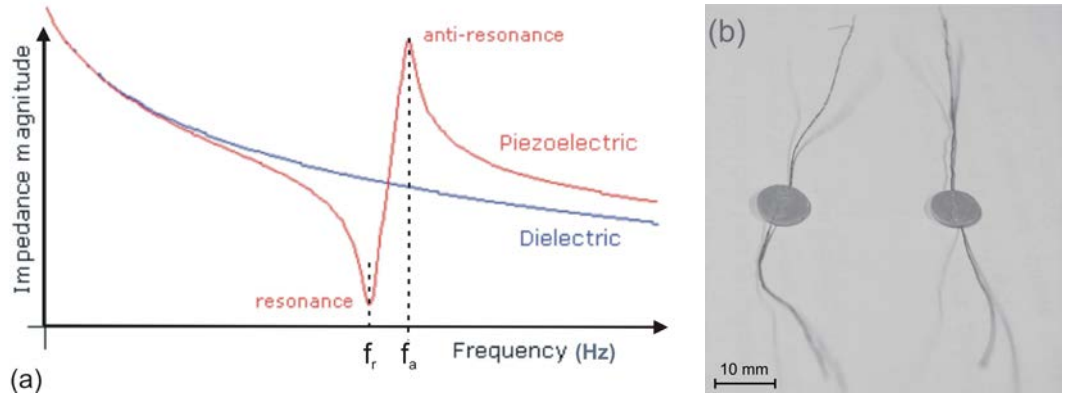

Fig. 4.10 Schematic representation of (a) impedance versus frequency plot for a piezoelectric (red) and a non-piezoelectric (blue) material where f_a and f_r represent the antiresonance and the resonance frequencies respectively (b) geometry of the sample used for the measurements.

$$k_p = \sqrt{\left(\frac{f_a - f_r}{f_a}\right) - \left(\frac{f_a - f_r}{f_a}\right)^2} \tag{4.9}$$

$$Q_m = \frac{1}{2\pi f_r Z_r C_f \left(1 - \left(\frac{f_r}{f_a}\right)\right)^2} \tag{4.10}$$

$$N_p = f_r \cdot Diameter \tag{4.11}$$

where k_p is the planar coupling factor, Q_m is the mechanical quality factor and N_p is the frequency constant (Hertz.meter), Z_r is the value of impedance at resonance frequency and C_f is the capacitance at 1 kHz.

5 Conventional synthesis

5.1 Effect of MnO_2 on the properties of $(K_{0.44}Na_{0.52}Li_{0.04})(Nb_{0.86}Ta_{0.1}Sb_{0.04})O_3$ ferroelectric ceramics

5.1.1 Manganese in piezoelectric ceramics

Manganese is an interesting element because of its multivalent ions (Mn^{2+}, Mn^{3+}, Mn^{4+} etc.) and this multivalence behavior implies that it can enter either the A- or B-site of the perovskite lattice. Soft and hard characteristics of ferroelectric ceramics have been reported for PZT and $BaTiO_3$ doped with Mn [96], [97]. The argument is based on the size of the ionic radius and coordination number (CN) of the elements. Ba and Pb on the A-site have a coordination number of 12 and the resulting ionic radii are 161 pm and 149 pm respectively. Ti can have a valent state of both +3 and +4 and for a coordination number of 6, the ionic radii are 67 pm and 60.5 pm respectively. The ionic radii of Mn^{2+}, Mn^{3+} and Mn^{4+} with a coordination number of 6 are 67 pm, 58 pm and 53 pm respectively.

It is believed that this smaller ionic radius favours it to enter the B-site thereby replacing Ti^{4+} [98]. Oxygen vacancies can only be produced when Mn enters as Mn^{2+} or Mn^{3+} as shown using the defect chemical reaction in equations 5.1 and 5.2 respectively.

$$MnO \xrightarrow{BaTiO_3} Mn_{Ti}^{''} + V_O^{\bullet\bullet} \tag{5.1}$$

$$Mn_2O_3 \xrightarrow{2BaTiO_3} 2Mn_{Ti}^{'} + 2O_O^{\times} + V_O^{\bullet\bullet} \tag{5.2}$$

Conductivity measurements on Mn doped $BaTiO_3$ shows Mn oxidizes from Mn^{3+} to Mn^{4+} which leads to variation in the electrical conductivity as the pO_2 increased [98]. Mn doping in $Pb(Mn_{1/3}Nb_{2/3})O_3$-$Pb(Ni_{1/3}Nb_{2/3})O_3$–$Pb(Zr_{1/2}Ti_{1/2})O_3$ ceramics showed that values of d_{33}, Q_m, k_p and density initially increased and later decreased while the T_c slightly increased. Its addition to PZT-PZN ceramics improved the Q_m while the crystal structure changed from tetragonal to rhombohedral with more addition [99]. Its effect on $Pb(Yb_{l/2}Nb_{1/2})O_3$-$PbTiO_3$ ceramics shows that Q_m increased while the T_c remained constant. Resistivity values

increased while the T_c decreased when it was used to dope BNT ceramics [100]. Conflicting results have been reported for BNBT ceramics. Li et al [101] reported that the d_{33} and k_p increased while Q_m decreased but Fan et al. [102] reported both softening and hardening effects as d_{33} and k_p decreased and Q_m increased.

Li et al. [103] reported that Mn enters both the A-and B-sites simultaneously when used to dope (Ca,Sr)$Bi_4Ti_4O_{15}$ due to Mn^{3+} ions while Hirose et al. [104] reported that hardening was obtained. The effects varied with dopant amount; with <1.5 mol% hard ferroelectric effects were obtained and there was more hardening effects between 1.5 and 4.5 mol% but the T_c was not significantly affected. Mn has also been used to dope KNN and "hard effects" were reported with the Q_m, *tan* δ, density being enhanced while d_{33}, k_p and ε_r were lowered. More Mn addition does not significantly alter the obtained T_c values besides changing the ferroelectric properties.

Mn was used in the work because it has been reported to improve the density of KNN ceramics through suppression of grain growth while also decreasing the electrical conductivity of the sample. The aim of this research is to study the effect of adding MnO_2 on the properties of the $(K_{0.44}Na_{0.52}Li_{0.04})$ $(Nb_{0.86}Ta_{0.1}Sb_{0.04})O_3$ ceramics.

5.1.2 Experimental procedure

Table 5.1 Composition and amount of each component powder used for the synthesis

	Amount of powders (grams)							
Composition	K_2CO_3	Na_2CO_3	Li_2CO_3	Nb_2O_5	Ta_2O_5	Sb_2O_3	MnO_2	Total
$(K_{0.44}Na_{0.52}Li_{0.04})(Nb_{0.86}Ta_{0.1}Sb_{0.04})O_3$ (LF4)	7,5381	6,833	0,3664	28,3391	5,478	1,4454	0	50
LF4 + 0.5 mol% MnO_2	7,5381	6,833	0,3664	28,3391	5,478	1,4455	0,1084	50
LF4 + 1.0 mol% MnO_2	7,5054	6,8034	0,3645	28,2163	5,4543	1,4391	0,2168	50
LF4 + 2.5 mol% MnO_2	7,4556	6,7583	0,3621	28,0294	5,4181	1,4296	0,5466	50

K_2CO_3, Na_2CO_3, Li_2CO_3 (99%), Nb_2O_5, Ta_2O_5, Sb_2O_3 (99.9%) and MnO_2 were used as starting powders. The procedures outlined in chapter 4 for sample preparation through the conventional method were used here. In this work, 0, 0.5, 1 and 2.5 mol% respectively of MnO_2 were used to dope $(K_{0.44}Na_{0.52}Li_{0.04})(Nb_{0.86}Ta_{0.1}Sb_{0.04})O_3$ ceramics and the amount of each component raw powder is shown in Table 5.1 . A uniaxial press (170 MPa) and a cold isostatic press (500 MPa) were used and the samples were sintered at 1075 °C for 1 h in air atmosphere. The samples were characterized using density measurements, X-ray

diffraction, high temperature dielectric measurements, polarization and strain hysteresis. Low signal piezoelectric coefficient (d_{33}) values were measured using a displacement transducer connected to a lock-in amplifier which measured the amplitude. Approximately 65 V was applied on the samples while the charge coefficient was calculated from the amplitude value of the lock-in amplifier.

5.1.3 Results

The density values for the samples doped with MnO_2 are shown in Table 5.2. The theoretical density for the undoped sample is 4.79 ± 0.02 g/cm^3 while the relative density was calculated to be 94.3%. The relative density value improved to 96.4% with 1 mol% of MnO_2.

The SEM images of the polished and etched samples in both the undoped and 0.5 mol% Mn doping are shown in Fig. 5.1. For both compositions, quasi-cubic shaped grains are observed on their surfaces. The microstructures of the samples contain both smooth and rough grains possibly due to different crystallographic planes, which behave differently during chemical etching. The higher energetic planes try to revert to lower energetic planes and the result is a steeped/rough surface.

Table 5.2 Density, dielectric and piezoelectric properties of $(K_{0.44}Na_{0.52}Li_{0.04})(Nb_{0.86}Ta_{0.1}Sb_{0.04})O_3$ with different amounts of MnO_2 at room temperature

Amount of MnO_2	0 mol%	0.5 mol%	1 mol%	2.5 mol%
Theoretical density [g/cm^3]	4.79	4.8	4.81	4.83
Relative density [%]	94.3	95.7	96.4	94.4
Coercive field (E_c) [kV/mm]	8.6	5.6	5.8	6.2
Remanent Polarization (P_r) [μC/cm^2]	18.3	8.6	8.3	8.9
Dielectric constant (ε_r) @ 1 kHz	1305	1440	1528	1680
Dielectric loss (tan δ) @ 1 kHz	0.146	0.028	0.018	0.026
Piezoelectric constant (d_{33}) [pm/V]	220	171	171	176
Piezoelectric constant (d^*_{33}) [pm/V]	363	262	331	209

For the undoped sample (Fig. 5.1a), there is an inhomogeneous grain size distribution leading to a bimodal grain size distribution with few big grains surrounded by many small grains. The calculated average grain sizes are 7.3 ± 1.1 μm and 2.1 ± 0.1 μm for the big and small grains respectively. Unevenly distributed relatively large pores are observed at the grain boundaries. The shape of the pores shows that some of them may have been formed due to grain pull-out during the polishing process. In Fig. 5.1b, the sample doped with 0.5 mol% of MnO_2 shows a unimodal grain size distribution with an average grain

size of approximately 2.1 ± 0.1 µm showing that the grain growth anomaly in the undoped sample is suppressed here because Mn is known to create oxygen vacancies which inhibits the movement of the grain boundaries.

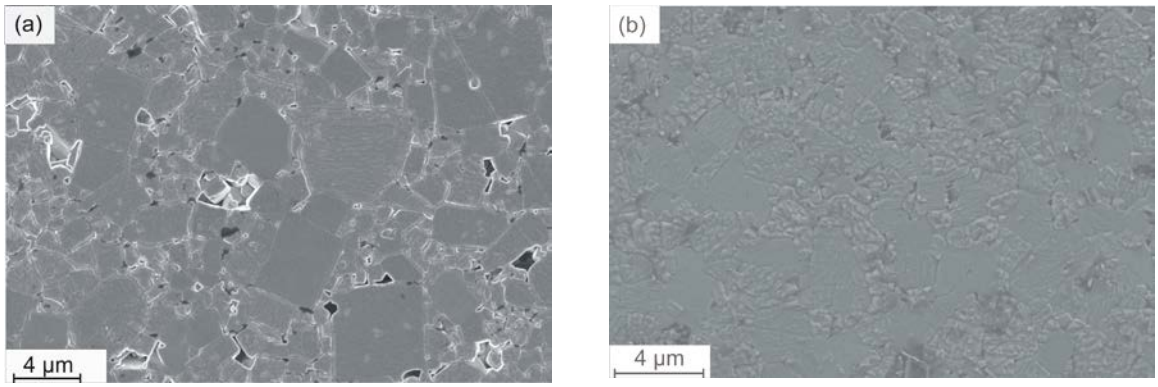

Fig. 5.1 SEM pictures of the thermally etched KNN-$LiTaO_3$-$LiSbO_3$ samples that were sintered at 1075 °C for 1 h (a) undoped (b) 0.5 mol% MnO_2.

Klimov et al. [105] attributed this to the fact that Mn ions occupy both the A- and B-sites of the perovskite lattice. They stated that when PZT is doped with Mn, the site occupancy is determined by the amount of the dopant in the ceramic. Below 0.5 mol%, MnO_2 is believed to act as a donor and above that as an acceptor by occupying A- and B-sites, respectively. It is believed that this behavior also applies to the KNN solid solution [57].

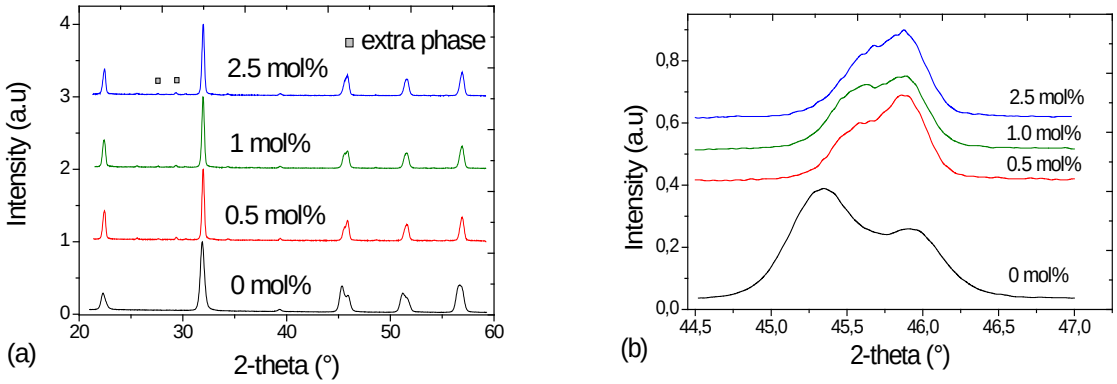

Fig. 5.2 XRD patterns of $(K_{0.44}Na_{0.52}Li_{0.04})(Nb_{0.86}Ta_{0.1}Sb_{0.04})O_3$ ceramics (a) doped with different amounts of MnO_2 (b) zoomed pattern from 44.5° to 47° showing the transition from orthorhombic to tetragonal phase.

The XRD patterns of samples doped with different amounts of MnO_2 are shown in Fig. 5.2a. All the samples have a perovskite structure and in the undoped sample, the orthorhombic structure is the dominant phase and transforms to a predominantly tetragonal structure with increasing amount of dopant. Fig. 5.2b shows the enlarged portion of the diffraction patterns from 44.5° to 47°. Extra peaks (marked with a square) that appear with increasing amounts of the additive show that the solubility of MnO_2 in the $(K_{0.44}Na_{0.52}Li_{0.04})(Nb_{0.86}Ta_{0.1}Sb_{0.04})O_3$ solid solution may be limited and the excess is believed to accumulate at the grain boundaries [106]. Peak search and match analysis was carried out using EVA (search and match software) and a reference pattern from International crystallographic and diffraction data (ICDD) but due to their low intensity, these extra peaks could not be conclusively attributed to any structure.

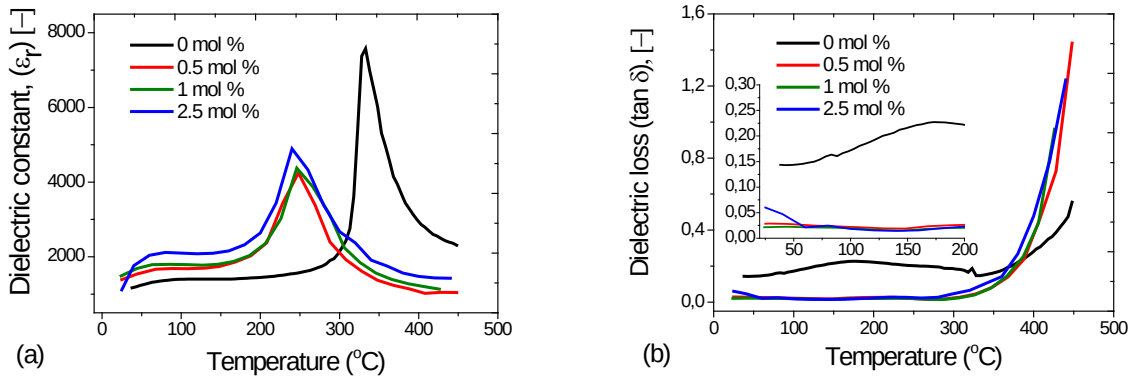

Fig. 5.3 Temperature dependent (a) dielectric constant (ε_r) and (b) dielectric loss ($tan\ \delta$) values for $(K_{0.44}Na_{0.52}Li_{0.04})(Nb_{0.86}Ta_{0.1}Sb_{0.04})O_3$ ceramics doped with MnO_2.

Fig. 5.3a shows the temperature-dependent dielectric constant values while Fig. 5.3b shows the dielectric loss values for the MnO_2 doped samples measured at 1 kHz. $(K_{0.44}Na_{0.52}Li_{0.04})(Nb_{0.86}Ta_{0.1}Sb_{0.04})O_3$ has a polymorphic phase transition (PPT) behavior and has two-phase transition peaks: The first peak which is not pronounced is associated with the T_{T-O} near room temperature while the second is with the tetragonal to cubic phase transition at 333 °C with a dielectric peak of ~ 9500. These values are high when compared to other values in the literature [4]. This could be due to differences in sintering atmosphere used, powder processing methods and parameters used or even from the starting raw powders. Addition of MnO_2 reduces the T_c to about 249 °C which did not significantly decrease with increasing doping amount. Addition of dopants is known to

change the microstructures substantially and affect crystallinity of the samples [78]. The dielectric loss values in Fig. 5.3b show that the addition of dopants reduces the dielectric loss in the samples to approximately 2.5 % at temperatures below 300 °C. The dielectric loss in the undoped sample is however slightly higher than those reported by other researchers [78, 107]. For the manufacturing of devices like transformers that require very low dielectric loss values even at elevated temperatures, the doped composition could be explored as has been attempted by Guo et al. [108].

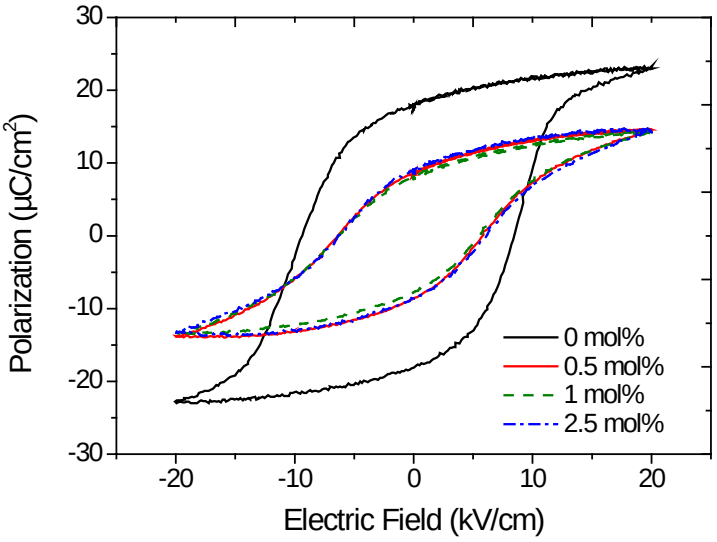

Fig. 5.4 Variation of polarization versus electric field curves for $(K_{0.44}Na_{0.52}Li_{0.04})(Nb_{0.86}Ta_{0.1}Sb_{0.04})O_3$ ceramics doped with MnO_2.

The polarization hysteresis curves for the undoped and doped samples are shown in Fig. 5.4. All the samples show saturation polarization with a 20 kV/cm applied electric field. The addition of Mn lowers both the E_c and the P_r values but there is no significant difference with Mn amount. Additionally the doped ceramics exhibit a lower area of the hysteresis loop and as a result hysteretic losses are lower too. In Fig. 5.5, the strain hysteresis loops for the undoped and doped ceramics are shown. All the samples have the typical butterfly shape which shows that they have ferroelectric properties. The doped ceramics all exhibit a smaller hysteretic behavior than the undoped ceramic. This may be explained by the acceptor doping effect of the dopant on the $(K_{0.44}Na_{0.52}Li_{0.04})(Nb_{0.86}Ta_{0.1}Sb_{0.04})O_3$ ceramics which causes hard ferroelectric effects.

The highest value of the piezoelectric charge coefficient (d_{33}) for the samples as shown in Table 5.2 is from the undoped sample as Mn addition reduced the values This could be attributed to the fact that addition of Mn inhibits domain wall movement which leads to a decrease in the lattice distortion as is evident in the reduced peak splitting in Fig. 5.2.

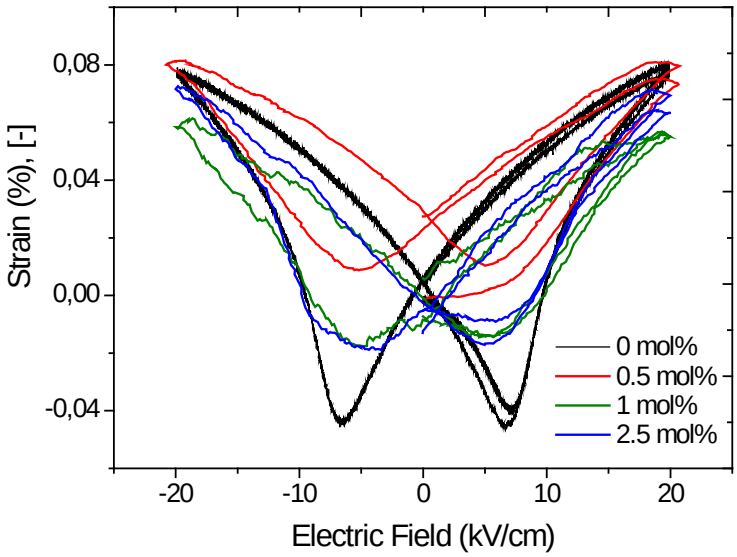

Fig. 5.5 Variation of strain versus electric field hysteresis loops for $(K_{0.44}Na_{0.52}Li_{0.04})(Nb_{0.86}Ta_{0.1}Sb_{0.04})O_3$ ceramics doped with MnO_2.

5.1.4 Discussion

Manganese has several possible valence states and when used as a dopant for $(K_{0.44}Na_{0.52}Li_{0.04})(Nb_{0.86}Ta_{0.1}Sb_{0.04})O_3$ ceramics, a number of different outcomes can occur. The Kröger-Vink notation is used to represent its incorporation into the A-site, B-site or both sides of the lattice. The letter *A* represents the elements on the A-site which could be K, Na or Li while *B* represents the elements on the B-site which could be Nb, Ta or Sb and *O* represents oxygen atom respectively. The assumption is that when the valency is +2 or +3, it can enter the A-site of the lattice and form a cation vacancy as shown in equations (5.3)-(5.4) respectively. Equation 5.5 occurs when there isn't enough oxygen available for sintering in air, the probability of occurrence is low.

$$2MnO \xrightarrow{3ABO_3} 2Mn_A^{\bullet} + 2O_O^{\times} + 2V_A^{'} \tag{5.3}$$

$$Mn_2O_3 \xrightarrow{6ABO_3} 2Mn_A^{\bullet\bullet} + 3O_O^{\times} + 4V_A^{'} \quad (5.4)$$

$$2MnO \xrightarrow{2ABO_3} 2Mn_A^{\bullet} + O_O^{\times} + \frac{1}{2}O_2(g) + 2e' \quad (5.5)$$

When the valency is +3 or +4, it can enter the B-site of the lattice as shown in equations 5.6 and 5.7 respectively. In this case, an oxygen vacancy is expected to be formed in the lattice.

$$Mn_2O_3 \xrightarrow{2ABO_3} 2Mn_B^{''} + O_O^{\times} + 2V_O^{\bullet\bullet} \quad (5.6)$$

$$2MnO_2 \xrightarrow{2ABO_3} 2Mn_B^{'} + 3O_O^{\times} + V_O^{\bullet\bullet} \quad (5.7)$$

The more complex case is when it enters both the A- and B-sites of the lattice which is believed to occur with Mn doping based on the results obtained. Assuming Mn with a valency of +2 on the A-site and +4 on the B-site, the notation will be as shown in equation 5.8 where both cation and oxygen vacancy occurs.

$$2MnO + 2MnO_2 \xrightarrow{4ABO_3} Mn_A^{\bullet} + 2Mn_B^{'} + 5O_O^{\times} + V_A^{'} + V_O^{\bullet\bullet} \quad (5.8)$$

The case of Mn on interstitial sites will not be considered because vacancy defects rather than interstitials has been reported to be the dominant structural defect in perovskite lattice due to its close-packed nature. This has been observed experimentally using neutron powder diffraction [109] and ab-initio simulation in $Pb(Sc_{1/2}Nb_{1/2})O_3$ ceramics [110].

When MnO_2 is used to dope $(K_{0.44}Na_{0.52}Li_{0.04})(Nb_{0.86}Ta_{0.1}Sb_{0.04})O_3$ ceramics, the density of the samples improved slightly. Often in KNN-based ceramics, pores are entrapped within the grains because of grain boundary movements. Mn accumulates at the grain boundaries and inhibits the grain boundary movement leading to smaller size of the average grains. The diffraction patterns show that without Mn, the phase present is mainly orthorhombic and transforms to a tetragonal phase when Mn is introduced which implies that it stabilizes the tetragonal phase.

The temperature dependent dielectric properties plots show that the dielectric constant peaks decrease with increasing amount of Mn. The T_c decreases from 333 °C to 249 °C but there is no significantly difference with more Mn. First principles-based calculations of $Pb(Sc_{1/2}Nb_{1/2})O_3$ predicted that the introduction of Pb vacancies reduced the T_c of the samples and attributed this to relatively large internal inhomogenous electric fields

generated by these vacancies [110]. This idea can also be used to explain the decrease in T_c with Mn doping. The dielectric constant peaks broadened slightly as the dopant was added due to increase in site disorderliness and therefore local compositional fluctuation. The decrease in energy barriers due to the vacancies promote enhanced fluctuations between the energy minima below the T_c.
The polarization and strain hysteresis curves as well as the d_{33} values decreased with the addition of Mn. The P_r was lowered from ~18 μC/cm^2 to ~9 μC/cm^2, the E_c from ~8.5 kV/cm to ~6.2 kV/cm and the d_{33} from ~220 pC/N to ~171 pC/N. The d^*_{33} values from high signal measurements are higher than d_{33} values from low signal because the high electric field used introduces more irreversible polarization contribution than with low signal measurement.

The effect of MnO_2 on $(K_{0.44}Na_{0.52}Li_{0.04})(Nb_{0.86}Ta_{0.1}Sb_{0.04})O_3$ ceramics is mixed between those caused by oxygen and cation vacancy as shown in equation 5.8. This implies that Mn acts both like a donor and an accpetor in the ceramic leading to lower values of P_r, E_c, d_{33}, $tan\ \delta$, average grain size and increased dielectric constant at lower temperatures. In order to verify this, special characterization techniques like electron paramagnetic resonance (EPR), XANES and EXAFS which can detect the valence and position of elements in the lattice are required. It has been reported in $(PbZnNb)_{0.2}$-$(ZrTi)_{0.8}$ ceramics doped with MnO_2 that Mn^{2+} and Mn^{3+} states coexists in the sample [111].

5.1.5 Summary

The effect of adding MnO_2 on the properties of $(K_{0.44}Na_{0.52}Li_{0.04})(Nb_{0.86}Ta_{0.1}Sb_{0.04})O_3$ ceramics has been investigated. The density values improved with MnO_2 addition while grain growth was inhibited. The temperature of the phase transitions, remanent polarization, dielectric loss, coercive field and d_{33} values all decreased when Mn was added to the sample. It is believed that Mn is incorporated into both the A- and B-site of the lattice which leads to mixed dielectric and piezoelectric properties results.

5.2 Effect of substituting Nb with Sb on the properties of $(K_{0.5}Na_{0.5})NbO_3$ ceramics

5.2.1 Introduction

Research into lead-free single and polycrystalline $(K_xNa_{1-x})NbO_3$ ceramics started in the late 1950's but the interest waned when PZT became the piezoceramics of choice due to its superior properties. The interest in this ceramic was renewed by Saito et al. [61] when they reported that using texture and isovalent substitution of both A- and B-site elements, the piezoelectric properties can be greatly improved. Combined Li, Ta and Sb substitutions are known to result in one of the highest piezoelectric properties in the KNN system [77, 78]. The effect of only Li on the properties of KNN has been reported in the literature [53, 112]. The effect of Ta which is expected to enter the B-site of the lattice based on valence and ionic radius considerations has also been reported [113]. A combination of Li and Ta [61, 114] as well as Li and Sb on the A- and B-sites respectively of the lattice have been reported [115]. There is however very little report in the literature on the effect of only Sb on the structure and properties of KNN. Sb and Mn have been used to dope KNN and it was reported that Mn only served as a sintering aid but it is possible that there are other effects [57, 116]. In this work, the effect of substituting Nb with Sb on the piezoelectric, dielectric, crystallographic and microstructural properties of $K_{0.5}Na_{0.5}NbO_3$ was investigated. The objective is to understand the effect of substituting Nb with Sb on the properties of $(K_{0.5}Na_{0.5})NbO_3$ ceramics.

5.2.2 Experimental procedure

$(K_{0.5}Na_{0.5})(Nb_{1-x}Sb_x)O_3$ where x = 0; 0.02; 0.14 was synthesized through the mixed-oxide route with the following powders; K_2CO_3, Na_2CO_3, (99%), Nb_2O_5 and Sb_2O_3 (99.9%). The compositions and amounts of each component powder used in the work are shown in Table 5.3. The powders were put inside a custom made silicone mould and pressed for 2 min at 300 MPa with a cold isostatic press while sintering was carried out at between 1080 °C and 1100 °C respectively for 2 h in air. Samples with composition (x=0, 0.02, 0.06, 0.1, 0.12 and 0.14) sintered at 1080 °C were thermally etched for microstructural examination. SEM and quantitative energy dispersive spectroscopy were used to study the microstructure evolution. The standards used were the following natural minerals: Quartz (O), Albite ($NaAlSi_3O_8$) (Na), Orthoclase ($KAlSi_3O_8$) MAD-10 (K), Nb (Nb), Sb (Sb). Density, X-ray diffraction, high temperature dielectric properties, resistance measurement, impedance

measurement, polarization and strain hysteresis techniques were used to characterize the samples.

Table 5.3 Composition and amount of each component powder used for the synthesis

	Amount of powders (grams)				
Composition	K_2CO_3	Na_2CO_3	Nb_2O_5	Sb_2O_3	Total
$(K_{0.5}Na_{0.5})NbO_3$	7,8377	6,0115	30,1507	0	44
$(K_{0.5}Na_{0.5})(Nb_{0.98}Sb_{0.02})O_3$	7,8273	6,0036	29,5086	0,6604	44
$(K_{0.5}Na_{0.5})(Nb_{0.96}Sb_{0.04})O_3$	7,817	5,9957	28,8682	1,3191	44
$(K_{0.5}Na_{0.5})(Nb_{0.94}Sb_{0.06})O_3$	7,8067	5,9877	28,2295	1,9761	44
$(K_{0.5}Na_{0.5})(Nb_{0.92}Sb_{0.08})O_3$	7,7964	5,9798	27,5924	2,6313	44
$(K_{0.5}Na_{0.5})(Nb_{0.9}Sb_{0.1})O_3$	7,7861	5,9718	26,9571	3,2848	44
$(K_{0.5}Na_{0.5})(Nb_{0.88}Sb_{0.12})O_3$	7,7758	5,9641	26,3234	3,9366	44
$(K_{0.5}Na_{0.5})(Nb_{0.86}Sb_{0.14})O_3$	7,7657	5,9563	25,6913	4,5866	44

5.2.3 Results

The effect of sintering at different temperatures and substituting Nb with Sb on the bulk density of KNN are shown in Table 5.4. For pure KNN, sintering at 1080 °C gave the highest density value (94 ± 1.0%) which decreases as the sintering temperature increases. Substituting with up to 8 mol% Sb did not show any consistent trend in density but between 10 and 14 mol%, the density value increases as the sintering temperature increases. This shows that substitution with substantial amount of Sb to KNN increases the optimum sintering temperature. This observation is similar to a literature report by Lin et al. [57] although a small amount of MnO_2 was used in their work.

Table 5.4 Density of $(K_{0.5}Na_{0.5})(Nb_{1-x}Sb_x)O_3$ sintered at 1080 °C, 1090 °C and 1100 °C respectively. The lattice parameters and resistance values were obtained from samples sintered at 1080 °C.

Bulk density (g/cm^3)				Lattice parameter (Å)			Resistivity (Ω.cm)	K_p	Q_m	N_p
mol% Sb	@1080 °C	@1090 °C	@1100 °C	a	b	c	@1080 °C	@1080 °C	@1080 °C	@1080 °C
0	4.22 ± 0.04	4.11 ± 0.04	3.99 ± 0.05	3.94744	5.64043	5.6702	1.35E9 ± 7.93E8	0.27	17.3	3153
2	4.18 ± 0.07	4.25 ± 0.04	4.23 ± 0.02	3.94986	5.63788	5.6643	9.13E9 ± 1.84E9	0.38	12.4	3219
4	4.06 ± 0.03	4.21 ± 0.02	4.19 ± 0.01	3.95444	5.63569	5.6583	2.22E11 ± 1.31E11	0.46	6.20	2254
6	4.14 ± 0.06	4.23 ± 0.02	4.24 ± 0.02	3.95432	5.63158	5.6461	1.07E11 ± 3.52E10	0.29	16.5	2984
8	4.3 ± 0.07	4.18 ± 0.04	4.19 ± 0.02	3.95774	5.62538	5.6381	3.66E9 ± 2.8E9	0.33	16.4	2717
10	4.07 ± 0.05	4.26 ± 0.02	4.57 ± 0.03	3.95901	5.61942	5.6322	8.29E8 ± 1.11E8	0.27	13.4	2634
12	4.35 ± 0.05	4.37 ± 0.05	4.53 ± 0.04	3.96627	5.61309	5.6406	3.13E9 ± 9.2E8	0.32	10.3	3062
14	4.29 ± 0.15	4.33 ± 0.04	4.56 ± 0.03	3.96248	5.61151	5.6343	2.12E9 ± 1.31E9	0.25	9.68	2275

The XRD patterns for $(K_{0.5}Na_{0.5})(Nb_{1-x}Sb_x)O_3$ ceramics sintered at 1080 °C are shown in Fig. 5.6a. The pure KNN pattern shows minute extra peaks which could not be identified from the database while the patterns between 2 and 10 mol% Sb content have a single orthorhombic phase. Above 10 mol%, extra peaks begin to appear and a search and match operation using EVA indicates that the extra peaks are related to PDF 01-083-1899 from ICDD database. This phase has a formula ($K_2NaSb_3O_9$) with a Laue group (*cP64*) and crystallizes in a cubic structure. It is an ordering variant of $KSbO_3$ with splitting of one of the cation sites. Lin et al. [57] reported that Sb is believed to diffuse into the KNN lattice and form a solid solution with a single perovskite structure but this occurs when its solid solubility limit is not exceeded. It could also be that the addition of Mn increases the solid solubility limit of Sb in KNN thereby suppressing the formation of a second phase.

An enlarged portion of the patterns between 44.5° and 47° is shown in Fig. 5.6b. When more than 8 mol% of Sb is substituted, the phase transforms from an orthorhombic to a pseudo-cubic phase similar to a report in the literature [57]. Pseudo-cubic in this case means that the phase looks cubic in outer form but is not isometric in internal structure or in how the properties are distributed. Based on the difference in ionic radius between Sb

(60 pm) and Nb (64 pm) with a coordination number of 6, it is expected that the lattice distortion will increase but this did not occur and rather a structure that is pseudo-cubic with increasing Sb content was formed.

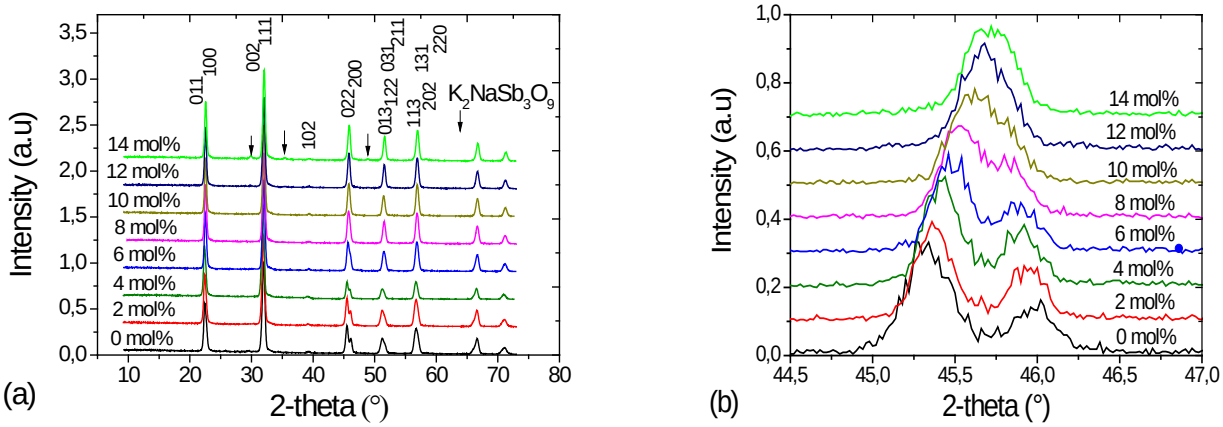

Fig. 5.6 XRD patterns of the polished surfaces of $(K_{0.5}Na_{0.5})(Nb_{1-x}Sb_x)O_3$ ceramics sintered at 1080 °C for 2 h where x ranges from 0 to 14 mol% Sb (a) showing 2θ values from 10° to 73° and the extra peaks shown with arrows are related to $K_2NaSb_3O_9$ (b) Enlarged pattern from 44.5° to 47° showing the reduction in peak splitting as the amount of antimony substituted increased.

$KNbO_3$ with PDF number 01-071-0946 in the ICDD database was used as a reference because it is isostructural with KNN. The whole powder pattern decomposition was carried out using the Le bail method in Topas. With increasing amount of Sb in KNN, the lattice constant a_{ortho} increased while b_{ortho} and c_{ortho} decreased resulting in a decrease of the volume of the unit cell as shown in Table 5.4. Fig. 5.7a shows the microstructure of a polished and thermally etched pure KNN sample with many small and few big pores located mainly at the grain boundary junctions. The grains have a unimodal size distribution with an average size of 1.51 ± 0.9 µm. When 2 mol% of Sb is added (Fig. 5.7b), solute precipitation could be observed mainly at the grain boundaries. The grain growth increases with an average size of 2.64 ± 1.53 µm. This size distribution shows that some grains were quite large while others were small. As more Nb is substituted with Sb, the growth of the new phase also increases forming well ordered clusters which are located mainly at the boundaries (Fig. 5.7c).

The size of the grains decreases with increasing Sb content with an average size of

2.47 ± 1.44 µm for 6 mol% Sb. 10 mol% Sb content reduces the grain size to 1.24 ± 0.59 µm (Fig. 5.7d). With 12 mol% Sb substitution, (Fig. 5.7e), the growth of the new phase becomes more pronounced forming an interconnected network both inside the grains and at the boundaries. The average grain size increases to 1.5 ± 0.58 µm. With 14 mol% Sb (Fig. 5.7f), the new phase has grown such that it almost completely covers the grains. This observation is similar to the report by Li et al. where the Sb rich phase showed plate-like shapes [71]. The grain decreases further with an average size of 1.04 ± 0.76 µm.

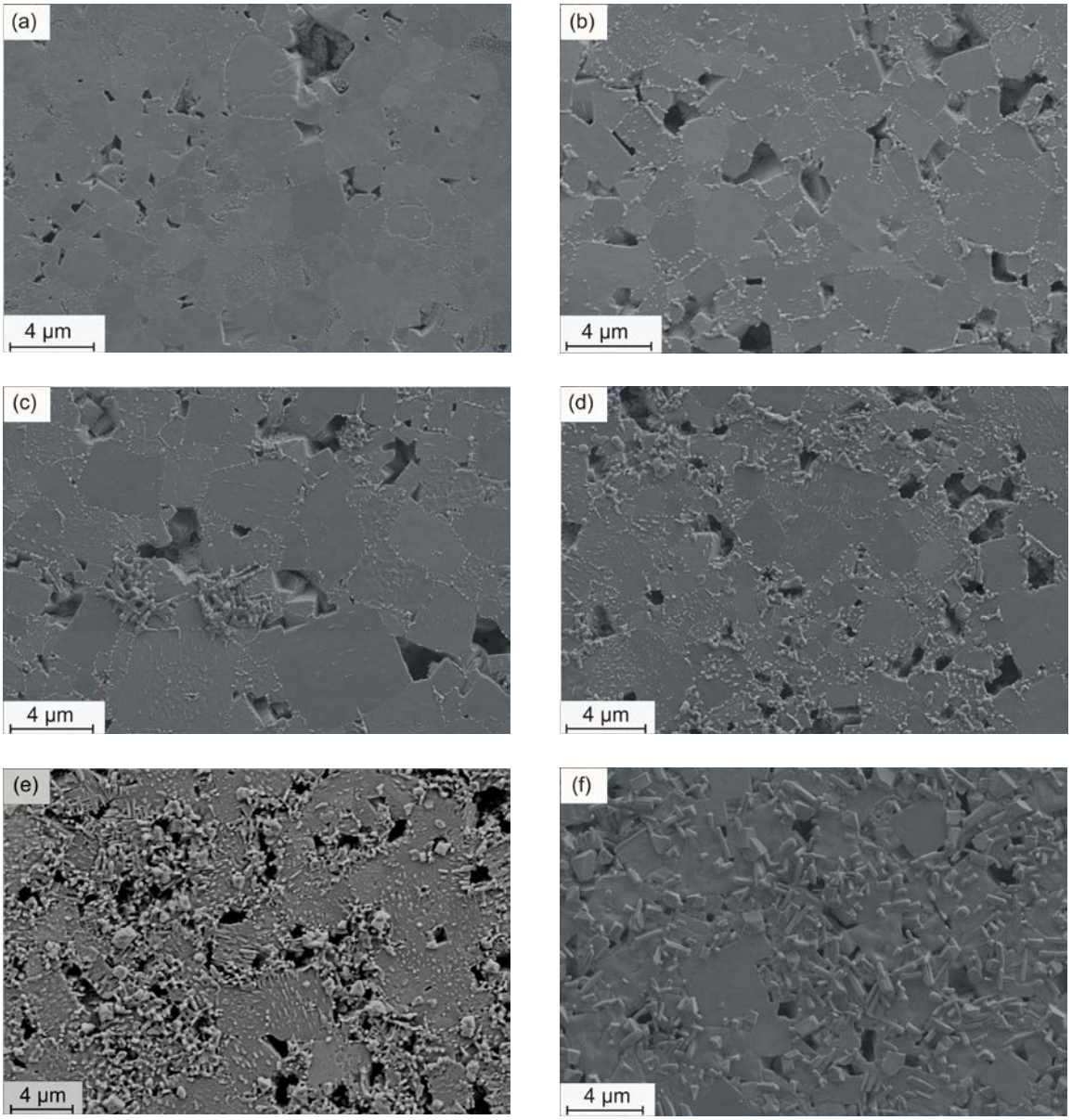

Fig. 5.7 SEM micrographs of KNN ceramics sintered at 1080 °C and doped with 0, 2, 6, 10, 12 and 14 mol% Sb (Fig. 5.7a, Fig. 5.7b, Fig. 5.7c, Fig. 5.7d, Fig. 5.7e and Fig. 5.7f respectively). The second phases can be seen clearly at both the grain boundary and inside the grains.

Quantitative element analysis was also carried out by selecting an area of approximately 1 µm by 1 µm on the surface of the sample. In addition, scans were carried out on the main and precipitate phase for the sample with 14 mol% Sb. The atomic percent of Na, K, Nb, Sb and O were normalized assuming ABO_3 stoichiometry in all cases and a summary of the quantitative element analysis result for the samples is shown in Table 5.5. The values

were obtained after iterating 5 times and then normalizing them. In the main grains, while Nb amounts are more or less within the limits, K and Na amounts are always deficient for all the samples. In most cases, the measured value for Na was on average about 30 % less than the expected value while K was less by about 15 %. The amount of Sb was less in most cases by about 20 % while oxygen amount in all cases was higher than the expected value.

Table 5.5 EDX element ratio showing the actual and expected atom % of the different elements in the $(K_{0.5}Na_{0.5})(Nb_{1-x}Sb_x)O_3$ ceramics

Element	Atomic %	0 mol%	2 mol%	6 mol%	10 mol%	14 mol% (dark)	14 mol% (bright)
O	Actual	65.63	67.22	65.79	65.48	68.38	70.03
	Expected	59.99	59.98	59.99	59.99	59.99	59.99
Na	Actual	6.53	7.19	7.21	6.91	6.58	6.31
	Expected	10.03	10.04	10.04	10.03	10.04	10.04
K	Actual	8.33	7.94	8.36	8.79	7.92	7.86
	Expected	9.99	9.99	9.99	9.99	9.99	9.99
Nb	Actual	19.5	17.44	17.71	17.08	15.07	9.31
	Expected	19.98	19.58	18.78	17.98	17.18	17.18
Sb	Actual		0.2	0.92	1.74	2.05	6.49
	Expected		0.4	1.2	2	2.8	2.8

The temperature dependence of the dielectric constant values for the samples measured at 100 kHz is as shown in Fig. 5.8a. A dielectric constant value of ~700 is obtained for pure KNN at room temperature which is high compared to what has been previously reported in the literature [8, 47]. Both phase transition points (T_c and $T_{T\text{-}O}$) shifted to lower temperatures with increasing Sb content. The decrease in the lattice constants with increasing Sb substitution accompanies the lowering of the Curie point. The values obtained for both phase transitions for pure KNN (T_c = 412 °C, $T_{T\text{-}O}$ = 202 °C) are similar to what has been reported earlier [8]. The $T_{T\text{-}O}$ could not be observed for the sample with 14 mol% Sb while the peaks broaden at both $T_{T\text{-}O}$ and T_c with increasing Sb content indicating decreasing ferroelectricity in the sample.

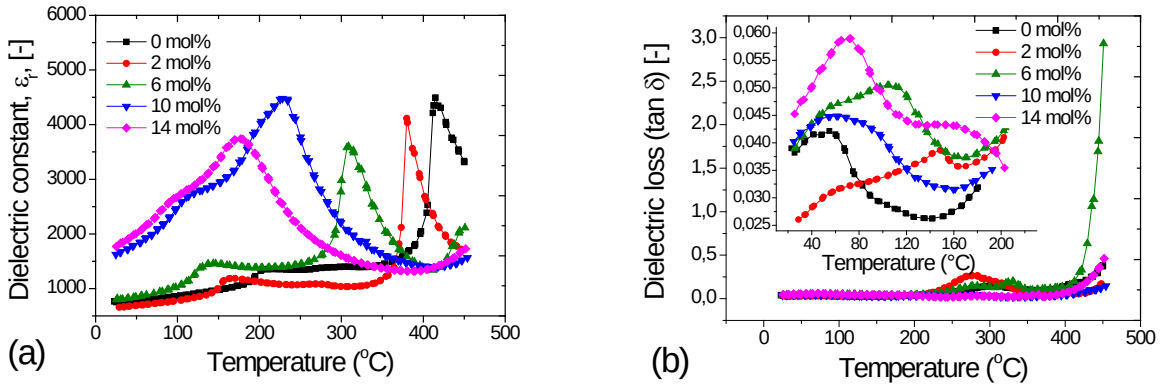

Fig. 5.8 (a) Dielectric constant (ε_r) values for $(K_{0.5}Na_{0.5})(Nb_{1-x}Sb_x)O_3$ ceramics measured at 100 kHz as a function of temperature. (b) Dielectric loss (tan δ) values for the same compositions as a function of temperature measured at 100 kHz. The inset shows an enlarged portion of the diagram from 25 °C to 200 °C.

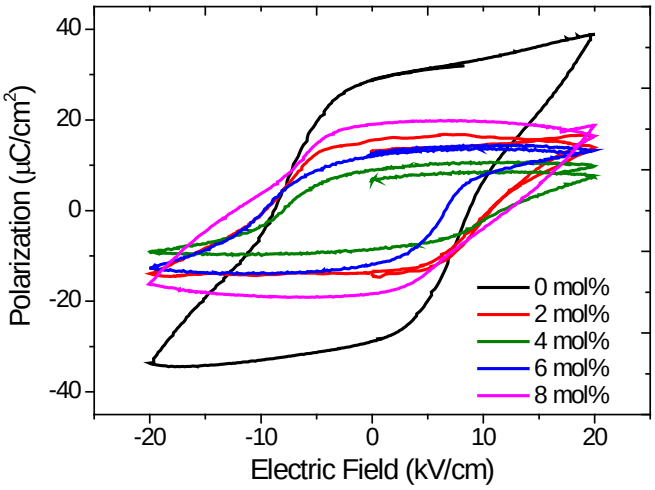

Fig. 5.9 Variation of the polarization versus field (P-E) hysteresis loops for $(K_{0.5}Na_{0.5})(Nb_{1-x}Sb_x)O_3$ ceramics sintered at 1080 °C.

The temperature dependence of the dielectric loss measured at 100 kHz is shown in Fig. 5.8b. At close to room temperature, 2 mol% Sb gives lower loss values (0.026) compared to pure KNN but as Sb content increases, the loss values increases. The inset in Fig. 5.8b shows an enlarged region up to 200 °C indicating differences in loss values with increasing temperature and different amounts of Sb. At temperature above 200 °C, the samples with low Sb amount have higher loss values when compared with those with higher Sb content.

Generally the loss values of the samples are moderate considering that there are A-site vacancies in the ceramic.

The resistivity values for the samples measured at room temperature are shown in Table 5.4 The highest value is obtained with 4 mol% while the lowest is with 10 mol%. Initial Sb substitution increases the resistivity up to 10^{11} Ωcm but it decreases when more than 6 mol% is added. The polarization-electric field plot of samples with different molar percentages of Sb is shown in Fig. 5.9. With a 20 kV/cm field, well saturated hysteresis curves are obtained for samples with up to 8 mol% Sb but with more addition, good hysteresis curves could not be obtained due to high leakage current. The P_r value for pure KNN is ~27 μC/cm^2 while the E_c is ~8.8 kV/cm. Substitution with Sb decreases the P_r for all the samples but there is no significant change in the E_c (~9 kV/cm) values. The sample with 4 mol% Sb however has the lowest P_r (9.5 μC/cm^2) values. There is no consistent trend in the obtained N_p values which ranges from 2254 (4 mol% Sb) to 3219 (2 mol% Sb). All the samples showed high N_p values which indicate its suitability for high frequency application.

5.2.4 Discussion

Substitution of Nb with Sb in KNN ceramics below 10 mol% did not lead to any significant difference in the density values but with both higher Sb amount and sintering temperatures, density values with up to 94±1% are obtained. The increase in density values could be due to the formation of an extra phase detected with the XRD. This phase is mainly present at the grain boundaries and can act to impede the movement of the grain boundary.

As the amount of Sb added to the KNN ceramics increased, the phase present gradually transformed from an orthorhombic to a pseudo-cubic phase and an extra phase was also formed. A literature report on a similar composition identified a new phase using temperature-dependent dielectric measurement to have a rhombohedral symmetry [117]. A possible reason why an extra phase was formed may be due to the fact that Nb and Sb are both transition metals with many oxidation states. The valence state of Nb and Sb in the lattice should in principle be the same but it is possible that their valence states have been altered. The ionic radii of these elements vary with their oxidation states. For a coordination number (CN) of 6, Nb has ionic radii of 64 pm and 68 pm for valence states of +5 and +4 respectively. Sb with a CN of 6 has ionic radii of 60 pm and 76 pm for

valence states of +5 and +3 respectively. When both elements have a valent state of +5, their difference is negligible but if the valent state changes, cation vacancies will be introduced which limits the solubility limit of the elements in each other due to ionic mismatch.

All the etched samples doped with Sb have precipitates at their grain boundaries. Chemical etching in oxide ceramics affect grains with different crystallographic planes differently thereby revealing a significant amount of the grain boundary precipitate [118]. This grain boundary segregation occurred mainly due to ionic misfit in the perovskite lattice. Rod-like grains appeared at the grain boundaries of samples with more Sb content. These rod-like grains contain the Sb rich phase with close to 3 times more Sb content than in the normal grains. This shows that Sb has a tendency to concentrate mainly at the grain boundaries in KNN ceramics. One of the main driving forces for grain boundary segregation is the difference in electrostatic potential between the matrix and the new phase. It occurs due to the presence of aliotropic solutes which tend to segregate in the space charge region [119]. The grain size of the samples decreased with increasing amount of Sb possibly because the excess solute accumulates at the grain boundaries and acts as a drag during the sintering process.

High dielectric constant and P_r values were obtained for the undoped sample possibly due to a slight change in the stoichiometry of the ceramic due to the presence of A-site vacancies in the perovskite. ZrO_2 balls were used as the grinding medium and it is possible that Zr may have been introduced during sample processing. The A-site vacancy may also explain the decrease in the volume of the unit cell with Sb doping. As the amount of Sb added to the sample increases, the dielectric constant values at lower temperatures increases while the T_c and $T_{T\text{-}O}$ decreases. According to Bellaiche et al. [110] based on the first principles investigation of $Pb(Sc_{1/2}Nb_{1/2})O_3$ ceramics, the reduction in T_c is due to a relatively large internal inhomogenous electric fields generated by Pb vacancies. This explanation equally applies here because the EDX analysis clearly shows that there were A-site vacancies. The density values of the samples can also affect the obtained Q_m values with higher values being obtained from denser samples. The dielectric response of the samples with increasing Sb amount shows an increase in the diffuse scatter and broadening at the ferroelectric transition due to decrease in the energy barriers that are caused by cation vacancies which increases the fluctuations between the energy minima below the T_c.

5.2.5 Summary

The effect of substituting Nb with Sb on the properties of KNN was investigated. A phase change from an orthorhombic to a pseudo-cubic phase was observed above 8 mol% Sb and the microstructures of the samples containing Sb show rod-like solute segregation mainly at the grain boundaries but also inside the grains. The temperatures of both phase transitions were lowered with increasing Sb content such that above 10 mol% Sb, the $T_{T\text{-}O}$ decreases to below room temperature. At temperatures below 100 °C, substituting more Nb resulted in higher relative permittivity and dielectric loss values. Saturation polarization was attained for samples with ≤ 8 mol% but no hysteresis loop was obtained for samples with > 8 mol% due to high leakage current. The sample with 4 mol% Sb substitution gave the best properties (k_p = 0.46, Q_m = 6.2, N_p = 2296).

6 High-throughput synthesis

6.1 Effect of Bi on the A- and B-sites of KNN-based piezoelectric ceramics investigated using HTE method

6.1.1 Introduction

It is known that the main consitituent of PZT ceramics which enables high piezoelectric properties is the element Pb. It has similar chemical properties with Bi and both are heavy elements but Bi has lower toxicity. Some Bi-based ceramics have ferroelectric characteristics with high T_c values. It is believed that doping of KNN ceramics with Bi may result in higher piezoelectric properties. Few reports can be found in the literature where the properties of KNN ceramics were modified with Bi. In one of them, it was suggested that Bi_2O_3 only acts as a sintering aid to KNN due to its low melting temperature [120]. Both phase transition temperatures and the P_r and E_c values were lowered when Bi was added. The piezoelectric charge coefficient increased when 0.6 wt% of Bi was added to KNN while an extra phase was observed in the diffraction pattern with more Bi addition. In another report, the Bi-doped KNN samples were sintered in both air and oxygen atmospheres and the reported piezoelectric properties were higher than for pure KNN but the T_c was lower [121]. Suzuki et al. [122] added Bi to KNN ceramics also containing Li, Ta and Sb and reported that the electrical insulation of the samples improved which enhanced the poling process. Rödel et al. [123] in a review article on lead-free ferroelectric ceramics stated that Bi can be used to replace elements on either the A - and B-sites of the perovskite lattice. In this work, very small amounts of Bi were used to substitute K and Na on the A-site while keeping the B-site elements constant and later both Nb and Ta on the B-site were substituted while keeping the A-site elements constant for the KNN-based compositions. The objective of this work is to investigate the effect of Bi on the properties of KNN-based ceramics and to show that the HTE method can also be used to produce ceramic samples with similar properties as those produced from the conventional method.

6.1.2 Experimental procedure

Table 6.1 Calculated composition and dosed amount of each component powder used for the synthesis in KNN-A ceramics. Other compositions are similar in calculated and the actual amount of powders dosed and will not be presented

		Calculated amount of the powders (milligrams)							
	mol% Bi	K_2CO_3	Li_2CO_3	Na_2CO_3	Nb_2O_5	Ta_2O_5	Sb_2O_3	Bi_2O_3	Total
Calculated	0	195.96		150.3	753.74			0	1,100
Actual		196		151.1	754			0	1,101
Calculated	0.001	195.77		150.16	753.41			0.66	1,100
Actual		196,4		150.6	753.6			0.5	1,102
Calculated	0.002	195.59		150.02	753.07			1.32	1,100
Actual		195,9		150.7	753.1			1.3	1,103
Calculated	0.003	195.4		149.88	752.74			1.98	1,100
Actual		195.7		150.7	752.9			2.1	1,101
Calculated	0.004	195.22		149.73	752.41			2.64	1,100
Actual		195.5		150.3	752.5			2.7	1,101
Calculated	0.005	195.04		149.59	752.08			3.3	1,100
Actual		195.1		149.9	752.3			3.3	1,101
Calculated	0.006	194.85		149.45	751.74			3.95	1,100
Actual		194.9		150	751.5			4.1	1,101
Calculated	0.007	194.67		149.31	751.41			4.61	1,100
Actual		194.7		149.7	751.6			4.7	1,101
Calculated	0.008	194.48		149.17	751.08			5.27	1,100
Actual		195.1		149.9	751.3			5.7	1,102
Calculated	0.009	194.3		149.03	750.75			5.92	1,100
Actual		194.5		149.4	750.7			5.8	1,100
Calculated	0.01	194.12		148.89	750.42			6.58	1,100
Actual		194.7		149.1	749.6			6.8	1,100

$(K_{0.5}Na_{0.5})NbO_3$ with Bi on the A- and B-sites abbreviated as KNN-A and KNN-B respectively, $(K_{0.48}Na_{0.48}Li_{0.04})(Nb_{0.9}Ta_{0.1})O_3$ with Bi on the A and B-sites as KNNLT-A, and KNNLT-B respectively and $(K_{0.48}Na_{0.48}Li_{0.04})(Nb_{0.85}Ta_{0.1}Sb_{0.05})O_3$ as (KNNLST) were produced using the HTE method. Bi_2O_3 was added to the KNN-based compositions from 0 mol% to1 mol% in the following steps; 0; 0.001; 0.01. 1,100 mg of powders was dosed for each composition. The amount of the component powders used for the synthesis for

KNN-A compositions are shown in Table 6.1. The calculated and actual amounts of powders dosed are in some cases different because either the powder amounts are sometimes too small or the flowability of the powder is too poor. After the milling and calcination process, the powders were cold isostatically pressed at 300 MPa for 2 min. Sintering was in air atmosphere between 1090 °C – 1120 °C for 1 h at a heating and cooling rate of 2 °C/min and 10 °C/min respectively. XRD patterns were recorded at 6 different positions on the surface of the sample between 20° and 60° to examine sample homogeneity. Density determination, dielectric properties measurement, resistance measurement and hysteresis were used to characterize the samples.

6.1.3 Results

The density values obtained for the samples as a function of substituted Bi amount is shown in Table 6.2. The temperature required for sintering the samples when Bi is added increased but it was expected that since Bi_2O_3 has a low melting point (820 °C), the sintering temperature will be reduced. This effect has been observed by Du et al. [120] for KNN ceramics modified with Bi. A lot of samples with slightly different compositions were produced using this method and changes in composition also affect the optimum sintering temperature. To increase the processing time of the ceramics, samples with similar compositions were sintered with the same temperature. Some samples were optimally sintered while others were not and low density values were obtained. No defined trend in density values with the amount of Bi added was obtained and this is one of the setbacks of the HTE method.

Table 6.2 Density values for the KNN ceramics as a function of Bi amount added

	Density (g/cm^3)				
Bi amount (mol%)	KNN-A	KNN-B	KNNLT-A	KNNLT-B	KNNLST
0	4.215	4.176	4.188	4.476	4.085
0.1	4.259	4.358	4.348	4.351	4.386
0.2	4.204	4.419	4.272	4.454	4.302
0.3	4.27	4.043	4.417	4.421	4.349
0.4	4.2	4.171	4.262	4.508	4.343
0.5	4.14	4.115	4.179	4.464	4.5
0.6	4.285	4.278	4.298	4.54	4.409
0.7	4.291	4.112	4.609	4.547	4.406
0.8	4.124	4.276	4.512	4.354	4.46
0.9	4.084	4.29	4.469	4.382	4.451
1.0	4.355	4.404	4.468	4.449	4.488

The density values for KNNLT-B and KNNLST compositions are more consistent with an average density of 4.4 g/cm^3. When compared to the values in the literature with similar compositions, the obtained values are acceptable [120, 124]. To investigate the consistency of the results produced using the HTE method, a composition was selected from KNNLST from which 20 samples were produced. The average density value obtained was 4.42 ± 0.14 g/cm^3 which show that samples with reproducible density values can be produced.

The X-ray diffraction patterns for the samples are shown in Fig. 6.1. For KNN-A compositions, single perovskite phases with orthorhombic symmetry are obtained up to 0.9 mol%. With 1 mol% of Bi, an extra phase which is related to $K_2BiNb_5O_{15}$ (PDF 00-046-0317 from ICDD) is observed. A previous study on this composition showed that with more than 0.7 wt% Bi, a similar phase ($KBi_2Nb_5O_{16}$) was obtained [120]. The KNN-B compositions as shown in Fig. 6.1b also reveal single phases with orthorhombic symmetry up to 0.8 mol% Bi and a pseudo-cubic phase above this amount. A phase boundary between two orthorhombic phases is observed between 0.4 and 0.5 mol%. A similar study on pure KNN modified with both Li and Bi revealed a phase boundary but from an orthorhombic phase to a tetragonal phase [124]. For KNNLT compositions with Bi on both the A- and B-sites, a single phase is obtained up to 1 mol%. For KNNLT-A in Fig. 6.1c, a two-phase boundary between an orthorhombic and a tetragonal phase was observed at ~ 0.6 mol% while for KNNLT-B, (Fig. 6.1d), a two-phase mixture is present up to 0.3 mol%. The tetragonal phase becomes dominant with more Bi addition which indicates that Bi stabilizes the tetragonal phase in KNNLT ceramics. The diffraction patterns for KNNLST compositions (Fig. 6.1e) show that the tetragonal phase is the dominant phase up to 0.6 mol% and above this amount, a pseudo-cubic phase is formed.

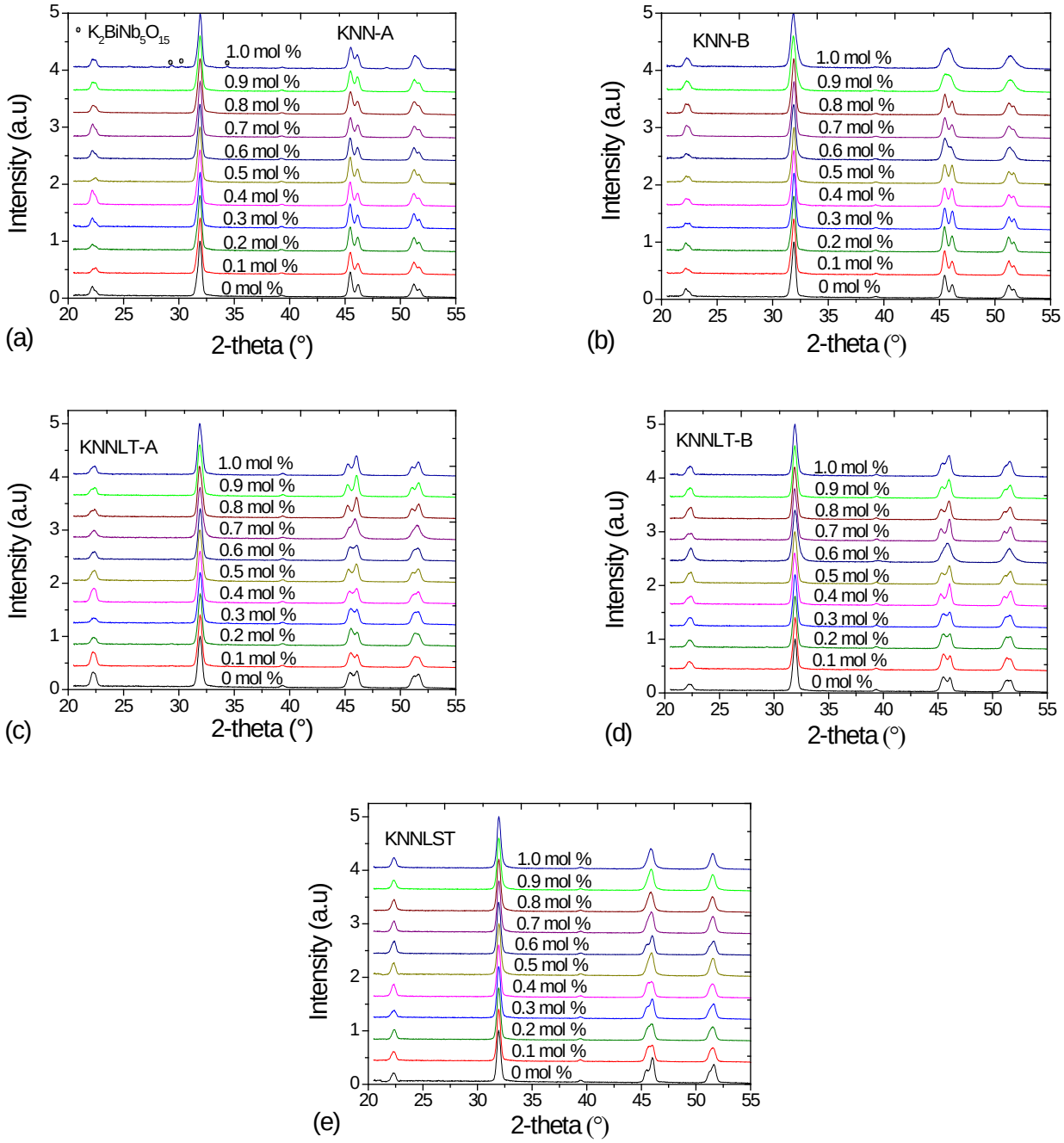

Fig. 6.1 XRD patterns of the polished surfaces of KNN-based compositions modified with Bi. Figs. 6.1a, 6.1b, 6.1c, 6.1d and 6.1e correspond to KNN-A, KNN-B, KNNLT-A, KNNLT-B and KNNLST compositions respectively.

The SEM images of the samples are shown in Fig. 6.2. A unimodal grain size distribution with an average grain size of 2.5 ± 0.8 µm is obtained for pure KNN ceramics (Fig. 6.2a).

There are pores at the grain boundaries of the sample. When Bi is added to either the A- or the B-sites of the KNN lattice, the average grain size decreased. There are few pores at the grain boundaries with an average grain size of 2.2 ± 0.8 µm for KNN-A doped with 1 mol% Bi (Fig. 6.2b). There are lots of pores at the grain boundaries and the grains are even smaller with an average size of 0.9 ± 0.4 µm for KNN-B with 1 mol% Bi (Fig. 6.2c). Addition of both Li and Ta to KNN has been reported to considerably improve its sinterability [61]. There is less porosity at the grain boundaries for the KNNLT composition without Bi (Fig. 6.2d). A unimodal size distribution is observed and the average grain size is 2.5 ± 1.0 µm. No significant difference is observed in the microstructures of KNNLT-A and KNNLT-B in Fig. 6.1e and Fig. 6.2f and the average grain sizes are 2.5 ± 0.9 µm and 2.5 ± 1.0 µm respectively. A unimodal grain size distribution is obtained for pure KNNLST ceramics in Fig. 6.2g and its microstructure is similar to that with 1 mol% Bi in Fig. 6.2h. The average grain size for pure KNNLST composition is 2.8 ± 0.9 µm and 1.8 ± 0.6 µm for that with 1 mol% Bi.

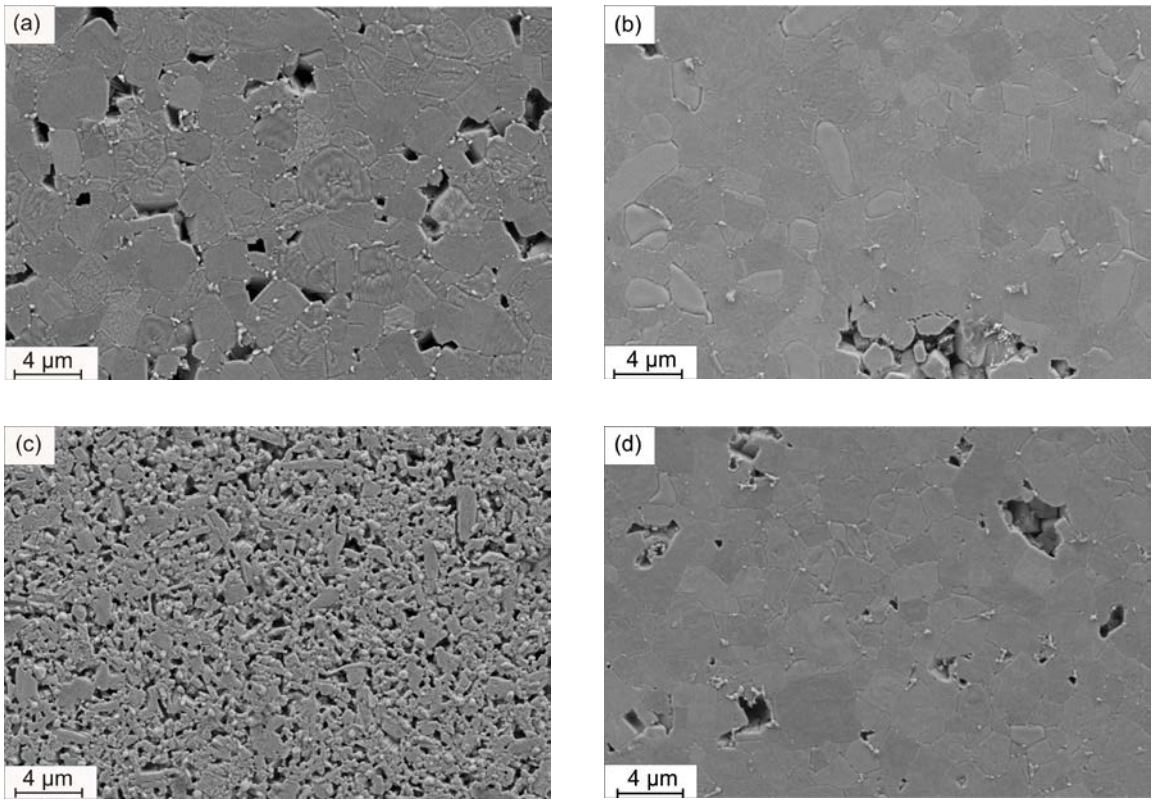

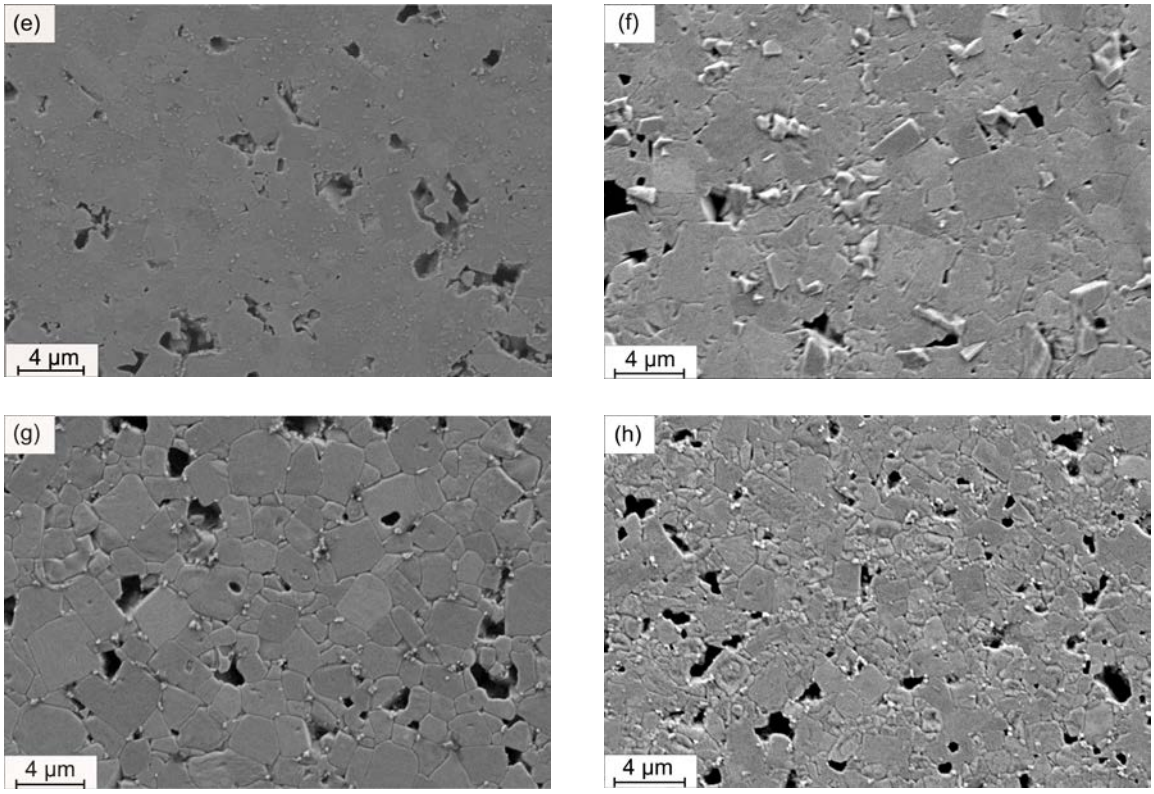

Fig. 6.2 SEM images of the polished surfaces of (a) pure KNN, (b) KNN-A with 1 mol% Bi (c) KNN-B with 1 mol% Bi, (d) pure KNNLT, (e) KNNLT-A with 1 mol% Bi, (f) KNNLT-B with 1 mol% Bi, (g) pure KNNLST, (h) KNNLST with 1.0 mol% Bi ceramics sintered at temperatures between 1090 °C and 1100 °C.

Fig. 6.3a shows the dielectric constant values for samples modified with Bi. For KNN-A compositions, the dielectric constant values did not vary much with doping and an average of 500 is obtained. The low dielectric constant value at 0.8 mol% is due to the low density value obtained for this composition. It has been reported for PZT ceramics that porosity has a very big influence on its dielectric properties [125]. The obtained values are slightly lower than reported values for similar compositions measured at the same frequency [126]. The dielectric constant values for KNN-B compositions between 0.2 mol% and 0.8 mol% are low probably due to the low density values of the samples. The dielectric constant values for KNNLT-A and KNNLT-B up to 0.6 mol% are similar (~ 600) and it increases to about 800 with more addition. The highest dielectric constant values are obtained with KNNLST compositions but there is no clear trend in the obtained values. The highest ε_r value (1265) is obtained with 1 mol% but it also has a high dielectric loss value. The corresponding dielectric loss (tan δ) values for the samples are shown in Fig. 6.3b. In most

compositions, the obtained dielectric loss values are below 0.05. Samples with 0, 0.5 and 1 mol% Bi content for KNNLT and KNNLST compositions showed relatively higher dielectric loss values due to their low density values. A dielectric loss value of ≤ 0.03 is obtained for most of the samples which is comparable to results from similar compositions [127].

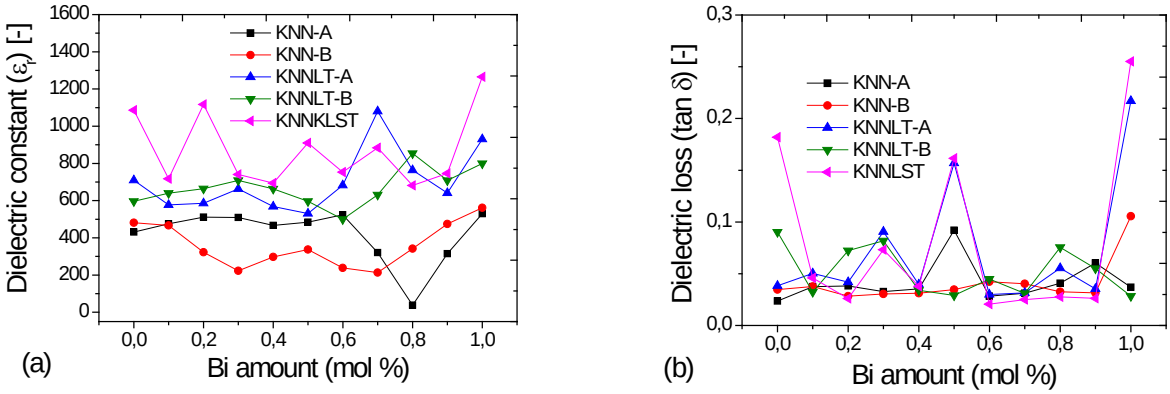

Fig. 6.3 Graph of (a) dielectric constant (ε_r) and (b) dielectric loss (tan δ) for KNN-based ceramics modified with Bi measured at 1 kHz and at room temperature.

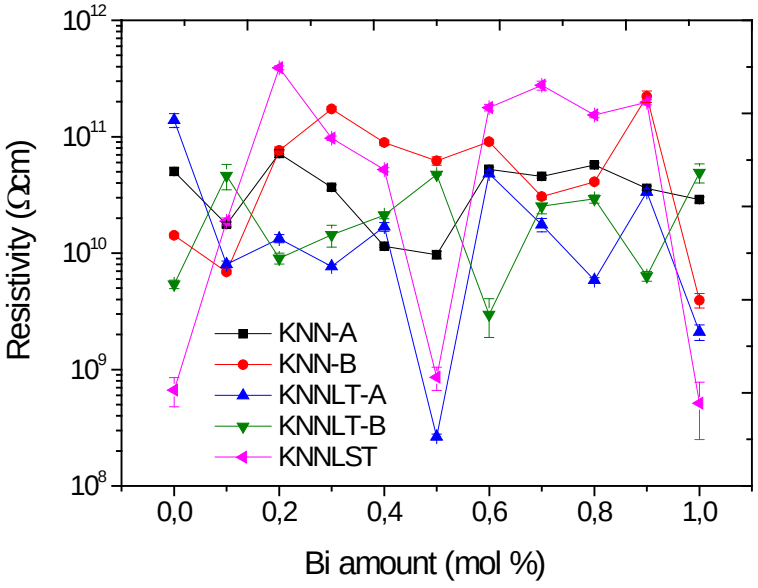

Fig. 6.4 Room temperature resistivity values for the KNN-based ceramics modified with Bi.

Fig. 6.4 shows the resistivity values for the samples. A correlation between dielectric loss values in Fig. 6.3b and resistivity values are observed. Compositions which have high values of dielectric loss also have low resistivity values. Resistivity values ranging from 10^9 to 10^{11} Ωcm are obtained for the samples and they are comparable to values reported by Saito et al for KNN ceramics doped with Li and Ta. [61].

The polarization hysteresis curve for KNNLT-B with 0.2 mol% Bi is shown in Fig. 6.5. With a 20 kV/cm electric field, a good hysteresis curve is obtained in this composition as well as in others. The P_r value for this composition is ~27 μC/cm^2 while the E_c is ~9.55 kV/cm. Table 6.3 shows the remanent polarization and coercive field values for other compositions. Some samples could not be measured due to large leakage current and for these compositions; no values of P_r and E_c are recorded. In most cases, with increasing addition of Bi, P_r decreases while E_c increases for KNN and KNNLT compositions but decreases for KNNLST compositions. P_r and E_c values for KNN modified with 0.5 wt% Bi were reported to be 28.2 μC/cm^2 and ~7.03 kV/cm respectively [126]. It was stated that with increasing Bi amount, the P_r increased while E_c decreased.

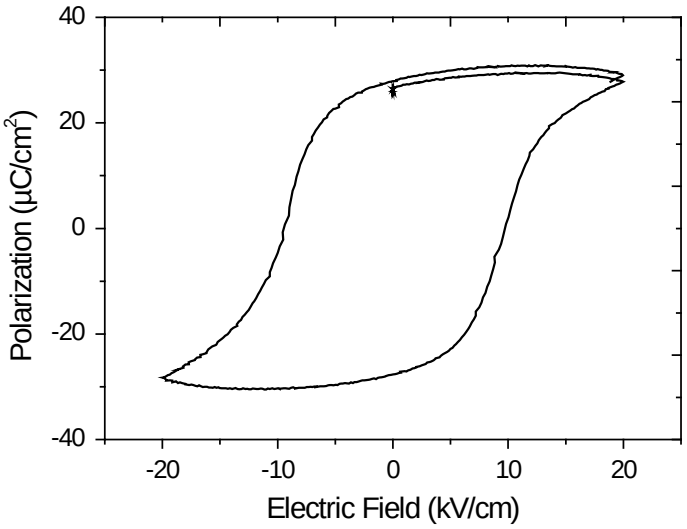

Fig. 6.5 Polarization hysteresis curve for KNNLT-B ceramics modified with 0.2 mol% Bi. Other compositions were measured and their remanent polarization and coercive field values are given in Table 6.3.

Table 6.3 Remanent polarization P_r and coercive field E_c values for KNN-based ceramics modified with Bi

Remanent Polarization (P_r) ($\mu C/cm^2$)						Coercive Field (E_c) (kV/cm)				
Bi amt [mol%]	KNN - A	KNN - B	KNNLT - A	KNNLT - B	KNNLST	KNN - A	KNN - B	KNNLT - A	KNNLT - B	KNNLST
0	25.5	25.5	23.5	23.5	26.69	9.77	9.77	8.86	8.86	12.87
0.1	23	26.84	22.27	16.97	22.63	9.04	11.2	11.3	9.28	8.53
0.2	37	11.89	11.33	27.34	5.02	10.35	12.5	11.6	9.55	8.13
0.3	32	--	27.5	31.73	10.89	9.5	--	10.3	8.52	8.9
0.4	--	--	13.5	37	10.21	--	--	11.5	11.95	8.5
0.5	33.69	--	--	15.21	--	9.5	--	--	10.95	--
0.6	33.35	--	8.68	--	8.8	10.05	--	10.2	--	9.43
0.7	--	--	--	11.54	--	--	--	--	12.34	--
0.8	--	--	23.8	15.08	5.09	--	--	12.5	11.04	8.3
0.9	--	--	--	17.19	3.81	--	--	--	12.19	8.75
1	20.25	--	--	7.09	--	10.86	--	--	10.5	--

Table 6.4 gives a summary of the obtained d^*_{33} values for the samples. Some of the samples were conductive and for such samples, no d^*_{33} values are recorded. Relatively high values (especially KNNLST compositions) are obtained for some compositions while low values are obtained for others. The d^*_{33} values and P_r values do not correspond in cases where there are high conductivity in the samples which contributed to the hysteresis.

Table 6.4 High signal piezoelectric charge coefficient (d^*_{33}) values for KNN-based ceramics modified with Bi

Piezoelectric charge coefficient (d^*_{33}) [pm/V]					
Bi amount [mol%]	KNN - A	KNN - B	KNNLT - A	KNNLT - B	KNNLST
0	209	209	227	221	301
0.1	227	135	282	259	429
0.2	250	97	247	144	--
0.3	162	68	237	88	359
0.4	--	92	159	332	--
0.5	278	378	388	264	250
0.6	198	65	228	93	315
0.7	137	87	89	347	283
0.8	123	139	304	406	237
0.9	--	205	409	205	265
1.0	280	373	236	191	--

6.1.4 Discussion

When Bi is incorporated to the A-site of the lattice, it is expected to act as a donor dopant

as shown in equation 6.1. Cation vacancies are created in the lattice which should result in improved values of dielectric constant and piezoelectric properties but high dielectric loss.

$$Bi_2O_3 \xrightarrow{6ABO_3} 2Bi_A^{\bullet\bullet} + 3O_O^{\times} + 4V_A^{'} \tag{6.1}$$

$$Bi_2O_3 \xrightarrow{4ABO_3} Bi_B^{''} + O_O^{\times} + 2V_O^{\bullet\bullet} \tag{6.2}$$

$$5Bi_2O_3 \xrightarrow{5ABO_3} 3Bi_A^{\bullet\bullet} + 5Bi_B^{''} + 12O_O^{\times} + 2V_A^{'} + 3V_O^{\bullet\bullet} \tag{6.3}$$

When it is incorporated to the B-site, it is expected to act as an acceptor dopant as shown using equation 6.2. Oxygen vacancies are created in the lattice which leads to smaller grain size, pinning of the domain wall movement and therefore lower values of dielectric and piezoelectric properties. It is also possible for Bi to be incorporated to both the A-and B-sites of the lattice as shown in equation 6.3. In this case, a combination of both donor and acceptor doped characteristics is expected.

The results are however different from the expected results from theoretical considerations. The temperature required to sinter the samples increased when Bi was used dope KNN because its presence possibly increased the activation energy required for sintering. Because there were many compositions to be sintered, samples with similar compositions were sintered using the same temperature. High density values were obtained for compositions where the sintering temperature was optimum while low values were obtained where the temperature was not optimum.

The diffraction patterns for KNN-A compositions show that the phases present are orthorhombic and the extra phase shows that Bi has a limited solid solubility on the A-site of KNN lattice. A similar result where an extra phase was observed has been reported by Du et al. [128]. An orthorhombic-orthorhombic phase boundary was observed between 0.4 and 0.5 mol% for KNN-B and may be due to differences in the oxygen octahedral tilting in the sample as the Bi amount increases. For KNNLT compositions, there is a phase boundary between an orthorhombic and a tetragonal phase with increasing amount of Bi. This indicates that the presence of Bi lowers the $T_{T\text{-}O}$ to near room temperature. The tetragonal phase in KNNLST ceramics transforms to a pseudocubic phase with increasing dopant amount which also indicates decreasing ferroelectricity in KNN ceramics.

The microstructures of the samples show that when Bi is in the sample, the average grain

size is slightly smaller except in KNN-B where it was much smaller and more porous. This could be due to the dopant accumulation at the grain boundary due to oxygen vacancies. The dielectric constant values for the samples increased with isovalent substitution of Li, Ta and Sb in this trend; from pure KNN compositions to KNNLT compositions and finally to KNNLST composition with little effect from Bi addition. This increase can be traced to the coexistence of both orthorhombic and tetragonal phases at room temperature. Low and high values of the dielectric loss were also obtained for the samples. Samples with high dielectric loss values can be traced to their low density.

The obtained resistivity values are in the range of 10^9 - 10^{11} Ωcm. The correlation between low resistivity and high dielectric loss values is because high conductivity causes easier flow of charges through the material which contributes to the overall loss in the samples. Soft and hard characteristics of KNN ferroelectrics were obtained from the polarization hysteresis measurements for the samples. The P_r values for KNNLT and KNNLST compositions decreased with increasing amount of Bi indicating hard effects. The E_c for KNNLT compositions slightly increased with Bi amount while that for KNNLST compositions decreased indicating both hard and soft effects respectively. The high leakage current in KNN compositions show that the samples are conductive due to defects in the lattice. Relatively high d^*_{33} values were obtained but there was no consistent trend with dopant addition probably due to differences in density values.

6.1.5 Summary

Bulk ferroelectric ceramics were produced using the HTE method and the effect of Bi on the properties of KNN was investigated. The addition of Bi increases the optimum sintering temperature. Orthorhombic, tetragonal and pseudocubic phases were observed depending on the composition and amount of Bi. The microstructure is greatly altered when Bi is added to the B-site of KNN lattice while the average grain size also decreased. High ε_r values and low tan δ values were obtained for most of the samples. Samples with high tan δ also had low resistivity. Polarization hysteresis curves were obtained for most of the samples with moderate d^*_{33} values. No consistent trend in the values possibly due to low density values in some samples.

7 Temperature dependent structure investigation

7.1 Structure of $(K_{0.37}Na_{0.52}Li_{0.03})(Nb_{0.87}Ta_{0.1}Sb_{0.03})O_3$ ceramics studied using synchrotron diffraction

7.1.1 Objective and experimental procedure

Very few studies have been reported on the structural characterization of modified KNN ceramics at elevated temperatures. In this research, the structure of KNN ceramics modified with Li, Ta and Sb was investigated because of its high piezoelectric properties [4]. The sample was ground to fine powder in preparation for synchrotron X-ray measurement. Quite often this mechanical treatment produces stresses and strains which are introduced to the sample and to release them, the powder was annealed.

The objective of this research is to determine quantitatively the relative amount of the phases present, their lattice parameters with temperature and the phase transition temperatures. The amount of the raw powders used for synthesis is shown in Table 5.1.

7.1.2 Results

The OES/ICP characterization technique was used to determine the actual amount of each element present and possible elements introduced as impurities during processing. Four separate measurements were made and the values were averaged to obtain the results shown in Table 7.1. The actual amount of some elements with lower melting temperature like Li, K and Sb were lower than the intended amounts possibly due to evaporation during the sintering process. The element with the highest deficiency is Sb. Elements like Na, Nb, Ta and O on the other hand had the same or slightly higher amounts than calculated before the synthesis. Since the starting powders are not 100 % pure, it is possible that some of these powders are contained in other raw powders as impurities. This result implies that there are vacancies on the A-site of the perovskite lattice. The final composition was

adjusted to reflect the changes in the amounts of elements present after the chemical analysis. The ceramic balls used for milling were made from ZrO_2 and the analysis showed that 0.91 g/kg of Zr was added to the sample. Finally, it was concluded that the actual composition of the ceramic is $(K_{0.37}Na_{0.52}Li_{0.03})(Nb_{0.87}Ta_{0.1}Sb_{0.03})O_3$.

Table 7.1 OES/ICP analysis data as well as calculated molar amounts of the elements in our composition

Element	Li	Na	K	Nb	Sb	Ta	O	Zr[1]
OES/ICP values [g/kg]	1.270(3)	67.90(14)	83.60(17)	463.0(9)	19.60(4)	109.0(2)	266.0(5)	0.91
Element amount [mol]	0.0317	0.515	0.372	0.867	0.028	0.105	3.0	0.0017
Expected amount [mol]	0.04	0.52	0.44	0.86	0.04	0.1	3.0	0

[1] This element was introduced into the powder during processing.

The observed and calculated diffraction profiles and their difference curves for $(K_{0.37}Na_{0.52}Li_{0.03})(Nb_{0.87}Ta_{0.1}Sb_{0.03})O_3$ at -213 °C, -53 °C, 20 °C, 200 °C and 360 °C respectively are shown in Fig. 7.1. Fig. 7.1c shows the profile at 20 °C where a two-phase model was used to refine the structure while Figs. 7.1d and 7.1e show the profiles where a single phase model (tetragonal and cubic phase respectively) was used. The enlarged insets in Fig. 7.1a–e indicate the higher 2-theta regions (35° to 55°) in the diffraction patterns.

The diffraction peaks for the patterns at lower temperatures (especially at T ~ 20 °C) show that they are significantly broadened. Microstructural analysis was done with the anisotropic peak broadening model from Stephens [95]. In the tetragonal phase especially, very high strains are reached in the polar direction for $00l_t$ reflections.

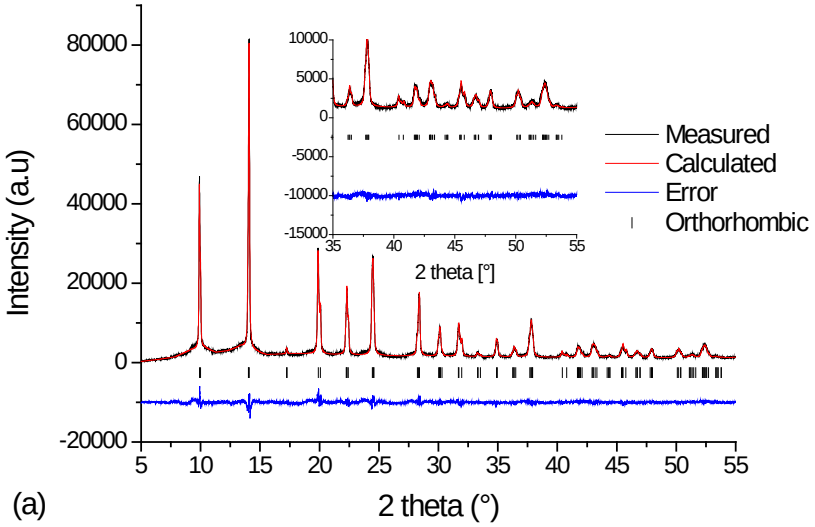
Intensity (a.u)
2 theta (°)
2 theta [°]
Measured
Calculated
Error
Orthorhombic
(a)

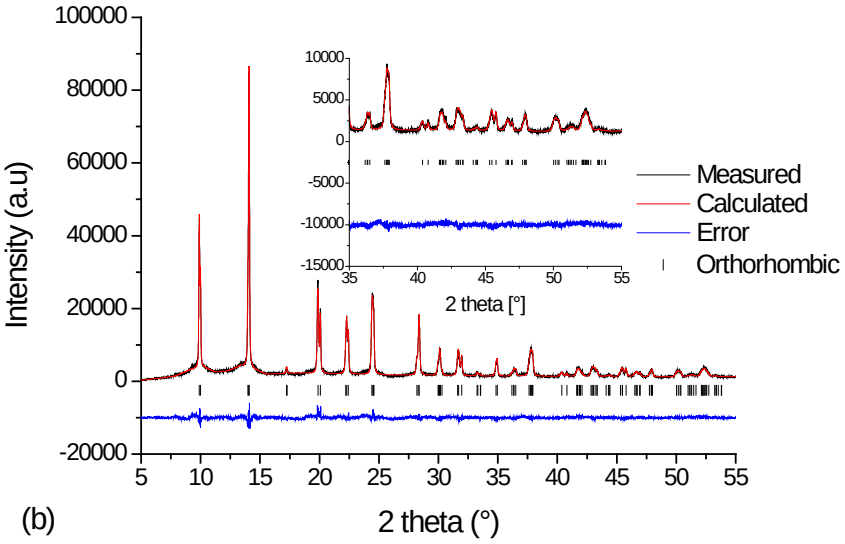
Intensity (a.u)
2 theta (°)
2 theta [°]
Measured
Calculated
Error
Orthorhombic
(b)

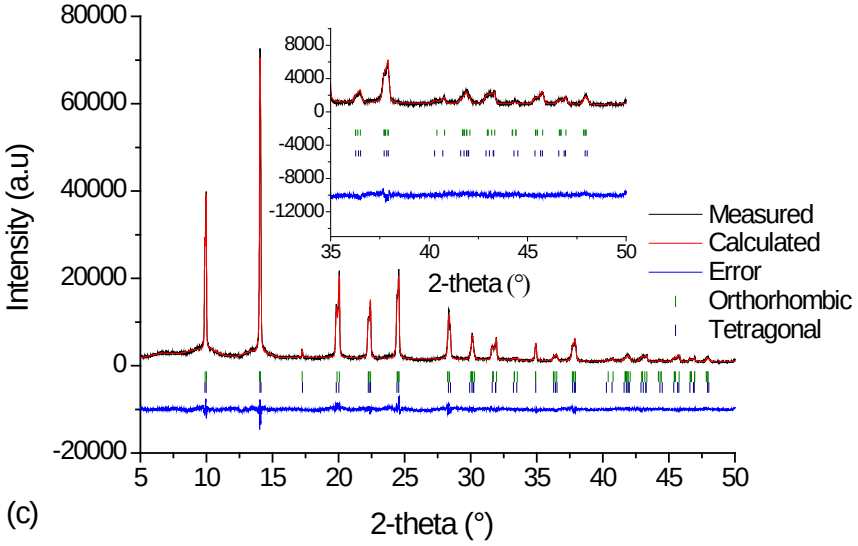
Intensity (a.u)
2-theta (°)
Measured
Calculated
Error
Orthorhombic
Tetragonal

(c)

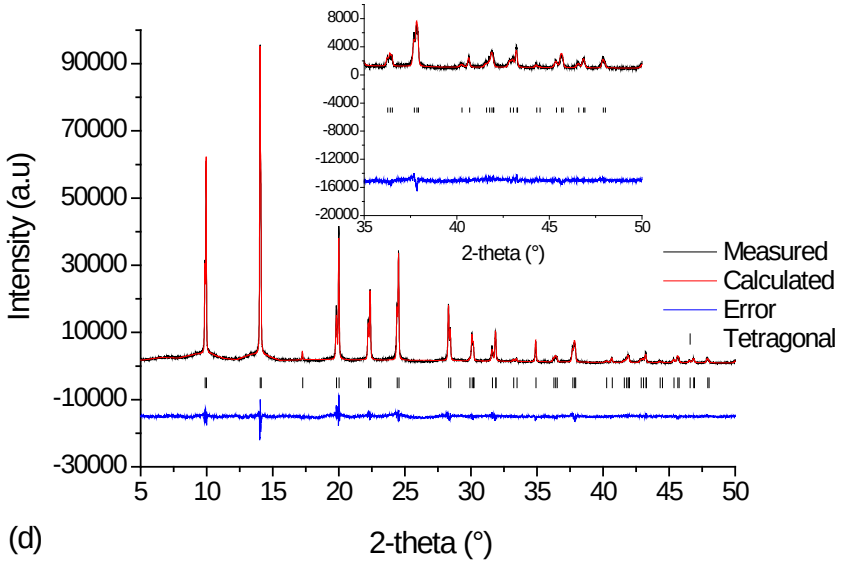
Intensity (a.u)
2-theta (°)
Measured
Calculated
Error
Tetragonal

(d)

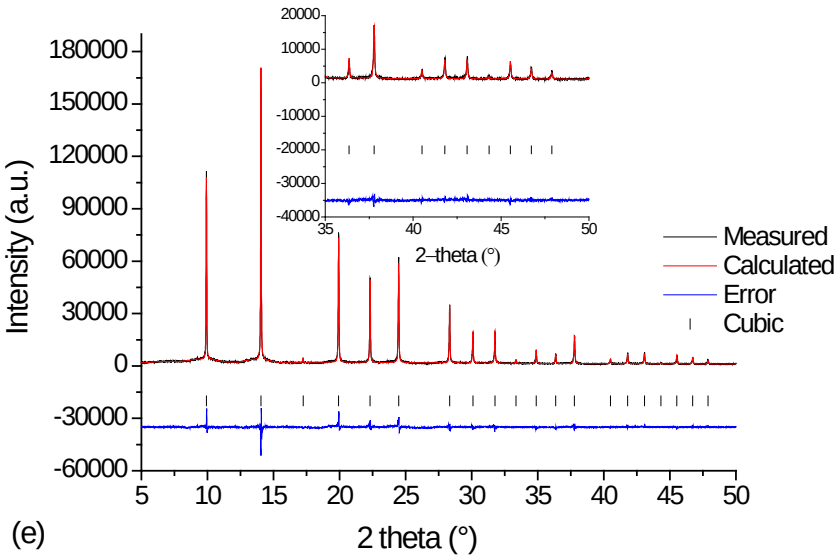

Fig. 7.1 Measured and calculated synchrotron diffraction profiles and their difference curves for $(K_{0.37}Na_{0.52}Li_{0.03})(Nb_{0.87}Ta_{0.1}Sb_{0.03})O_3$ at (a) -213 °C,(b) -53 °C (c) 20 °C, (d) 200 °C and (e) 360 °C respectively.

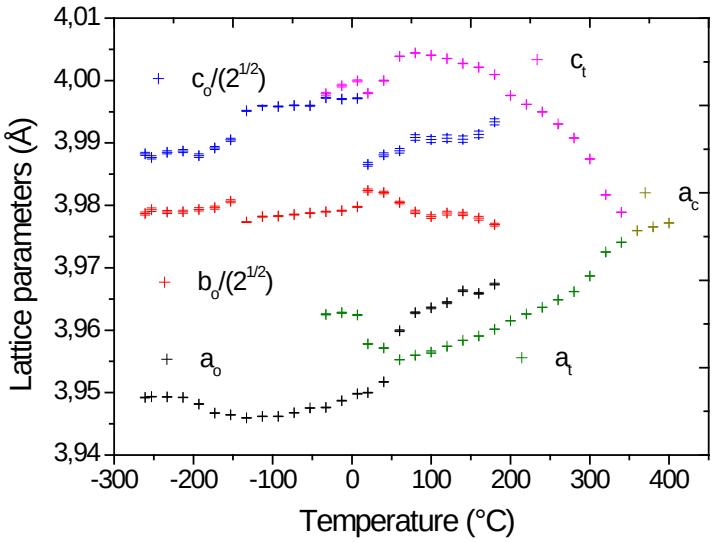

Fig. 7.2 Temperature dependence of lattice parameters a_o, b_o, c_o for the orthorhombic and a_t, c_t for the tetragonal and a_c for the cubic phase. There is a coexistence of orthorhombic and tetragonal phases between 20 °C and 180 °C, the tetragonal phase solely exists between 180 and 340 °C; the cubic phase exists above 340 °C.

The unit cell parameters as a function of temperature are shown in Fig. 7.2. The data were refined from -261 °C to -43 °C using an orthorhombic phase and from -33 °C up to 180 °C using a two-phase analysis approach because the refinement using one phase was not successful. The percentage of the constituent phases present was calculated through the scale factors involving the product of mass and volume of the unit cell contents of each phase. In this technique, the weight fraction of the phase was obtained using equation 7.1.

$$W_p = \frac{S_p(Z,M,V)_p * \tau_j}{\sum_j S_j(Z,M,V)_j * \tau_p} \tag{7.1}$$

where W_p is the relative weight fraction of phase p in a mixture of j phases while S, Z, M τ and V are the Rietveld scale factors derived from the refinement, the number of formula units per unit cell, mass of the formula unit, Brindley particle absorption contrast factor and the unit cell volume respectively.

Table 7.2 Experimental details and refinement results for $(K_{0.37}Na_{0.52}Li_{0.03})(Nb_{0.87}Ta_{0.1}Sb_{0.03})O_3$ for the lowest temperatures of each model

Phase type	Single	Two-phase		Single	Single
Crystal system, Space group	orthorhombic, *Amm2*	orthorhombic, *Amm2*	tetragonal, *P4mm*	tetragonal, *P4mm*	Cubic, $Pm\bar{3}m$.
Temp	-261 °C	20 °C		200 °C	360 °C
a (Å)	3.94921(5)	3.95000(7)	3.95779(6)	3.961364(19)	3.975964(16)
b (Å)	5.6267(2)	5.6320(2)	3.95779(6)	3.961364(19)	3.975964(16)
c (Å)	5.6403(2)	5.6379(3)	3.99799(12)	3.99797(3)	3.975964(16)
V (Å^3)	125.333(8)	125.422(9)	62.625(2)	62.7378(6)	62.8532(4)
Z	2	2	1	1	1
Refinement					
R_p (%)	6.54	6.5	--	8.02	7.31
R_{wp} (%)	8.48	8.37	--	6.77	6.7
R_{exp} (%)	3.33	3.88	--	3.6	3.35
G O F	4.7	4.2	--	5.1	5.8
X^2	21.9	18.13	--	26.26	31.97
No of parameters	32	47	47	47	24

The tetragonal *P4mm* (99) space group was used for the refinement from 200 °C to 340 °C while the cubic space group $Pm\bar{3}m$ (221) was used from 360 °C to 400 °C. The refinement results for the lowest temperature of each model are shown in Table 7.2. The orthorhombic cell parameters b_o and c_o were divided by √2 for better representation and they fit well with a_t and c_t from the tetragonal phase. The subscript't' denotes the

tetragonal cell. In the tetragonal phase, the *c/a*-ratio increased from -33 °C to 80 °C. Above this temperature, a constant decrease of the *c/a*-ratio could be observed up to the ferroelectric-paraelectric phase transition.

In the *Amm2* space group, the different values of b_o and c_o lead to a rhombic distortion of the $(001)_c$ plane resulting in an expansion along $[110]_c$. The pseudocubic lattice parameter a_{pc} was calculated using equation 7.2 while the pseudo-monoclinic angle β was derived from equation 7.3

$$a_{pc} = \frac{\sqrt{b_o^2 + c_o^2}}{2} \tag{7.2}$$

$$\beta = 2\arcsin\left(\frac{c_o}{2a_{pc}}\right) \tag{7.3}$$

The plot of the calculated pseudo-monoclinic angle as a function of temperature is shown in Fig. 7.3. As the values of b_o and c_o change (Fig. 7.2), the pseudo-monoclinic angle increases with temperature.

A plot of the dielectric constant together with the dielectric loss as a function of temperature is shown in Fig. 7.4. The dielectric constant indicates a maximum at a temperature of 335 ± 3 °C which corresponds to the temperature of the phase transition from the cubic to the tetragonal phase on cooling. The T_c obtained from the dielectric constant measurement is close to the result from the X-ray diffraction. Due to the diffuse nature of the plot near room temperature, it is not possible to determine the $T_{T\text{-}O}$ phase transition. The dielectric loss values increased with increasing measuring temperature and at the T_c, there was an abrupt decrease in the loss values.

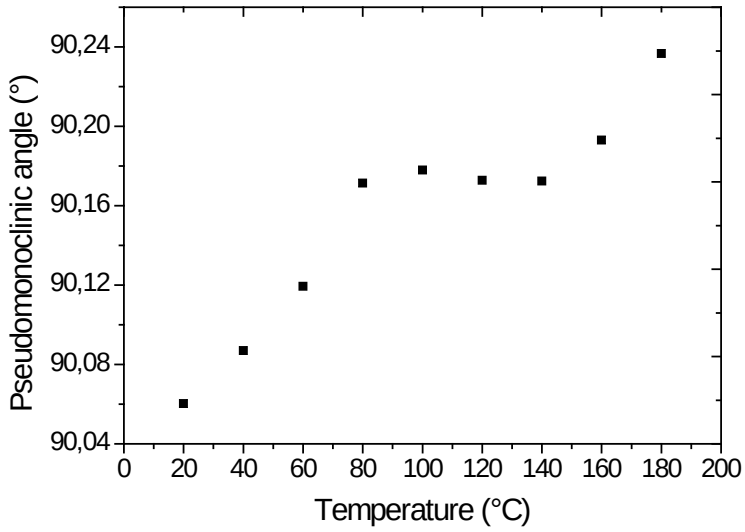

Fig. 7.3 Pseudo-monoclinic angle as a function of temperature for $(K_{0.37}Na_{0.52}Li_{0.03})(Nb_{0.87}Ta_{0.1}Sb_{0.03})O_3$ ceramics.

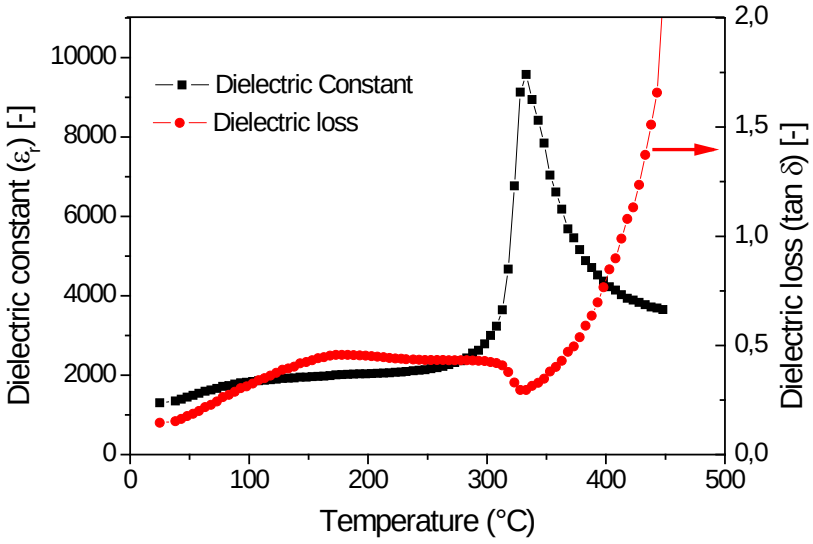

Fig. 7.4 Variation of the dielectric constant and dielectric loss as a function of temperature for $(K_{0.37}Na_{0.52}Li_{0.03})(Nb_{0.87}Ta_{0.1}Sb_{0.03})O_3$ ceramic measured at 1 kHz.

The unit-cell volume of the orthorhombic, tetragonal and cubic unit cells are shown in Fig. 7.5. As the temperature increases, the volume of the unit cell also increases except at the phase coexistence regions where there was a slight scatter in the values. This behavior can

be explained by the microstrains in the sample. At the phase coexistence region, the volume of the orthorhombic phase was slightly higher than the tetragonal phase.

Fig. 7.6 shows the weight fractions of the different phases as a function of temperature. From -33 °C to ~ 180 °C, both the tetragonal and orthorhombic phases coexist together but in different amounts. At lower temperatures, the orthorhombic phase is dominant and as the temperature increases, the volume fraction of the tetragonal phase gradually increases. The reason for this occurrence could be due to relaxation of the microstrains in the sample at near room temperature.

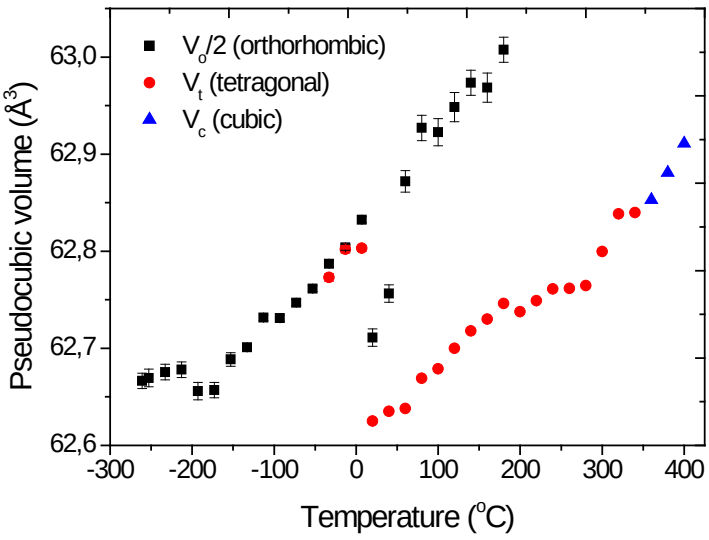

Fig. 7.5 Unit cell volume for the different phases in $(K_{0.37}Na_{0.52}Li_{0.03})(Nb_{0.87}Ta_{0.1}Sb_{0.03})O_3$ as a function of temperature.

The strain induces a phase transition to the high temperature phase which may be accompanied by the formation of domains. Above 180 °C, the weight fraction of the tetragonal phase is 100 % while above 340 °C; the weight fraction of the cubic phase is 100 %. The theoretical density for this composition at 20 °C was calculated using the mixture rule to be 4.845 g/cm^3. At room temperature the unit-cell parameters b_o and c_o are almost the same, while the unit-cell parameter a_o is shorter (Fig. 7.2). It should be noted that b_o is along the $[\bar{1}10]_c$-direction and c_o is along the $[110]_c$-direction. When b_o is equivalent to c_o, we have tetragonal symmetry with a polarization vector along $[110]_t$ which tells us that the structures are very closely related. From low temperatures up to 60 °C, a clear two-phase coexistence can be observed with a dominating orthorhombic

phase. In this temperature region, internal strain from the microstructure decreased with increasing temperature and led to a relaxation of both phases as seen from Fig. 7.2. From 80 °C to 140 °C a continuous phase transition from orthorhombic to tetragonal takes place. Above 140 °C an additional distortion of the orthorhombic phase can be observed (Fig. 7.3).

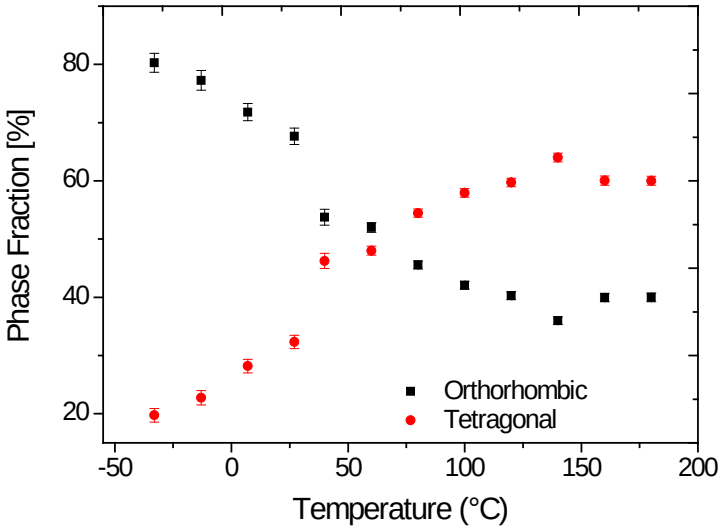

Fig. 7.6 Weight fractions of the phases in percent as a function of temperature for $(K_{0.37}Na_{0.52}Li_{0.03})(Nb_{0.87}Ta_{0.1}Sb_{0.03})O_3$ ceramics.

7.1.3 Discussion

The result from the OES/ICP analysis shows that the intended composition to be produced is different from the actual composition of the sample. The nature of the elements being synthesized determines the amount of materials lost during the sintering process. Elements with low melting temperature and high vapor pressure have a tendency to be deficient than those with high melting temperature. In this case, Li, K, and Sb were deficient while the other elements were almost unchanged.

The diffraction patterns in Fig. 7.1 show that very high intensities were obtained from the synchrotron X-ray measurements which make it easier to resolve the peaks in these patterns and subsequently do Rietveld refinement. The intensities of the reflections at higher angles are low compared to those at lower angles and superlattice reflections could not be observed. This is a disadvantage of X-ray diffraction compared to neutron

diffraction. The results from the microstructural analysis of the patterns show that there were anisotropic peak broadening especially at low temperatures. A possible explanation for the peak broadening could be that the microstrains which were introduced during sample processing were not completely removed during the annealing process. Very high strains are reached in the polar axis of the tetragonal phase which causes large deviations in the values of interplanar spacings along these axes. These broadenings are better observed with the diagram in Fig. 7.2 which shows the lattice parameters as a function of temperature where there is little scattering in the *c/a* ratios. At low temperatures (from ~-50 °C to 50 °C), the anisotropic broadening of the peaks can be interpreted in terms of compressive stresses which result in smaller tetragonal *c/a* ratios.

As the temperature is increased, the lattice relaxes, which may lead to the formation of larger-sized domains and as a result, a more consistent tetragonal *c/a* -ratio is obtained. If the sample contains domains with lamellar structure, this indicates that the polar axes are oriented along the width of these domains. This is best explained using the configuration in the 90° domains instead of 180° domains in $BaTiO_3$ [129] and in PZT ceramics [126]. The pseudo-monoclinic angle and the phase fraction show that above 140 °C, there is a continuous distortion in the progression of the weight percent of the phases with temperature. This unexpected behavior can either be due to strain from tetragonal domain growth or an artifact resulting from the residual anisotropic reflection broadening. This effect is well known for PZT and could be related to the nature of the microstructure [130].

The lattice parameters show that there is phase coexistence between an orthorhombic and a tetragonal phase which is an indication of a polymorphic phase boundary (PPT). As the temperature increases, the weight fraction of the tetragonal phase increases until above 180 °C where it becomes the only phase present. Different phases in a perovskite structured material have different polarization directions and domain configurations. When there is phase coexistence in the sample, it implies that the polarization directions possible in the material are the sum of the individual phases present. This phase coexistence over a wide range of temperature may explain why the piezoelectric properties of ceramics with this composition are better than those with other compositions.

7.1.4 Summary

Synchrotron X-ray diffraction measurements have been performed on $(K_{0.37}Na_{0.52}Li_{0.03})(Nb_{0.87}Ta_{0.1}Sb_{0.03})O_3$ ceramics up to 400 °C using a 20 °C measurement step. Chemical analysis carried out on the sample showed that small amounts of Zr were introduced during the processing and also that small amount of some volatile elements (Li, K and Sb) were lost after sintering. Rietveld refinement using Fullprof suite has been applied in this work to successfully refine the structure of this ceramic material.

An orthorhombic phase with space group *Amm2*, a tetragonal phase with space group *P4mm* and a cubic phase with space group $Pm\bar{3}m$ were used to refine the structure up to 400 °C. The quantitative analysis showed that while both the orthorhombic and tetragonal phase were present up to 180 °C, only the tetragonal phase remained up to 340 °C and above this temperature, the cubic phase was present. This phase coexistence in the sample explains in part why the piezoelectric properties of this material are higher than in other KNN ceramics.

7.2 Electrical and structural studies of $(K_xNa_{1-x})NbO_3$ ferroelectric ceramics modified with Li, Ta and Sb

7.2.1 Introduction

The effect of doping KNN with Li has been investigated by a lot of researchers. Guo et al. [131] studied the effect of Li from 4 to 20 mol% and reported an increase in the piezoelectric properties but also showed that above 8 mol%, an extra phase ($K_3Li_2Nb_5O_{15}$) begins to form. Temperature dependent dielectric studies [54, 132, 133] have been used to investigate the phase transitions when Li is added to KNN while thermal cycling [53] has been used to study the fatigue properties of KNN. A decrease in properties of about 30 % is observed after the first cycle and later the properties stabilize. Raman spectroscopy, dielectric and piezoelectric property measurements were used to develop a phase diagram for Li doped KNN ceramics and a rhombohedral phase was reported to be present at very low temperatures [54]. Rietveld refinement using a two-phase model with space groups *Amm2* and *P4mm* was used by Sun et al. [134] to refine the structure of this ceramic up to 6 mol% Li at room temperature.

When Sb was added to KNN above 10 mol%, a second phase related to $K_2NaSb_3O_9$ was observed while quantitative EDX analysis showed A-site element vacancies and excess

oxygen [135]. In another report, Zuo et al. reported that above 8 mol% Sb in KNN, the rhombohedral to orthorhombic phase transition temperature (T_{r-o}) is shifted upwards to room temperature [117].

Ta has been reported to lower both the electromechanical quality factor and the phase transition temperatures when added to KNN [135]. It also decreased the grain size of KNN ceramics due to high temperatures required for the sintering. There are reports about the doping of KNN with both Li and Ta [61, 114]. In one of the reports on KNN modified with 7 mol% $LiTaO_3$, *P1m1* space group was used as a reference material for the Rietveld refinement of the patterns. Temperature dependent lattice parameter values were plotted although a second phase could be observed in the diffraction pattern used for the refinement [136]. The piezoelectric and electromechanical properties of the samples were reported to have increased while their phase transition temperatures decreased.

There is very little information in the literature about the structural studies of KNN-based ceramics at both cryogenic and elevated temperatures. Synchrotron diffraction is a very important tool for studying X-ray diffraction of crystalline substances and in this investigation, KNN modified separately with Li, Ta, Sb and a combination of Li and Ta was synthesized and analyzed from -261 °C to temperatures above their respective T_c. Dielectric and hysteresis measurements were also carried out on the samples.

Sample preparation steps are expected to introduce stresses and strain in the samples and also changes in the lattice from the highly symmetric cubic phase to low symmetry also distort the lattice. The samples were annealed prior to the measurement but all the stresses and strains may not have been relieved thereby contributing to the lattice distortion.
The distortions of the lattice for the rhombohedral, orthorhombic and tetragonal lattices were calculated using equations (7.4) - (7.6) respectively.

$$\eta(r) = \left(\left(\frac{c_h}{(\sqrt{6} * a_h)} \right) - 1 \right) * 100 \tag{7.4}$$

$$\eta(o) = \left(\left(\frac{c_o}{\sqrt{2} * a_o} \right) - 1 \right) * 100 \tag{7.5}$$

$$\eta(t) = \left(\left(\frac{c_t}{a_t} \right) - 1 \right) * 100 \tag{7.6}$$

The objective here is to determine the relative amount of phases present, their lattice parameters, and the phase transition temperatures of these ceramics as a function of temperature and to compare these results with those from electrical characterization. The composition and amount of each component powder used for the synthesis is shown in Table 7.3 while that for $(K_{0.5}Na_{0.5})(Nb_{0.96}Sb_{0.04})O_3$ has been given in Table 5.3

Table 7.3 Composition and amount of each component powder used for the synthesis

	Amount of the powders (grams)					
Composition	K_2CO_3	Na_2CO_3	Li_2CO_3	Nb_2O_5	Ta_2O_5	Total
$(K_{0.48}Na_{0.48}Li_{0.04})NbO_3$	20,6232	15,8181	0,9189	82,6401	0	120
$(K_{0.5}Na_{0.5})(Nb_{0.9}Ta_{0.1})O_3$	20,4474	15,6831	0	70,7916	13,0761	120
$(K_{0.48}Na_{0.48}Li_{0.04})(Nb_{0.9}Ta_{0.1})O_3$	19,7232	15,1278	0,8787	71,1312	13,1877	120

7.2.2 OES/ICP analysis

Table 7.4 shows the results from the OES/ICP analysis and the calculated molar amounts of the elements.

Table 7.4 OES/ICP analysis as well as calculated molar amounts of the elements in the samples.

Element	Li	Na	K	Nb	Sb	Ta	O	Zr*
$(K_{0.48}Na_{0.48}Li_{0.04})NbO_3$								
OES/ICP values [g/kg]	1.27	68.9	108	526	--	--	281	0.40
Element amount [mol]	0.03136	0.51369	0.47346	0.97041	--	--	3.01034	<0.00075
$(K_{0.5}Na_{0.5})(Nb_{0.90}Ta_{0.1})O_3$								
OES/ICP values [g/kg]	--	64.5	105	452	--	98.2	266	0.40
Element amount [mol]	--	0.50957	0.48777	0.88364	--	0.09857	3.01966	<0.00080
$(K_{0.5}Na_{0.5})(Nb_{0.94}Sb_{0.06})O_3$								
OES/ICP values [g/kg]	--	72.5	107.0	491	35.4	--	276	0.4
Element amount [mol]	--	0.54900	0.47643	0.92004	0.05061	--	3.00315	0.00076
$(K_{0.48}Na_{0.48}Li_{0.04})$ $(Nb_{0.9}Ta_{0.1})O_3$								
OES/ICP values [g/kg]	0.96	64.6	101	451	--	101	267	0.40
Element amount [mol]	0.02502	0.5083	0.46736	0.87825	--	0.10098	3.01922	<0.00079

* This element was introduced into the powder during processing.

There are deficiencies in Li, K, Sb and Nb while Na, Ta and O are in the required amounts. Based on the results, the actual compositions are; $(K_{0.47}Na_{0.51}Li_{0.03})NbO_{3.01}$ abbreviated

here as KNN-L, $(K_{0.49}Na_{0.51})(Nb_{0.88}Ta_{0.1})O_3$ as KNN-T, $(K_{0.48}Na_{0.55})(Nb_{0.92}Sb_{0.05})O_3$ as KNN-S and $(K_{0.47}Na_{0.51}Li_{0.025})(Nb_{0.88}Ta_{0.1})O_{3.02}$ as KNN-LT.

7.2.3 Structural characterization

The measured and calculated diffraction profiles and their difference curves for KNN-L, KNN-T, KNN-LT and KNN-S ceramics measured at -253 °C showing the orthorhombic and rhombohedral phases are shown in Fig. 7.7. KNN-L and KNN-LT (Fig. 7.7a and 7.7c) show an orthorhombic *Amm2* phase while KNN-T and KNN-S (Fig. 7.7b and 7.7d) show a rhombohedral *R3c* phase. The insets in the figures are enlarged sections of the patterns with higher 2-theta regions (35° - 55°). The peak splitting of 200_c reflection at ~20° (Fig. 7.7a and 7.7c) shows that the phase present is orthorhombic while for the rhombohedral phase, (Fig. 7.7b and 7.7d) the 200_c reflection shows no splitting. The diffraction pattern for $(K_{0.37}Na_{0.52}Li_{0.03})(Nb_{0.87}Ta_{0.1}Sb_{0.03})O_3$ ceramics also has an orthorhombic phase at -261 °C. This indicates that the presence of Li in KNN ceramics suppresses the orthorhombic to rhombohedral phase transition.

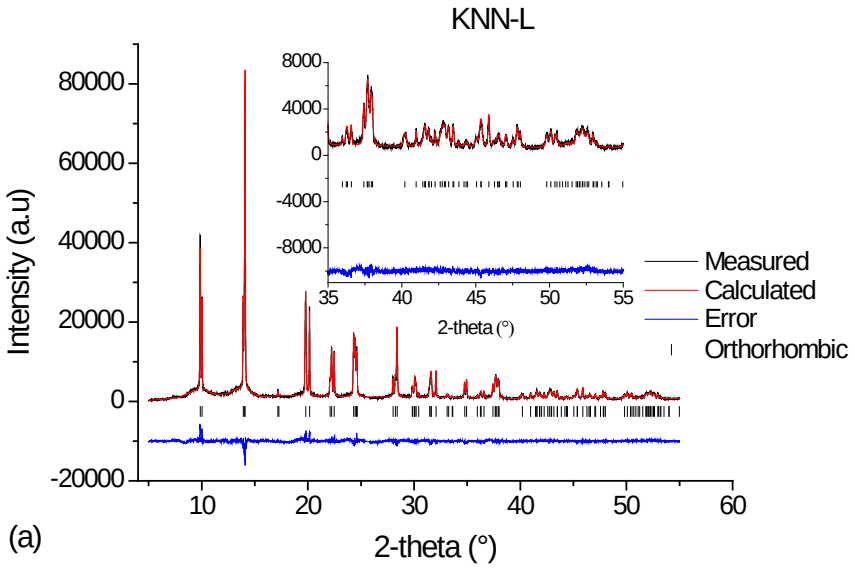

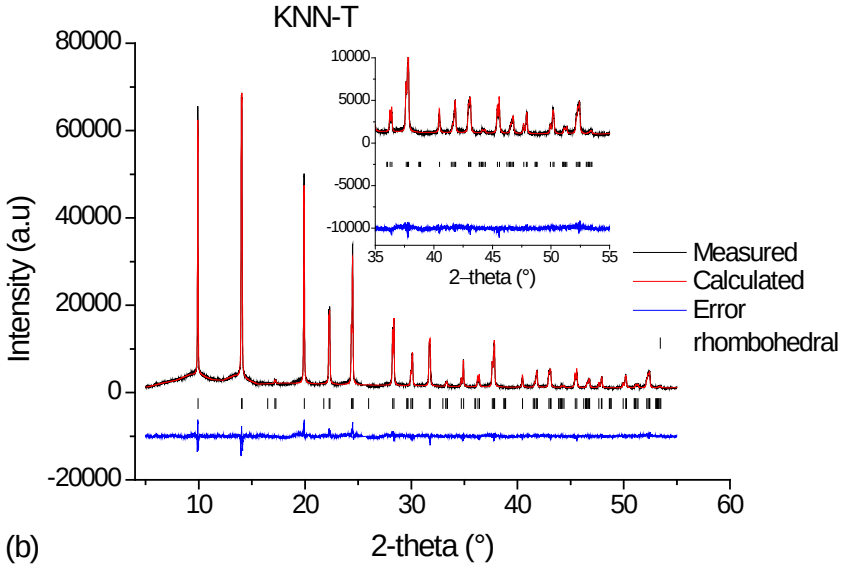
KNN-T
Intensity (a.u)
2-theta (°)
2–theta (°)
Measured
Calculated
Error
rhombohedral

(b)

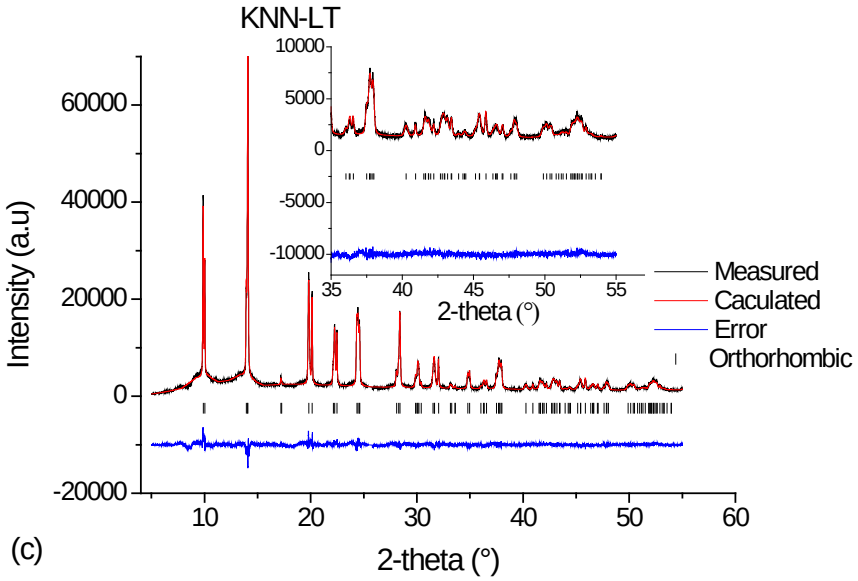
KNN-LT
Intensity (a.u)
2-theta (°)
2-theta (°)
Measured
Caculated
Error
Orthorhombic

(c)

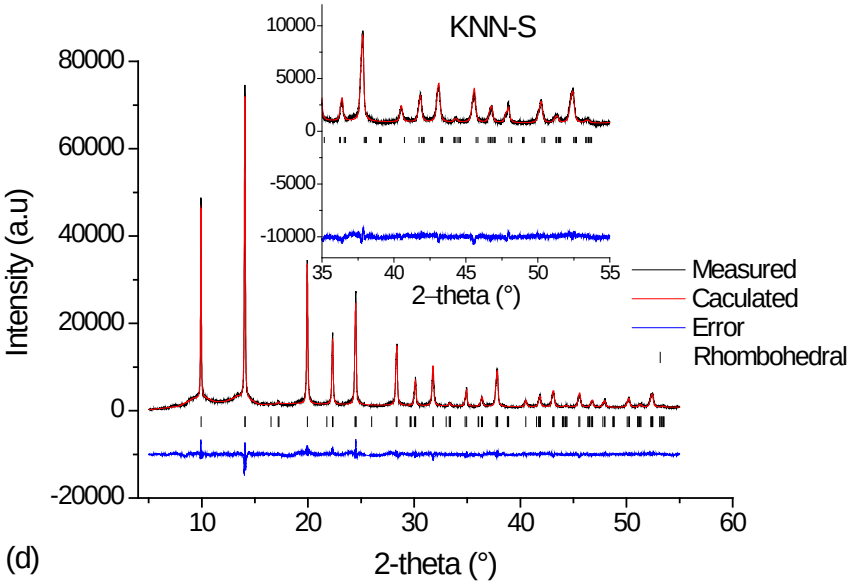

Fig. 7.7 Measured and calculated synchrotron X-ray diffraction profiles and their difference curves for (a) KNN-L measured at -253 °C, (b) KNN-T measured at -253 °C showing the rhombohedral phase and (c) KNN-LT measured at -253 °C showing the orthorhombic phase (d) KNN-S measured at -253 °C showing the rhombohedral phase.

Table 7.5 Experimental details and refinement result for KNN-L for the lowest temperatures of each model

Phase type	Single	Two-phase		Single	Single
Crystal system space group Temp	Orthorhombic *Amm2* -261 °C	Orthorhombic *Amm*2 100 °C	Tetragonal *P4mm* 100 °C	Tetragonal *P4mm* 120 °C	Cubic $Pm\bar{3}m$ 480 °C
a (Å)	3.93132(3)	3.94646(4)	3.95257(8)	3.95531(3)	3.97596(16)
b (Å)	5.63895(5)	5.64422(7)	3.95257(8)	3.95531(3)	3.97596(16)
c (Å)	5.68307(5)	5.67812(7)	4.03856(15)	4.03898(4)	3.97596(16)
V (Å^3)	125.9851(17)	126.478(3)	63.094(3)	63.1878(10)	62.8532(4)
ρ (g/cm^3)	4.451	4.436		4.438	4.424
Z	2	2	1	1	1
Refinement					
Rp (%)	7.19	10.1	--	12.5	11.7
Rwp (%)	9.25	12.7	--	16.8	14.7
Rexp (%)	2.04	2.28	--	2.31	2.36
G O F	4.5	5.5	--	7.1	6.2
X^2	20.6	30.8	--	53.2	38.9
No of parameters	35	43	43	30	24

The refinement parameters for lowest temperatures of each model used in the refinement for KNN-L, KNN-T, KNN-LT and KNN-S ceramics are shown in Tables 7.5 - 7.8 respectively. Depending on the composition and temperature at which the pattern was taken, either a single or a mixed phase was used.

Table 7.6 Experimental details and refinement result for KNN-T for the lowest temperatures of each model

Phase type	Single	Two-phase		Single	Single	Single
Crystal system space group Temp	Rhombohedral *R3c* -261 °C	Rhombohedral *R3c* -103 °C	Othorhombic *Amm*2 -103 °C	Orthorhombic *Amm*2 -83 °C	Tetragonal *P4mm* 170 °C	Cubic $Pm\bar{3}m$ 370 °C
a (Å)	5.61271(4)	5.61662(5)	3.94036(6)	3.94128(2)	3.96331(2)	3.98276(19)
b (Å)	5.61271(4)	5.61662(5)	5.63778(12)	5.63739(4)	3.96331(2)	3.98276(19)
c (Å)	13.83390(4)	13.83255	5.67068(10)	5.67081(4)	4.02016(3)	3.98276(19)
V (Å^3)	377.417(4)	377.905(5)	125.974(4)	125.9970(14)	63.1479(6)	63.1758(5)
ρ (g/cm^3)	4.726	4.720		4.719	4.709	4.704
Z	6	6	2	2	1	1
Refinement						
Rp (%)	6.38	6.50	--	6.34	8.33	9.22
Rwp (%)	8.38	8.56	--	8.23	10.6	12.1
Rexp (%)	1.91	3.76	--	1.89	2.14	2.20
G O F	4.4	4.5	--	4.4	7.1	5.5
X^2	19.2	20.66	--	19.0	24.6	30.2
No of parameters	27	35	35	35	30	20

Table 7.7 Experimental details and refinement result for KNN-LT for the lowest temperatures of each model

Phase type	Single	Two-phase		Single	Single
Crystal system space group Temp	Orthorhombic *Amm2* -261 °C	Orthorhombic *Amm*2 20 °C	Tetragonal *P4mm* 20 °C	Tetragonal *P4mm* 110 °C	Cubic $Pm\bar{3}m$ 420 °C
a (Å)	3.93602(3)	3.94594(5)	3.95505(12)	3.95496(2)	3.96519(2)
b (Å)	5.63331(6)	5.6418(2)	3.95505(12)	3.95496(2)	3.96519(2)
c (Å)	5.67188(6)	5.66929(11)	4.0038(5)	4.02479(3)	3.96519(2)
V (Å^3)	125.761(2)	126.212(5)	62.629(8)	62.9544(7)	63.1240(7)
ρ (g/cm^3)	4.709	4.701	--	4.703	4.693
Z	2	2	1	1	1
Refinement					
Rp (%)	6.26	4.50	--	6.08	6.17
Rwp (%)	8.06	5.70	--	8.05	7.85
Rexp (%)	1.81	1.51	--	1.21	1.75
G O F	4.4	3.8	--	6.6	4.5
X^2	19.7	14.3	--	44.1	20.2
No of parameters	35	46	46	30	30

Table 7.8 Experimental details and refinement result for KNN-S for the lowest temperatures of each model.

Phase type	Single	Two-phase		Single	Single	Single
Crystal system space group Temp	Rhombohedral *R3c* -261 °C	Rhombohedral *R3c* -83 °C	Othorhombic *Amm*2 -83 °	Othorhombic *Amm*2 -73 °C	Tetragonal *P4mm* 160 °C	Cubic $Pm\bar{3}m$ 340 °C
a (Å)	5.61129(8)	5.61435(11)	3.95842(14)	3.96256(7)	3.96648(4)	3.98067(2)
b (Å)	5.61129(8)	5.61435(11)	5.6281(2)	5.62165(10)	3.96648(4)	3.98067(2)
c (Å)	13.80226(17)	13.80779(3)	5.6430(2)	5.64242(9)	4.00373(5)	3.98067(2)
V ($Å^3$)	376.363(8)	376.924(14)	125.719(8)	125.691(4)	62.9906(12)	63.0767(6)
ρ (g/cm^3)	4.606	4.597		4.597	4.587	4.582
Z	6	6	2	2	1	1
Refinement						
Rp (%)	7.59	7.64	--	7.48	9.8	
Rwp (%)	10	9.9	--	9.75	12.9	8.37
Rexp (%)	2.1	2.08	--	2.09	2.03	10.8
G O F	4.8	4.7	--	4.7	6.4	2.01
X^2	22.8	22.6	--	21.8	40.4	28.9
No of parameters	27	36	36	31	30	21

The lattice parameters for KNN-L, KNN-T, KNN-LT and KNN-S ceramics as a function of temperature are shown in Fig. 7.8. Depending on the composition, a series of phase transformations were observed from -261 °C to temperatures above the respective T_c of the samples. Orthorhombic, rhombohedral, tetragonal and cubic phases were observed and for these phases, the space groups *Amm2*, *R3c*, *P4mm* and $Pm\bar{3}m$ respectively were used for the refinement. There are temperature ranges where phase coexistence occurred and for such phase mixtures, a combination of the respective models was used for the refinement. The rhombohedral cell parameters a_h and c_h were divided by √2 and √12 respectively for better representation.

KNN-L in Fig. 7.8a exhibits an orthorhombic phase from -261 °C to 90 °C. Between 100 °C and 110 °C; phase coexistence between the orthorhombic phase and the tetragonal could be observed. The tetragonal phase existed from 120 °C to 470 °C and above this temperature the cubic phase was present. In KNN-T (Fig. 7.8b), the rhombohedral phase was observed from -261 °C to -93 °C with a two-phase coexistence of the rhombohedral and the orthorhombic phase between -103 °C and -93 °C. From -103 °C to 150 °C, the orthorhombic phase was present showing a two-phase coexistence of the orthorhombic and the tetragonal phase at 160 °C. From 160 °C to 360 °C, the tetragonal phase was observed

and above 370 °C, the sample was cubic. In KNN-LT (Fig. 7.8c), the orthorhombic phase was present from -261 °C to 100 °C with a broad two-phase coexistence of the orthorhombic and the tetragonal phase between -23 °C to 100 °C. The tetragonal phase was present from -23 °C to 420 °C and above this temperature, the cubic phase was present.

In KNN-S (Fig. 7.8d), the rhombohedral phase was present from -261 °C to -83 °C with a two-phase coexistence between the rhombohedral and the orthorhombic phase at -83 °C. From -83 °C to 140 °C, the orthorhombic phase was present and at 140 °C, a two-phase coexistence between the orthorhombic and the tetragonal phase was observed. The tetragonal phase was present from 140 °C to 320 °C and above 340 °C, the sample was purely cubic.

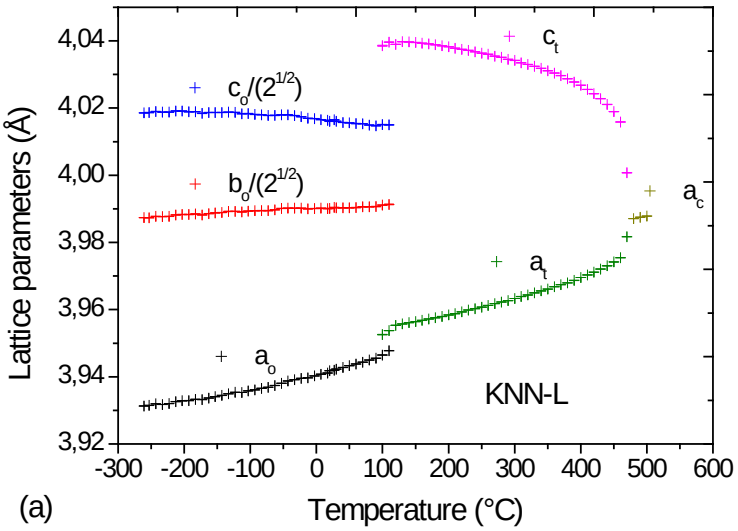

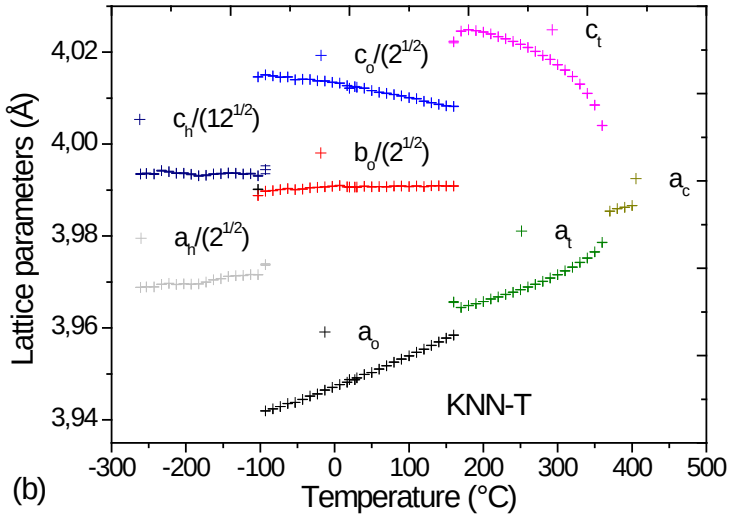
Lattice parameters (Å)
4,02
4,00
3,98
3,96
3,94
-300
-200
-100
0
100
200
300
400
500
Temperature (°C)
$c_o/(2^{1/2})$
c_t
$c_h/(12^{1/2})$
$b_o/(2^{1/2})$
a_c
$a_h/(2^{1/2})$
a_t
a_o
KNN-T

(b)

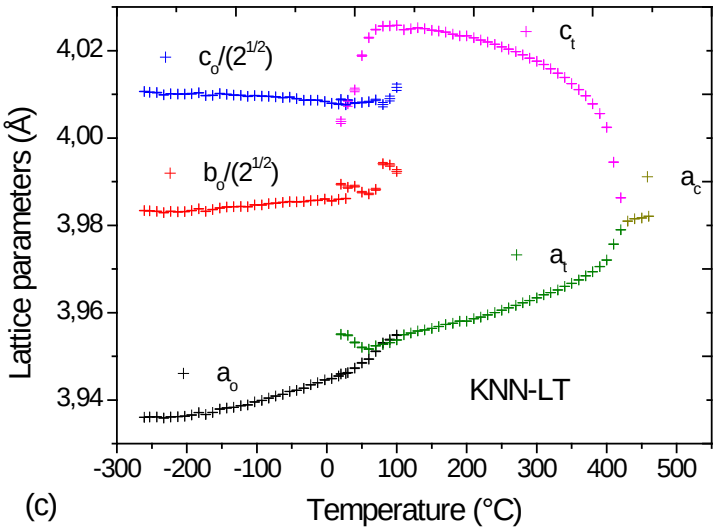
Lattice parameters (Å)
4,02
4,00
3,98
3,96
3,94
-300
-200
-100
0
100
200
300
400
500
Temperature (°C)
$c_o/(2^{1/2})$
c_t
$b_o/(2^{1/2})$
a_c
a_t
a_o
KNN-LT

(c)

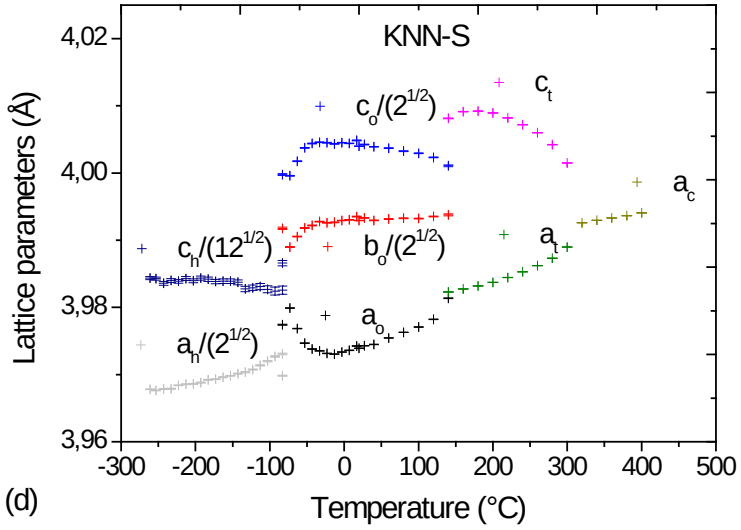

Fig. 7.8 Temperature dependence of the lattice parameters (Å) a_h, c_h for the rhombohedral phase, a_o, b_o, c_o for the orthorhombic phase, a_t, c_t for the tetragonal phase and a_c for the cubic phase. (a) KNN-L ceramics with coexistence of the orthorhombic and tetragonal phase between 100 °C and 110 °C (b) KNN-T ceramics with phase coexistence between the rhombohedral and orthorhombic phase between -103 °C and -93 °C and orthorhombic and tetragonal phases at 160 °C (c) KNN-LT ceramics with coexistence of the orthorhombic and tetragonal phases from -40 °C to 100 °C (d) KNN-S ceramics with phase coexistence between the rhombohedral and orthorhombic phase at -83 °C and orthorhombic and tetragonal phases at 140 °C.

The pseudo-cubic lattice parameter a_{pc} was calculated using equation 7.2 while the pseudo-monoclinic angle β was derived from equation 7.3. The plots of the pseudo monoclinic angle as a function of temperature for the samples are shown in Fig. 7.9. In all cases, the pseudo-monoclinic angle decreases with increasing temperature for each phase. The pseudo-monoclinic angle increased in the following order; KNN-S, KNN-T, KNN-LT and KNN-L which shows that such lattice deformations do not require monoclinic symmetry. The deviation in the β-values obtained for the KNN-LT composition from ~7 °C corresponds to the two-phase coexistence between the orthorhombic and the tetragonal phase. The β-values could only be calculated from ~ -100 °C for samples with a rhombohedral phase (KNN-S and KNN-T). The β-values for the KNN-S composition for ≥

20 °C are almost exactly 90° which shows that they are very close to tetragonal values of the lattice parameters.

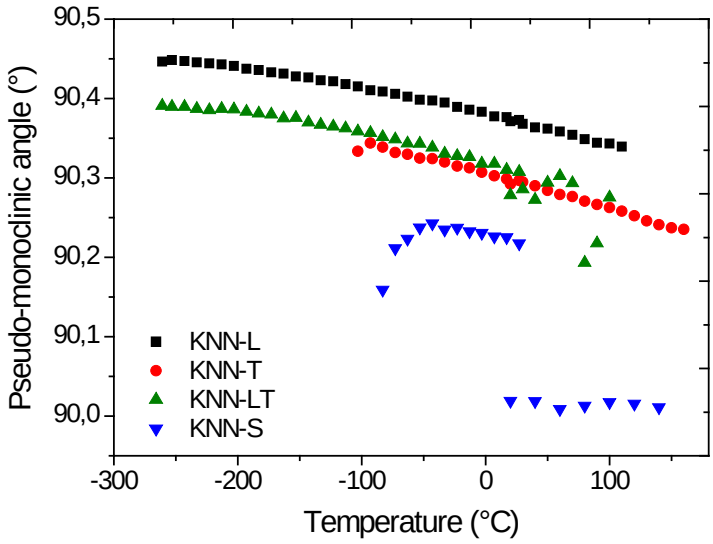

Fig. 7.9 Variation of the pseudo-monoclinic angle as a function of temperature for KNN-L, KNN-T, KNN-S and KNN-LT ceramics.

The percentage of the constituent phases in the samples was calculated through the scale factors which involve the product of mass and volume of the unit cell contents of each phase. The weight fraction of the phases (W_p) was obtained using equation 7.1 The weight fractions of the phases for the samples as a function of temperature are shown in Fig. 7.7. In KNN-L (Fig. 7.7a), the rhombohedral phase was not observed at low temperatures and the phase coexistence between the orthorhombic and the tetragonal phase occurred within a narrow temperature range between 100 °C and 110 °C. The temperature range of phase coexistence in KNN-LT (Fig. 7.7b) was wider compared to the other compositions. The coexistence ranges from -33 °C to 110 °C and as the temperature increases, the percentage of the tetragonal phase increases. The temperature range of phase coexistence is even wider (up to 180 °C) when Sb is added to the sample [137]. In KNN-T (Fig. 7.7c), two different phase coexistence regions are observed. The first is between a rhombohedral and an orthorhombic phase while the second is between an orthorhombic and a tetragonal phase. The first occurs between -103 °C and -93 °C while the second is at 160 °C. The phase coexistence in KNN-S (Fig. 7.70d) is similar to KNN-T but the difference is in the

coexistence temperature. The first coexistence occurs at -83 °C while the second is at 120 °C.

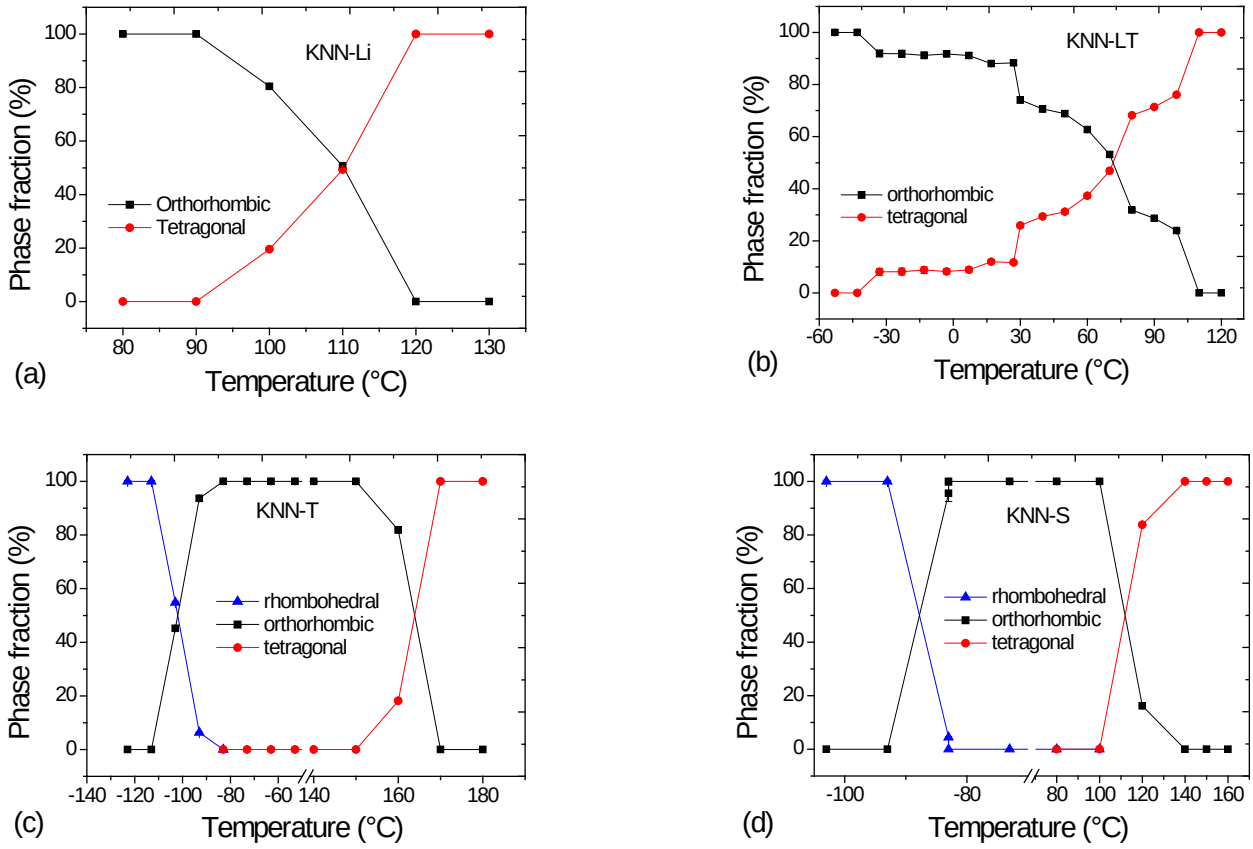

Fig. 7.7 Weight fraction of the phases (%) as a function of temperature for (a) KNN-L ceramics (b) KNN-LT ceramics (c) KNN-T ceramics and (d) KNN-S ceramics.

The rhombohedral phase was observed in KNN-T composition from -261 °C to -93 °C and from -261 °C to -83 °C for KNN-S composition. To calculate the rhombohedral angle α_{pc} in the pseudocubic cell, the lattice parameters (a_h and c_h) of the hexagonal cell were used as shown in equation 7.7.

$$\cos\alpha_{pc} = \frac{\left(c_h^2 - 6a_h^2\right)}{\left(c_h^2 + 12a_h^2\right)} \tag{7.7}$$

The lattice strain is the deviation of the rhombohedral angle from 90° and is shown in Fig. 7.8. As the temperature increases, the lattice strain gradually decreases and approaches

zero when a new phase is formed. Similar compositions with similar results have been reported [138, 139].

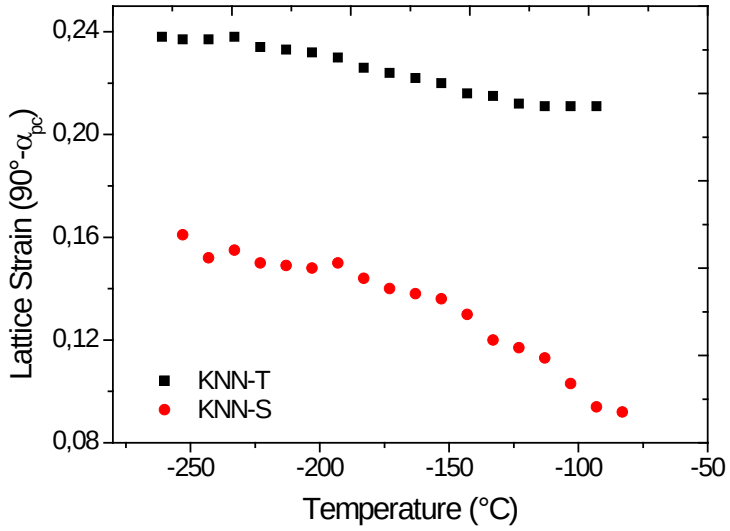

Fig. 7.8 Lattice strain for KNN-T and KNN-S ceramics.

The lattice distortion (%) as a function of temperature in the samples is shown in Fig. 7.9. The largest lattice distortions for both the orthorhombic and tetragonal phase are with the KNN-L composition. In the orthorhombic phase, the distortion is ~ 2.25% and as the temperature increases, the distortion decreases. When a new phase is formed, the distortion jumps to a higher value and then gradually decreases with increasing temperature. As the temperature approaches T_c, the distortion rapidly drops to almost zero. The same trend was observed for the KNN-LT composition with the difference that the distortions are lower. The deviation in the distortion values corresponds to the two-phase coexistence in the sample. For KNN-S and KNN-T composition, the degree of distortion in the rhombohedral phase is the smallest.

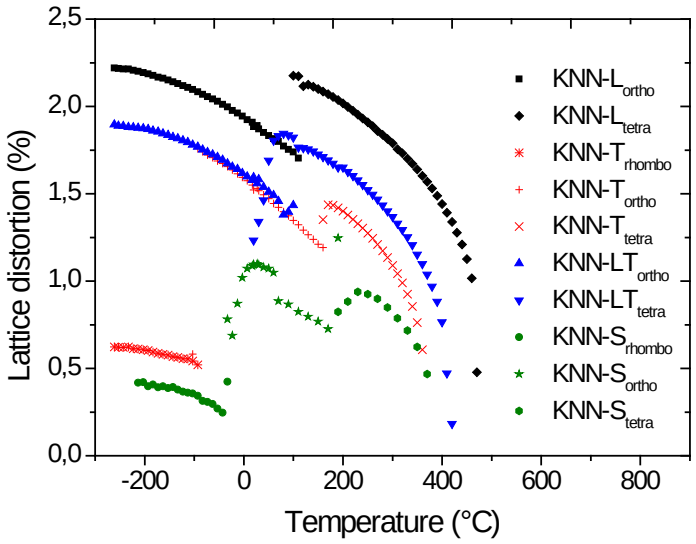

Fig. 7.9 Lattice distortion (%) as a function of temperature for KNN-L, KNN-T, KNN-LT and KNN-S ceramics. Depending on the composition, rhombohedral, orthorhombic and tetragonal distortions were observed.

7.2.4 Electrical characterization

Plots of the dielectric properties for KNN-L, KNN-T, KNN-S and KNN-LT ceramics from room temperature to temperatures above their T_c are shown in Fig. 7.10. The enlarged insets highlight the shape of the curve near the phase transition temperature from orthorhombic to tetragonal $T_{T\text{-}O}$ which is indicated with an arrow. The transition temperatures using dielectric measurement in some samples are slightly different from those identified by X-ray diffraction. A possible reason could be due to differences in strain constraints in the samples used for the measurements. The samples for X-ray diffraction were ground and annealed prior to the measurements while the samples used for dielectric measurements were in pellet form. The powders for X-ray diffraction were rotated during measurement to ensure that averaged results were obtained while fixed bulk ceramic pellets were used for the dielectric measurement.

The phase transition from orthorhombic to tetragonal phase for the KNN-L composition was identified to be at 140 ± 2 °C by a dielectric peak value of 588 and to be at ~120 °C by X-ray diffraction. It has a dielectric peak value of ~10360 at 458 ± 3 °C and at 480 °C for X-ray diffraction. The phase transition from orthorhombic to tetragonal phase for the

KNN-T composition was identified to be at 170 ± 2 °C by a dielectric peak value of 887 and to be at ~170 °C by X-ray diffraction. It has a dielectric peak value of ~4772 at 358 ± 3 °C and at 370 °C for X-ray diffraction. The phase transition from orthorhombic to tetragonal phase for the KNN-LT composition was identified to be at 111 ± 2 °C by a dielectric peak value of 657 and to be at ~110 °C by X-ray diffraction. It has a dielectric peak value of ~5510 at 393 ± 3 °C and at 370 °C for X-ray diffraction. The phase transition from orthorhombic to tetragonal phase for the KNN-S composition was identified to be at 140 ± 2 °C by a dielectric peak value of ~1312 and to be at ~140 °C by X-ray diffraction. It has a dielectric peak value of ~4012 at 306 ± 3 °C and at 340 °C for X-ray diffraction.
The variations in the reported T_c values from literature are not very far apart from our results for similar compositions. For KNN-L composition, a T_{T-O} in the range of ~120 °C - 150 °C and T_c in the range 440 °C – 460 °C have been reported but the peak values were lower [54, 114, 133]. For KNN-T-like compositions, reported T_{T-O} and T_c values were ~187 °C and 350 – 360 °C respectively [58, 60] while for KNN-LT-like compositions, reported T_{T-O} and T_c values were ~20 °C and 350 – 440 °C respectively [68, 140]. The shapes of the peak at the T_{T-O} appear to be more diffuse with increasing temperature range of the phase coexistence in the material.

For the KNN-T composition, the dielectric constant versus temperature curve shows a phase change T_{T-O} at 170 °C. As the degree of phase coexistence increases, the shape of the curve becomes diffuse and the exact transition temperature cannot be clearly identified especially for KNN-LT ceramics (Fig. 7.10a). The plot of dielectric loss in the samples is shown in Fig. 7.10b. For KNN-L and KNN-T compositions, high loss values are obtained compared to KNN-S and KNN-LT composition. This may be due to the smaller ionic radius of Li which leads to high cation vacancies in the lattice as can be observed in the dielectric data at high temperatures. Ta has been reported to give “soft” properties to KNN but it did not translate to higher properties in our work [61]. As the measurement temperature increases, the loss values for KNN-L and KNN-T also increase but the loss values for KNN-S and KNN-LT are in the same range up to 300 °C.

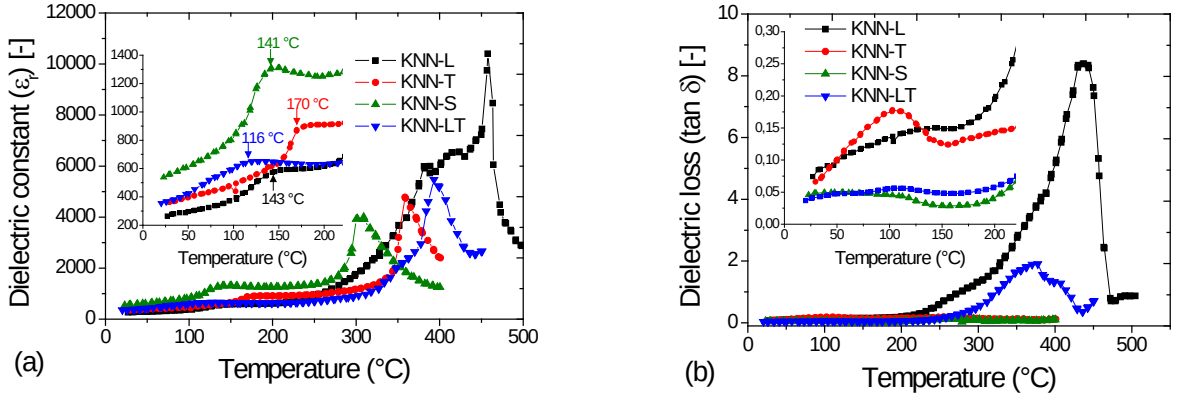

Fig. 7.10 Variation of the (a) dielectric constant and (b) dielectric loss (tan δ) as a function of temperature for KNN-L, KNN-T, KNN-S and KNN-LT ceramics measured at 100 kHz.

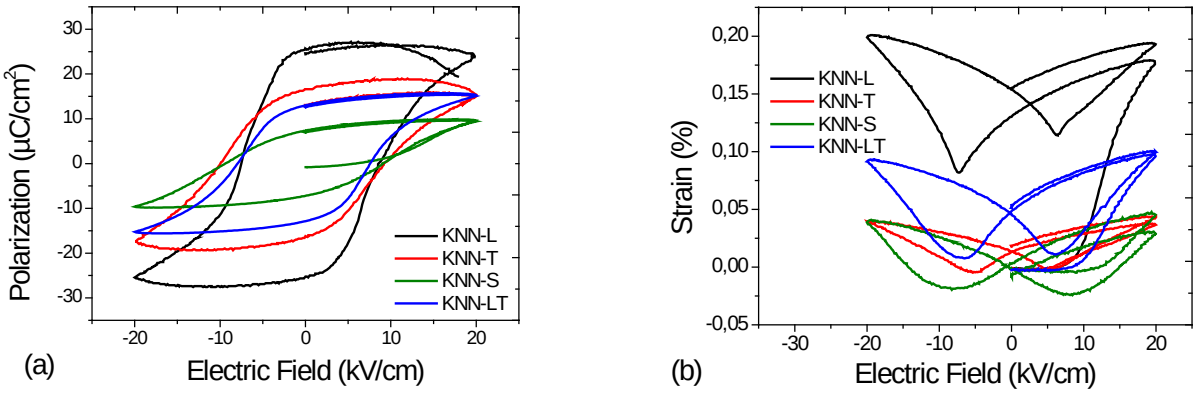

Fig. 7.11 Variation of (a) polarization-field hysteresis loops and (b) strain-field hysteresis loops measured at room temperature for KNN-L, KNN-T, KNN-S and KNN-LT ceramics.

The polarization hysteresis curves for the samples are shown in Fig. 7.11a. When a ~20 kV/cm field is applied, good hysteresis loops were obtained for all the samples and the saturation polarization is obtained for KNN-S and KNN-LT compositions. A 25 μC/cm^2 P_r value is obtained for the KNN-L composition while a ~ 8 kV/cm E_c value is obtained for all compositions. For the KNN-T composition, the P_r is ~16.5 μC/cm^2 and ~13 μC/cm^2 for KNN-LT. P_r values in the literature (17 – 19 μC/cm^2) for compositions close to KNN-T are similar to this result but the difference is that lower applied fields was used here [60].

For KNN-LT compositions, slightly higher P_r values (25 μC/cm^2) were reported in the literature [68]. A P_r of ~7.1 μC/cm^2 and E_c ~9 kV/cm is obtained for the KNN-S composition. This suggests that Sb addition to KNN may result in "hard" ferroelectric properties.

The strain hysteresis loops for the samples which show the typical butterfly shape indicating ferroelectricity are shown in Fig. 7.11b. High remanent strain S_r, (0.0013) is obtained for the KNN-L composition, which is in agreement with the high lattice distortion for the sample in Fig. 7.9. Moderately high S_r was obtained for KNN-LT (0.00047) while a very low S_r (0.000136) was obtained for the KNN-T composition. There are not much strain hysteresis data in the literature with S_r values for comparison. The asymmetry in the loop for KNN-L composition is possibly due to uneven distribution of charges as the field is applied in opposite directions [141, 142].

The piezoelectric charge coefficient d^*_{33} values for the samples obtained using high signal measurements is shown in Table 7.9.

Table 7.9 Density, P_r, E_c S_r and d^*_{33} values for KNN-L, KNN-T, KNN-S and KNN-LT ceramics measured at room temperature

Composition	Density (g/cm^3)	Theoretical Density @ 20 °C (g/cm^3)	Remanent polarization P_r (μC/cm^2)	Coercive field E_C (kV/cm)	Remanent strain S_r	Piezoelectric coefficient d^*_{33} (pm/V)
KNN-L	4.12±0.04	4.44	25.0	8.0	0.0013	207±8
KNN-T	4.40±0.07	4.71	16.5	7.8	0.000136	104±15
KNN-LT	4.23±0.03	4.70	13.0	7.8	0.00047	228±6
KNN-S	4.07±0.05	4.59	7.1	9.0	0.00003	223±21

The highest values of ~230 pm/V are from KNN-S and KNN-LT compositions followed by KNN-L with a value of 207 ± 8 pm/V. It is believed that the coexistence of more than one phase in a piezoelectric ceramic will result in higher piezoelectric properties. This result however shows that this assumption may not always be the case. It may apply for some compositions (in this case KNN-L and KNN-T) and not in others (KNN-S). The highest relative density value of ~93% was obtained with the KNN-T composition but the d^*_{33} was the lowest (103 ± 15 pm/V). A slightly higher d_{33} value was reported in the literature for the KNN-T composition and this increment was attributed to "softening" of

the ceramics due to the presence of $KTaO_3$ [58]. Slightly lower values are reported for KNN-L compositions [131, 133] and for KNN-LT-like compositions, a range of values were reported depending on the composition [68, 114, 140]. A summary of the density, P_r, E_c, S_r and d^*_{33} values are shown in Table 7.9

7.2.5 Discussion

Materials which undergo a first order phase transition exhibit a discontinuity in their polarization, lattice parameters and other properties [18]. The lattice parameters for all the samples show discontinuities at the phase transitions (Fig. 7.8) which indicates that they all undergo a first order phase transition. Noheda et al. [143] reported that when there is a second order phase transition, no phase coexistence should be observed. The presence of phase coexistence here confirms a first order phase transition in the samples. It is not clear if the phase coexistence is an intrinsic feature of modified KNN ceramics or just a compositional fluctuation over a small range of temperature or composition. More research needs to be done to verify that.

The chemical composition and radii of the ions influence how ferroelectric phases are formed. Li with 6 fold coordination has a very small ionic radius (76 pm) compared to either K (164 pm) or Na (139 pm) with 12 fold coordination. Ta being a transition element, has different valent states which leads to strong changes in the ionic radius. If the valence state is +5, then the ionic radius is the same with that of Nb (64 pm) (6 fold coordination) and as the valence state decreases, the ionic radius increases [144]. The huge difference in the ionic radius of Li compared to A-site elements which it replaces may explain why the rhombohedral low temperature phase is suppressed while the T_c is shifted to higher temperatures. Similar results have been reported for Ca and Pb doped $BaTiO_3$ where the T_c increased with doping while other phase transition temperatures decreased [145]. For a coordination number of 12, the ionic radii of Ba, Ca and Pb are 1.61, 1.34 and 1.49 respectively. Both elements have a smaller ionic radius compared to Ba giving them more space and higher atomic and electronic polarizability respectively, which intensifies the interactions between the Ti ions [145].

Addition of dopants is known to result in the lowering of the phase transition temperatures [146]. Instead of the normal morphotropic phase boundrary that is observed in PZT, a polymorphic phase transition (PPT) occurs and this is both a composition and temperature

dependent phenomenon. Phase coexistence leads to the formation of a polymorphic phase boundary which results in higher piezoelectric properties compared to pure KNN especially for isovalent dopants. The increase in the number of possible polarization directions is also a possible reason for the enhanced properties. A total of 18 possible polarization directions of the domains are therefore available for a mixture of orthorhombic (12 $[110]_c$) and tetragonal phases (6 $[001]_c$). Polycrystalline constraints, domain wall motion and interphase boundary motion have also been reported to have significant effects on the piezoelectric and electromechanical properties [147]. As the temperature range of the phase coexistence becomes wider, the piezoelectric coefficient becomes higher especially for KNN with Li, Ta and Sb [4, 148] but unlike in PZT, the enhancement in the d_{33} value is not extremely high at the phase boundary.
Addition of more than 10 mol% Sb to KNN has been reported to result in the formation of a new phase at room temperature. This phase has been identified to be of rhombohedral symmetry using temperature dependent dielectric studies [117, 135]. This is in agreement with our result where the $T_{o\text{-}r}$ was observed at -83 °C with 5 mol% Sb. It is clear that as more Sb is added, this transition point will be elevated to higher temperatures.

The dielectric constant values always peak at the T_c because the polarizability of the lattice is higher and is associated with the free conducting electrons created by cation vacancies [149]. The highest value of dielectric constant at T_c is with the KNN-L composition (Fig. 7.13a) and it also has the highest dielectric loss values. As the temperature increases, it is probable that interfacial ionic polarization within the Nb-O framework is created and this gives rise to large dielectric constants [150]. This motion of the Li also accounts for the high dielectric loss in KNN-L composition. It can also be explained in terms of the mobility of the free electronic or ionic charges in the sample leading to ease of domain wall movement and therefore high dielectric loss. When Ta is added to the Li (KNN-LT), it appears that this motion is reduced in the lattice leading to reduced dielectric constant and loss values.

A decrease in the lattice distortion also results in the reduction of both the spontaneous polarization and strain [151]. The high P_r value for KNN-L is related to the high lattice distortion at all temperatures. Addition of Ta to Li in KNN (KNN-LT) decreases both the lattice distortion and the spontaneous polarization and remanent strain. Low distortion values were obtained for KNN-T possibly because with a coordination number of 6 and

valency of +5, they both have the same ionic radius (64 pm). The uneven strain hysteresis loop for KNN-L (Fig. 7.11b) is possibly due to inhomogeneities in the charge carrier densities in the sample [141]. The d^*_{33} value for the KNN-T composition is low even when the density is higher than other compositions possibly due to the difficulty of aligning the domains when the electric field is applied.

7.2.6 Summary

Synchrotron X-ray diffraction has been used to characterize KNN-based compositions from -261 °C to temperatures above their respective T_c values. OES/ICP analysis showed that after sintering, elements with high vapor pressure (Li and K) are lower than the intended compositions and that ZrO_2 is introduced to the samples due to friction between the milling balls, powder and stirrer. Li in KNN suppresses the formation of the rhombohedral low temperature phase and this is attributed to the size difference between the ionic radii of the A-site elements. When only Ta or Sb is added to KNN, the $T_{r\text{-}o}$ is observed at ~ -103 °C. With co-doping of Li, Ta and Sb in KNN, a wide temperature range of phase coexistence are observed with a slightly higher piezoelectric coefficient due to higher possible polarization directions. High dielectric constant peaks, lattice distortion, spontaneous polarization and strain and dielectric constants are obtained when Li is added to KNN ceramics. This is attributed to the ease of domain wall movement, and high mobility of the free electrons or ionic charges in the sample. The existence of more than one phase in a piezoelectric ceramic does not necessarily translate into much higher piezoelectric coefficients. While for some compositions like KNNwith Li, Ta and Sb, the d_{33} values are considerably higher, it was not for others. A higher density value does not always translate to high piezoelectric properties as there are other determining factors involved.

8 Conclusion

In this dissertation, the structure and properties of lead-free $(K_xNa_{1-x})NbO_3$-based piezoelectric ceramics doped with lithium, tantalum, antimony, manganese and bismuth were investigated using both conventional mixed-oxide ceramics synthesis method and high-throughput experimentation (HTE) method. Structural analysis was done using Rietveld refinement with Fullprof software.

$(K_{0.44}Na_{0.52}Li_{0.04})(Nb_{0.86}Ta_{0.1}Sb_{0.04})O_3$ ferroelectric ceramics was doped with 0, 0.5, 1 and 2.5 mol% manganese in order to understand its effect on the properties. A combination of hard and soft ferroelectric effects was obtained. It is believed that Mn acted both as a donor and as an acceptor which led to the introduction of both cation and oxygen vacancies into the perovskite lattice. The Curie temperatures and the tetragonal-orthorhombic phase transition temperatures were lowered due to inhomogenous electric fields produced by these vacancies. The remanent polarization, average grain sizes and piezoelectric coefficients decreased with Mn addition which indicates hardening of the ferroelectric. The dielectric constant was higher at room temperature with Mn addition while the dielectric loss values and the coercive field decreased which indicates softening. The sample containing 1 mol% of Mn gave the best properties.

Antimony was used to substitute for niobium in $(K_{0.5}Na_{0.5})NbO_3$ ceramics from 0 mol% to 14 mol% with a doping step of 2 mol%. There was no trend in the obtained density values with Sb addition of up to 8 mol% while the density values increased with more dopant amount. The diffraction patterns showed that the orthorhombic phase was present without doping and as Sb amount in the sample increased, the crystal structure gradually changed

from an orthorhombic phase to a pseudocubic phase with more than 8 mol% Sb. A rod-like Sb rich second phase related to $K_2NaSb_3O_9$ is observed with more than 10 mol% Sb content with precipitates mainly at the grain boundaries. Energy dispersive X-ray spectroscopy analysis shows that A-site vacancies exist in the lattice while the microstructures show rod-like grains which segregated mainly at the grain boundary. The temperature of phase transitions dcreased with increasing Sb amount due to inhomogeneities due to the vacancies and as the amount of the dopant increased, a diffuse phase transition is observed. Good hysteresis curves were obtained for samples with Sb amounts ≤ 8 mol% while large leakage currents were observed for samples > 8 mol%. The mechanical quality factor of the samples show that Sb softens the $(K_{0.5}Na_{0.5})NbO_3$ ceramics. The sample with 4 mol% Sb content gave the best properties (k_p = 0.46, Q_m = 6.2, N_p = 2296).

Bismuth has a valent state of +3 and theoretically can be incorporated to both the A-site and B-site of the perovskite lattice. It was used to dope $(K_xNa_{1-x})NbO_3$-based ceramics on both the A- and B-sites of the lattice from 0 mol% to 1 mol% with a doping step of 0.1 mol%. Bi on the A-site of $(K_{0.5}Na_{0.5})NbO_3$ ceramics (KNN-A), on the B-site of $(K_{0.5}Na_{0.5})NbO_3$ ceramics (KNN-B), on the A-site of $(K_{0.48}Na_{0.48}Li_{0.04})(Nb_{0.9}Ta_{0.1})O_3$ ceramics (KNNLT-A), on the B-site of $(K_{0.48}Na_{0.48}Li_{0.04})(Nb_{0.9}Ta_{0.1})O_3$ ceramics (KNNLT-B) and on $(K_{0.48}Na_{0.48}Li_{0.04})(Nb_{0.85}Ta_{0.1}Sb_{0.05})O_3$ ceramics (KNNLST) were produced. High-throughput experimentation (HTE) method was used to investigate the effect of Bi on the piezoelectric properties of these ceramics. It was also done to show that the results obtained by the HTE method are comparable to those obtained through the conventional processing method.

High density values were obtained when the appropriate sintering temperature was used and the reproducibility test showed that samples with reproducible properties can be produced. Different phases were observed from the diffraction patterns as the amount of Bi increased. KNN-A compositions remained orthorhombic up to 1 mol% Bi while KNN-B compositions changed from orthorhombic to pseudocubic phase. KNNLT compositions changed from a two-phase (orthorhombic-tetragonal) to a tetragonal phase with doping

while KNNLST compositions changed from tetragonal to pseudocubic with more than 0.7 mol% Bi amount. The SEM images showed that Bi addition to KNN ceramics decreased the average grain size with a remarkable reduction for KNN-B compositions. The dielectric constant values increased in the following order; KNN compositions, KNNLTcompositions and KNNLST compositions but there was no significant difference in the dielectric loss values. Samples with high dielectric loss values also had low resistivity values. Good hysteresis curves were obtained for some samples especially for KNNLT and KNNLST compositions. The highest piezoelectric coefficient value (d^*_{33} ~430 pm/V) was obtained for KNNLST composition doped with 0.1 mol% Bi.

The lattice parameters, lattice distortion, phase coexistence, theoretical densities and other structural information about $(K_xNa_{1-x})NbO_3$-based ceramics gained by synchrotron X-ray diffraction were determined using Rietveld refinement. The chemical analysis using OES/ICP method showed that the actual compositions are in most cases slightly different from the intended compositions. This is mainly due to impurities introduced during processing and element loss during sintering. Lower contents of Li, Sb and K were observed while Na and Ta had slightly higher amounts. Zr was always introduced during the milling process using ZrO_2 balls.

The sequence of phase transitions from low temperatures for $(K_{0.49}Na_{0.51})(Nb_{0.88}Ta_{0.1})O_3$ ceramics (KNN-T) and $(K_{0.48}Na_{0.55})(Nb_{0.92}Sb_{0.05})O_3$ ceramics (KNN-S) samples runs from rhombohedral to orthorhombic to tetragonal and finally cubic phase while the sequence for $(K_{0.47}Na_{0.51}Li_{0.03})NbO_{3.01}$ ceramics (KNN-Li), $(K_{0.47}Na_{0.51}Li_{0.025})(Nb_{0.88}Ta_{0.1})O_{3.02}$ ceramics (KNN-LT) and $(K_{0.37}Na_{0.52}Li_{0.03})(Nb_{0.87}Ta_{0.1}Sb_{0.03})O_3$ ceramics (KNNLST) samples runs from orthorhombic to tetragonal and finally to the cubic phase. Hence Li suppresses the formation of the rhombohedral phase in KNN-based ceramics. High lattice distortion, Curie temperature, remanent polarization and remanent strain were obtained with KNN-L ceramics possibly due to the smaller size of the Li ion compared to other A-site elements. Phase coexistence over a wide range of temperatures is observed for KNN-LT and KNNLST compositions while for KNN-Li, KNN-Ta and KNN-Sb, phase coexistence is observed only near the phase transition regions. Good agreement in the phase transition

temperature is obtained between the X-ray diffraction and high temperature dielectric measurement. The extensive phase coexistence near room temperature leads to more polarization directions which explain in part why the piezoelectric response of samples with KNN-LT and KNNLST compositions is higher than in other compositions.

References

[1] D. Berlincourt, "Piezoelectric ceramics: Characterisation and applications," *J Acoust. Soc. Am.,* vol. 70, pp. 1586-1595, 1981.

[2] H. Needleman, "Lead Poisoning," *Annu. Rev. Med,* vol. 55, pp. 209-222, 2004.

[3] E. p. a. t. Council, "Directive 2002/95/EC of the European parliament and of the council of January 2003 on the restriction of the use of harzardous substances in electrical and electronic equipment. ," *European Journal,* vol. 37, p. 19, 13/2/2003 2003.

[4] Y. Saito, H. Takao, T. Tani, T. Nonoyama, K. Takatori, T. Homma, T. Nagaya, and M. Nakamura, "Lead-free Piezoceramics," *Nature,* vol. 432, pp. 84-87, 2004.

[5] T. Takenaka, K. Sakata, and K. Toda, "Piezoelectric Properties of $(Bi_{1/2}Na_{1/2})TiO_3$-based ceramics," *Ferroelectrics,* vol. 106, pp. 375-380, 1990.

[6] K.-i. Kakimoto, T. Yoshifuji, and H. Ohsato, "Densification of tungsten-bronze $KBa_2Nb_5O_{15}$ lead-free piezoceramics," *J. Eur. Ceram. Soc.,* vol. 27, pp. 4111-4114, 2007.

[7] J. Gopalakrishnan, "Synthesis and structure of some interesting oxides of bismuth," *Proc. Indian Acad. Sci.,* vol. 96, pp. 449-458, 1986.

[8] L. Egerton and D. M. Dillion, "Piezoelectric and dielectric properties of ceramics in the system potassium-sodium niobate," *J. Am. Ceram. Soc,* vol. 42, pp. 438-442, 1959.

[9] E. J. Amis, X.-D. Xiang, and J.-C. Zhao, "Combinatorial Materials science: What's new since Edition?," *MRS Bulletin,* pp. 295-300, 2002.

[10] J. N. Cawse, "Experimental Design for Combinatorial and High throughput materials development," J. N. Cawse, Ed.: Wiley, 2003, pp. 1-24.

[11] S. Schmatloch and U. S. Schubert, "Techniques and Instrumentation for Combinatorial and High-Throughput Polymer Research: Recent Developments," *Macromol. Rapid. Commun.,* vol. 25, pp. 69-76, 2004.

[12] I. Hahndorf, O. Buyevskaya, M. Langpape, G. Grubert, S. Kolf, E. Guillon, and M. Baerns, "Experimental equipment for high-throughput synthesis and testing of catalytic materials," *Chem. Engineering Journal,* vol. 89, pp. 119-125, 2002.

[13] C. Schroeter, B. Wessler, A. Schoenecker, U. Keitel, and L. M. Eng, "High throughput screening of ferroelectric thin film libraries," *J Appl. Phys.*, vol. 100, 2006.

[14] A. Cardin, B. Wessler, C. Schuh, T. Steinkopff, and W. F. Maier, "High throughput experimentation for the development of new piezoelectric ceramics," *J. Electroceram.*, vol. 19, pp. 267-272, 2007.

[15] C. Schroeter, B. Wessler, and L. M. Eng, "High throughput method for $K_{0.5}Na_{0.5}NbO_3$ thin films preparation by Chemical solution deposition," *J. Eur. Ceram. Soc.*, vol. 27, pp. 3785-3788, 2007.

[16] G. H. Haertling, "Ferroelectric Ceramics: History and Technology," *J. Am. Ceram. Soc.*,, vol. 82, pp. 797–818, 1999.

[17] B. Jaffe, H. Jaffe, and W. R. Cook, "Piezoelectric Ceramics," *Academic Press, London*, 1971.

[18] U. Boettger, "Dielectric properties of polar oxides," in *Polar oxides*, R. Waser, U. Boettger, and S. Tiedke, Eds. Weinheim: Wiley-VCH, 2004, pp. 11-37.

[19] I. Flinn, "Piezoelectric ceramics and their applications," *Physics education*, pp. 274-280, 1975.

[20] H. Thomann, "Piezoelectric Ceramics," *Adv. Mater.* , vol. 2, pp. 458-463, 1990.

[21] S. R. McLaughlin, "Fabrication and Properties of $Bi_{1/2}Na_{1/2}TiO_3$ Based Ferroelectric Ceramics with Low Levels of B-site Additives," in *Mechanical and Materials Engineering*. vol. Doctor of Philosophy Ontario: Queen's University, 2008, p. 152.

[22] A. I. S. 180-1986, "IEEE Standard Definitions of Primary Ferroelectric Terms," pp. 1-24, 1986.

[23] A. J. Moulson and J. M. Herbert, "Electroceramics: Materials, Properties, Applications. ," vol. 2nd Edition, p. 340, 2003.

[24] R. A. D. Souza, M. S. Islam, and E. Ivers-Tiffe´e, "Formation and migration of cation defects in the perovskite oxide $LaMnO_3$," *J. Mat. Chem.*, vol. 9, pp. 1621–1627, 1999.

[25] C. Kittel, *Introduction to Solid State Physics* vol. 8. Hoboken, NJ: John Wiley & Sons, 2005.

[26] V. M. Goldschmidt, *Skrifter Norske Videnskaps-Akad. Mater,* vol. naturvid. Kl, p. 2, 1926.

[27] W. F. Maier, K. Stowe, and S. Sieg, "Combinatorial and high throughput materials science," *Angew. Chem. Int. Ed.,* vol. 46, pp. 6016-6067, 2007.

[28] A. Siegel, "Combinatorial synthesis of advanced ceramic materials," *Canadian ceram.,* pp. 17-21, 1998.

[29] J. N. Cawse, "Experimental strategies for combinatorial and high throughput materials development," *Acc. Chem. Res,* vol. 34, pp. 213-221, 2001.

[30] L. Harmon, "Experiment planning for combinatorial materials discovery," *J Mat. Sci.,* vol. 38, pp. 4479-4485, 2003.

[31] K. Kennedy, T. Stefansky, G. Davy, V. F. Zackay, and E. R. Parker, "Rapid method for determining Ternary-alloy phase diagrams," *J Appl. Phys.,* vol. 36, pp. 3808-3810, 1965.

[32] J.-C. Zhao, "Combinatorial approaches as effective tools in the study of phase diagrams and composition–structure–property relationships," *Progress in Mat. Sci.,* vol. 51, pp. 557-631, 2006.

[33] J. J. Hanak, "The "Multiple-sample concept" in materials research: synthesis, compositional analysis and testing of entire multicomponent systems," *J Mat. Sci.,* vol. 5, pp. 964-971, 1970.

[34] R. A. Potyrailo and I. Takeuchi, "Role of high-throughput characterization tools in combinatorial materials science " *Meas. Sci. Technol.,* vol. 16, pp. 1-4, 2004.

[35] P. Bomlai and P. Wichianrat, "Effect of Calcination Conditions and Excess Alkali Carbonate on the Phase Formation and Particle Morphology of $Na_{0.5}K_{0.5}NbO_3$ Powders," *J. Am. Ceram. Soc,* vol. 90, pp. 1650-1655, 2007.

[36] M. Fukada, T. Saito, H. Kume, and T. Wada, "Fabrication of Lead-Free Piezoelectric $(Na_{0.5}K_{0.5})NbO_3$ Ceramics by a Modified Solid-State Reaction Method," *IEEE-UFFC Transactions,* vol. 55, pp. 988-993, 2008.

[37] H. Yang, Y. Lin, J. Zhu, and F. Wang, "An efficient approach for direct synthesis of $K_{0.5}Na_{0.5}NbO_3$," *Powd. Technol.,* vol. 196, pp. 233-236, 2009.

[38] J. Acker, H. Kungl, and M. J. Hoffmann, "Influence of Alkaline and Niobium Excess on Sintering and Microstructure of Sodium-Potassium Niobate $(K_{0.5}$ $Na_{0.5})NbO_3$," *J. Am. Ceram Soc.,* vol. 93, pp. 1270-1281, 2010.

[39] T. Rojac, M. Kosec, B. Malic, and J. Holc, "Mechanochemical Synthesis of $NaNbO_3$, $KNbO_3$ and $K_{0.5}Na_{0.5}NbO_3$," *Science of Sint.*, vol. 37, pp. 61-67, 2005.

[40] E. Ringgaard and T. Wurlitzer, "Lead-Free Piezoceramics Based On Alkali Niobates," *J. Eur. Ceram. Soc.*, vol. 25, pp. 2701–2706, 2005.

[41] Y. Shiratori, A. Magrez, and C. Pithan, "Particle size effect on the crystal structure symmetry of $K_{0.5}Na_{0.5}NbO_3$," *J. Eur. Ceram. Soc.*, vol. 25, pp. 2075-2079, 2005.

[42] C. Pithan, Y. Shiratori, J. Dornseiffer, F.-H. Haegel, A. Magrez, and R. Waser, "Microemulsion mediated synthesis of nanocrystalline $(K_x,Na_{1-x})NbO_3$ powders," *J. Cryst. Growth.*, vol. 280, pp. 191-200, 2005.

[43] M. A. L. Nobre and S. Lanfredi, "Dielectric loss and phase transition of sodium potassium niobate ceramic investigated by impedance spectroscopy," *Catalysis Today*, vol. 78, pp. 529-538, 2003.

[44] R. J. C. Lima, W. Paraguassu, P. T. C. Freire, J. M. Sasaki, F. E. A. Melo, J. M. Filho, and S. Lanfredi, "Temperature-dependent Raman spectra of $K_{0.2}Na_{0.8}NbO_3$ ceramics," *J. Raman Spectrosc.*, vol. 36, pp. 28-32, 2005.

[45] J. G. Fisher, D. Rout, K.-S. Moon, and S.-J. L. Kang, "Structural changes in potassium sodium niobate ceramics sintered in different atmospheres," *J. Alloy.& Compds.* , vol. 479, pp. 467-472, 2009.

[46] J. G. Fisher, D. Rout, K.-S. Moon, and S.-J. L. Kang, "High-temperature X-ray diffraction and Raman spectroscopy study of $(K_{0.5}Na_{0.5})NbO_3$ ceramics sintered in oxidizing and reducing atmospheres," *Mat. Chem. & Phys.*, vol. 120, pp. 263-271, 2010.

[47] R. E. Jaeger and L. Egerton, "Hot pressing of potassium-sodium niobates," *J. Am. Ceram. Soc*, vol. 45, pp. 209-213, 1962.

[48] G. H. Haertling, "Properties of Hot-Pressed Ferroelectric Alkali Niobate Ceramics," *J. Am. Ceram Soc.* , vol. 50, pp. 329-330, 1967.

[49] K. Wang, B.-P. Zhang, J.-F. Li, and L.-M. Zhang, "Lead-free $Na_{0.5}K_{0.5}NbO_3$ piezoelectric ceramics fabricated by spark plasma sintering: Annealing effect on electrical properties," *J. Electroceram.*, vol. 21, pp. 251-254, 2008.

[50] J.-F. Li, K. Wang, B.-P. Zhang, and L.-M. Zhang, "Ferroelectric and Piezoelectric Properties of Fine-Grained $Na_{0.5}K_{0.5}NbO_3$ Lead-Free Piezoelectric Ceramics Prepared by Spark Plasma Sintering," *J. Am. Ceram. Soc*, vol. 89, pp. 706-709, 2006.

[51] M. Zhang, M. Guo, and Y. Zhou, "Low-Temperature Preparation of $K_xNa_{(1-x)}NbO_3$ Lead-Free Piezoelectric Powders by Microwave-Hydrothermal Synthesis," *Int. J. Appl. Ceram. Technol,* pp. 1-6, 2009.

[52] Y. Guo, K.-i. Kakimoto, and O. Hitoshi, "Phase transitional behavior and piezoelectric properties of $Na_{0.5}K_{0.5}NbO_3$–$LiNbO_3$ ceramics," *Appl. Phys. Lett.,* vol. 85, pp. 4121-4123, 2004.

[53] E. Hollenstein, D. Damjanovic, and N. Setter, "Temperature stability of the piezoelectric properties of Li-modified KNN ceramics," *J. Eur. Ceram. Soc.,* vol. 27, pp. 4093-4097, 2007.

[54] N. Klein, E. Hollenstein, D. Damjanovic, H. J. Trodahl, and N. Setter, "A study of the phase diagram of (K,Na,Li)NbO_3 determined by dielectric and piezoelectric measurements, and Raman spectroscopy," *J. Appl. Phys.,* vol. 102, 2007.

[55] K. Chen, G. Xu, D. Yang, X. Wang, and J. Li, "Dielectric and piezoelectric properties of lead-free $0.95(K_{0.5}Na_{0.5})NbO_3$–$0.05LiNbO_3$ crystals grown by the Bridgman method," *J. Appl. Phys.,* vol. 101, 2007.

[56] X. X. Wang, S. W. Or, K. H. Lam, H. L. W. C., P. K. Choy, and P. C. K. Liu, "Cymbal actuator fabricated using $(Na_{0.46}K_{0.46}Li_{0.08})NbO_3$ lead-free piezoceramic," *J. Electroceram.,* vol. 16, pp. 385-388, 2006.

[57] D. Lin, K. W. Kwok, H. Tian, H. Wong, and L.-w. Chan, "Phase Transitions and Electrical Properties of $(Na_{1-x}K_x)(Nb_{1-y}Sb_y)O_3$ Lead-Free Piezoelectric Ceramics With a MnO_2 Sintering Aid," *J. Am. Ceram. Soc.,* vol. 90, pp. 1458-1462, 2007.

[58] D. Lin, K. W. Kwok, and H. L. W. Chan, "Phase transition and electrical properties of $(K_{0.5}Na_{0.5})(Nb_{1-x}Ta_x)O_3$ lead-free piezoelectric ceramics," *Appl. Phys. A,* vol. 91, pp. 167-171, 2008.

[59] H. Tian, Z. Zhou, D. Gong, H. Wang, D. Liu, and Y. Jiang, "Growth and optical properties of paraelectric $K_{1-y}Na_yTa_{1-x}Nb_xO_3$ single crystals," *Appl. Phys. B,* vol. 91, pp. 75-78, 2008.

[60] M. Matsubara, T. Yamaguchi, W. Sakamoto, K. Kikuta, T. Yogo, and H. Shin-ichi, "Processing and Piezoelectric Properties of Lead-Free (K,Na) (Nb,Ta) O_3 Ceramics," *J. Am. Ceram. Soc.,* vol. 88, pp. 1190–1196, 2005.

[61] Y. Saito and H. Takao, "High Performance Lead-free Piezoelectric Ceramics in the (K,Na)NbO_3-$LiTaO_3$ Solid Solution System," *Ferroelectrics,* vol. 338, pp. 17–32, 2006.

[62] T. A. Skidmore and S. J. Milne, "Phase development during mixed-oxide processing of a $[Na_{0.5}K_{0.5}NbO_3]_{1-x}$–$[LiTaO_3]_x$ powder," *J. Mater. Res.*, vol. 22, pp. 2265-2272, 2007.

[63] Y. Zhen and J.-F. Li, "Abnormal Grain Growth and New Core–Shell Structure in (K,Na)NbO_3-Based Lead-Free Piezoelectric Ceramics," *J. Am. Ceram. Soc.*, vol. 90, pp. 3496-3502, 2007.

[64] M.-S. Kim, D.-S. Lee, E.-C. Park, S.-J. Jeong, and J.-S. Song, "Effect of Na_2O additions on the sinterability and piezoelectric properties of lead-free $95(Na_{0.5}K_{0.5})NbO_3$–$5LiTaO_3$ ceramics," *J. Eur. Ceram. Soc.*, vol. 27, pp. 4121-4124, 2007.

[65] M.-S. Kim, S.-J. Jeong, and J.-S. Song, "Microstructures and Piezoelectric Properties in the Li_2O-Excess $0.95(Na_{0.5}K_{0.5})NbO_3$–$0.05LiTaO_3$ Ceramics," *J. Am. Ceram. Soc*, vol. 90, pp. 3338-3340, 2007.

[66] D. Lin, K. W. Kwok, and H. L. W. Chan, "Effects of BaO on the structure and electrical properties of $0.95K_{0.5}Na_{0.5}(Nb_{0.94}Sb_{0.06})O_3$–$0.05LiTaO_3$ lead-free ceramics," *J. Phys. D: Appl. Phys.*, vol. 40, pp. 6778-6783, 2007.

[67] P. Bomlai, P. Sinsap, S. Muensit, and S. J. Milne, "Effect of MnO on the Phase Development, Microstructures, and Dielectric Properties of $0.95Na_{0.5}K_{0.5}NbO_3$–$0.05LiTaO_3$ Ceramic," *J. Am. Ceram. Soc*, vol. 91, pp. 624-627, 2008.

[68] Y. Chang, Z. Yang, D. Ma, Z. Liu, and Z. Wang, "Phase coexistence and high electrical properties in $(K_xNa_{0.96-x}Li_{0.04})(Nb_{0.85}Ta_{0.1})O_3$ piezoelectric ceramics," *J. Appl. Phys.*, vol. 105, 2009.

[69] J. Wu, D. Xiao, Y. Wang, J. Zhu, P. Yu, and Y. Jiang, "Compositional dependence of phase structure and electrical properties in $(K_{0.42}Na_{0.58})NbO_3$-$LiSbO_3$ lead-free ceramics," *J. Appl. Phys.*, vol. 102, 2007.

[70] J. Wu, D. Xiao, Y. Wang, J. Zhu, and P. Yu, "Effects of K content on the dielectric, piezoelectric, and ferroelectric properties of $0.95(K_xNa_{1-x})NbO_3$−$0.05LiSbO_3$ lead-free ceramics," *J. Appl. Phys.*, vol. 103, 2008.

[71] H. Li, W. Y. Shih, and W.-H. Shih, "Effect of Antimony Concentration on the Crystalline Structure, Dielectric, and Piezoelectric Properties of $(Na_{0.5}K_{0.5})0.945Li_{0.055}Nb_{1-x}Sb_xO_3$ Solid Solutions," *J. Am. Ceram. Soc*, vol. 90, pp. 3070-3072, 2007.

[72] S. Zhang, R. Xia, and T. R. Shrout, "Modified $(K_{0.5}Na_{0.5})NbO_3$ based lead-free piezoelectrics with broad temperature usage range," *Appl. Phys. Lett.*, vol. 91, 2007.

[73] S. Zhang, R. Xia, H. Hao, H. Liu, and T. R. Shrout, "Mitigation of thermal and fatigue behavior in $K_{0.5}Na_{0.5}NbO_3$-based lead free piezoceramics," *Appl. Phys. Lett,* vol. 92, 2008.

[74] H. Li, W.-H. Shih, and W. Y. Shih, "Lead-Free Piezoelectric Freestanding Films with Sheet Geometry-Enhanced High-Field Piezoelectric Coefficients," *J. Am. Ceram Soc.,* vol. 93, pp. 1852-2855, 2010.

[75] J. Ryu, J.-J. Choi, B.-D. Hahn, D.-S. Park, and W.-H. Yoon, "Ferroelectric and piezoelectric properties of $0.948(K_{0.5}Na_{0.5})NbO_3–0.052LiSbO_3$ lead-free piezoelectric thick film by aerosol deposition," *Appl. Phys. Lett.,* vol. 92, 2008.

[76] Y. Zhou, J. Zhang, L. Lia, Y. Su, J. Cheng, and S. Caoa, "Multiferroic composites in nano–microscale with non-solid solution by Co-ferrite and $(K_{0.5}Na_{0.5})NbO_3$-based ferroelectric matrix," *J. of Alloys and Compds,* vol. 484, pp. 535-539, 2009.

[77] E. K. Akdoğan, K. Kerman, M. Abazari, and A. Safari, "Origin of high piezoelectric activity in ferroelectric $(K_{0.44}Na_{0.52}Li_{0.04})−(Nb_{0.84}Ta_{0.1}Sb_{0.06})O_3$ ceramics," *Appl. Phys. Lett.,* vol. 92, 2008.

[78] N. M. Hagh, B. Jadidian, and A. Safari, "Property-processing relationship in lead-free (K, Na, Li) NbO_3-solid solution system," *J. Electroceramics,* vol. 18, 2007.

[79] Y. Chang, Z. Yang, Y. Hou, Z. Liu, and Z. Wang, "Effects of Li content on the phase structure and electrical properties of lead-free $(K_{0.46-X/2}Na_{0.54-X/2}Li_x)(Nb_{0.76}Ta_{0.20}Sb_{0.04})O_3$ Ceramics," *Appl. Phys. Lett,* vol. 90, June 5 2007 2007.

[80] Y. Chang, Z. Yang, and L. Wei, "Microstructure, Density, and Dielectric Properties of Lead-Free $(K_{0.44}Na_{0.52}Li_{0.04})(Nb_{0.96-x}Ta_xSb_{0.04})O_3$ Piezoelectric Ceramics," *J. Am. Ceram. Soc.,* vol. 90, pp. 1656-1658, 2007.

[81] J. Fu, R. Zuo, Y. Wu, Z. Xu, and L. Liz, "Phase Transition and Electrical Properties of Li-and Ta-Substituted $(Na_{0.52}K_{0.48})(Nb_{0.96}Sb_{0.04})O_3$ Piezoelectric Ceramics," *J. Am. Ceram Soc.,* vol. 91, pp. 3771-3773, 2008.

[82] F. Rubio-Marcos, M. A. B. nares, J. J. Romeroa, and J. F. Fernandeza, "Correlation between the piezoelectric properties and the structure of lead-free KNN-modified ceramics, studied by Raman Spectroscopy," *J. Raman Spectrosc.,* 2010.

[83] M. Abazari, T. Choi, S.-W. Cheong, and A. Safari, "Nanoscale characterization and local piezoelectric properties of lead-free KNN-LT-LS thin films," *J. Phys. D: Appl. Phys.,* vol. 43, 2010.

[84] S. Körbel, P. Marton, and C. Elsässer, "Formation of vacancies and copper substitutionals in potassium sodium niobate under various processing conditions," *Phys. Rev. B,* vol. 81, 2010.

[85] P. Ghosez, E. Cockayne, U. V. Waghmare, and K. M. Rabe, "Lattice dynamics of $BaTiO_3$, $PbTiO_3$ and $PbZrO_3$: a comparative first-principles study," *arXiv:cond-mat/9901246v2 [cond-mat.mtrl-sci]*, pp. 1-11, 1999.

[86] T. A. Stegk, R. Janssen, and G. A. Schneider, "High-Throughput Synthesis and Characterisation of Bulk Ceramics from Dry Powders " *J. Comb. Chem.*, vol. 10, pp. 274-279, 2008.

[87] V. K. Pecharsky and P. Y. Zavalij, *Fundamentals of Powder Diffraction and Structural Characterizationof Materials*, Second ed.: Springer, 2009.

[88] J. Ihringer and A. Küster, "Cryostat for synchrotron powder diffraction with sample rotation and controlled gas atmosphere in the sample chamber," *J Appl. Cryst.*, vol. 26, pp. 135-137, 1993.

[89] M. Knapp, V. Joco, C. Baehtz, H. H. Brecht, A. Berghaeuser, H. Ehrenberg, H. v. Seggern, and H. Fuess, "Position-sensitive detector system OBI for high resolution X-ray powder diffraction using on-site readable image plates " *Nuclear Instruments and Methods in Phys. Research A*, vol. 521, pp. 565-570, 2004.

[90] M. Knapp, C. Baehtz, H. Ehrenberg, and H. Fuess, "The synchrotron powder diffractometer at beamline B2 at HASYLAB/DESY: status and capabilities," *J. Synchrotron Rad.*, vol. 11, pp. 328-334, 2004.

[91] J. Rodriguez- Carvajal, "Fullprof. A program for Rietveld Refinement and pattern matching analysis," 2000.

[92] B. V. Laar and W. B. Yelon, "The peak in Neutron powder diffraction," *J. Appl. Cryst.*, vol. 17, pp. 47-54, 1984.

[93] L. W. Finger, D. E. Cox, and A. P. Jephcoat, "A correction for powder diffraction peak assymetry due to axial divergence," *J. Appl. Cryst.*, vol. 27, pp. 892-900, 1994.

[94] L. W. Finger, "PROFVAL: Functions to calculate powder-pattern peak profiles with axial divergence asymmetry," *J. Appl. Cryst.*, vol. 31, p. 111, 1998.

[95] P. W. Stephens, "Phenomenological model of anisotropic peak broadening in powder diffraction," *J Appl. Cryst.*, vol. 32, pp. 281-289, 1999.

[96] D. Hennings and H. Pomplun, "Evaluation of Lattice Site and Valence of Mn and Fe in Polycrystalline $PbTiO_3$ by Electron Spin Resonance and Thermogravimetry," *J. Am. Ceram. Soc.*, vol. 57, pp. 527-530, 1974.

[97] R. A. Eichel, "Defect structure of oxide ferroelectrics-valence state, site of incorporation, mechanisms of charge compensation and internal bias fields," *J. Electroceram.,* vol. 19, pp. 9-21, 2007.

[98] J.-Y. Kim, C.-R. Song, and H.-I. Yoo, "Mn-doped $BaTiO_3$: Electrical Transport Properties in Equilibrium State," *J. Electroceram.,* vol. 1, pp. 27-39, 1997.

[99] S.-M. Lee, S.-H. Lee, C.-B. Yoon, H.-E. Kim, and K.-W. Lee, "Low-temperature sintering of MnO_2-doped PZT–PZN Piezoelectric ceramics," *J. Electroceram.,* vol. 18, pp. 311-315, 2007.

[100] H. Nagata, N. Koizumi, N. Kuroda, I. Igarashi, and T. Takenaka, "Lead-Free Piezoelectric Ceramics of $(Bi_{l/2}Na_{l/2})TiO_3$-$BaTiO_3$-$BiFeO_3$ System," *Ferroelectrics,* vol. 229, pp. 273-278, 1999.

[101] X.-J. Li, Q. Wang, and Q.-L. Li, "Effects of MnO_2 addition on microstructure and electrical properties of $(Bi_{0.5}Na_{0.5})_{0.94}Ba_{0.06}TiO_3$ ceramics," *J. Electroceram.,* vol. 20, pp. 89-94, 2008.

[102] G. Fan, W. Lu, X. Wang, and F. Lian, "Effects of manganese additive on piezoelectric properties of $(Bi_{1/2}Na_{1/2})TiO_3$–$BaTiO_3$ ferroelectric ceramics," *J. Mater Sci,* vol. 42, pp. 472-476, 2007.

[103] G. Li, L. Zheng, Q. Yin, B. Jiang, and W. Cao, "Microstructure and ferroelectric properties of MnO_2-doped bismuth-layer $(Ca,Sr)Bi_4Ti_4O_{15}$ ceramics," *J. Appl. Phys.,* vol. 98, 2005.

[104] M. Hirose, T. Suzuki, H. Oka, K. Itakura, Y. Miyauchi, and T. Tsukada, "Piezoelectric properties of $SrBi_4Ti_4O_{15}$ based ceramics," *Jpn. J. Appl. Phys.,* vol. 38, pp. 5561-5563, 1999.

[105] V. V. Klimov, N. I. Selikova, and A. N. Bronnikov, "Effect of MnO_2, Bi_2O_3, and ZnO Additions on the Electrical Properties of Lead Zirconate Titanate Piezoceramics," *Inorganic Materials,,* vol. 42, pp. 573-577, 2006.

[106] S. Tashiro, K. Ishii, and T. Wada, "Fabrication of $(Sr_xK_{0.5-x}Na_{0.5-x})NbO_3$ Pizoelectric Ceramics and Effects of MnO Addition on Their Piezoelectric Properties," *Jpn. J. Appl. Phys.,* vol. 45, pp. 7449-7454, 2006.

[107] N. M. Hagh, B. Jadidian, E. Ashbahian, and A. Safari, "Lead-Free Piezoelectric Ceramic Transducer in the Donor-Doped $K_{1/2}Na_{1/2}NbO_3$ Solid Solution System," *IEEE-UFFC Transactions,* vol. 55, pp. 214-224, 2008.

[108] M. Guo, K. H. Lam, D. M. Lin, S. Wang, K. W. Kwok, H. L. W. Chan, and X. Z. Zhao, "A Rosen-type piezoelectric transformer employing lead-free $K_{0.5}Na_{0.5}NbO_3$ ceramics," *J Mater Sci,* vol. 43, pp. 709-714, 2008.

[109] B. C. Tofield and W. R. Scott, "Oxidative Nonstoichiometry in Perovskites, an Experimental Survey ; the Defect Structure of an Oxidized Lanthanum Manganite by Powder Neutron Diffraction," *J. Sol. Stat. Chem.,* vol. 10, pp. 183-194, 1974.

[110] L. Bellaiche, J. Íñiguez, E. Cockayne, and B. P. Burton, "Effects of vacancies on the properties of disordered ferroelectrics: A first-principles study," *Phys. Rev. B,* vol. 75, 2007.

[111] Y. Hou, M. Zhu, F. Gao, H. Wang, B. Wang, H. Yan, and C. Tian, "Effect of MnO_2 Addition on the Structure and Electrical Properties of $Pb(Zn_{1/3}Nb_{2/3})_{0.20}(Zr_{0.50}Ti_{0.50})_{0.80O3}$ Ceramics," *J. Am. Ceram. Soc.,* vol. 87, pp. 847-850, 2004.

[112] Y. Guo, K.-i. Kakimoto, and O. Hitoshi, "Phase transitional behavior and piezoelectric properties of $Na_{0.5}K_{0.5}NbO_3$–$LiNbO_3$ ceramics," *Applied Physics Letters,* vol. 85, pp. 1-3, 2004.

[113] M. Matsubara, K. Kikuta, and H. S., "Piezoelectric properties of $(K_{0.5}Na_{0.5})(Nb_{1-X}Ta_X)O_3$ - $K_{5.4}CuTa_{10}O_{29}$ ceramics," *J. Appl. Phys.,* vol. 97, 2005.

[114] E. Hollenstein, M. Davis, D. Damjanovic, and N. Setter, "Piezoelectric Properties of Li and Ta modified $(K_{0.5}\ Na_{0.5})NbO_3$ Ceramics," *Appl. Phys. Lett,* vol. 87, 2005.

[115] H. E. Mgbemere, R. P. Herber, and G. A. Schneider, "Investigation of the dielectric and piezoelectric properties of potassium sodium niobate ceramics close to the phase boundary at $(K_{0.35}Na_{0.65})NbO_3$ and partial substitutions with lithium and antimony," *J. Eur. Ceram. Soc.,* vol. 29, pp. 3271-3276, Dec 2009.

[116] I. Smeltere, M. Dambekalne, M. Livinsh, M. Dunce, and A. Mishnov, "Influence of Monoxides Addition on Sintering of Sodium-Potassium Niobates Solid Solution," *Integrated Ferroelectrics,* vol. 102, pp. 69-76, 2008.

[117] R. Zuo, J. Fu, D. Lv, and Y. Liu, "Antimony Tuned Rhombohedral-Orthorhombic Phase Transition and Enhanced Piezoelectric Properties in Sodium Potassium Niobate," *J. Am. Ceram. Soc.,* vol. 93, pp. 2783-2787, 2010.

[118] W. D. Kingery, "Plausible Concepts Necessary and Sufficient for Interpretation of Ceramic Grain-Boundary Phenomena: I I, Solute Segregation, Grain-Boundary Diffusion, and General Discussion," *J Am. Ceram. Soc.,* vol. 57, pp. 74-83, 1974.

[119] W. D. Kingery, "Plausible Concepts Necessary and Sufficient for Interpretation of Ceramic Grain-Boundary Phenomena: I, Grain-Boundary Characteristics, Structure, and Electrostatic Potential," *J Am. Ceram. Soc.,* vol. 57, pp. 1-8, 1974.

[120] H. Du, D. Liu, F. Tang, D. Zhu, and Z. Wancheng, "Microstructure, Piezoelectric, and Ferroelectric Properties of Bi_2O_3-Added $(K_{0.5}Na_{0.5})NbO_3$ Lead-Free Ceramics," *J. Am. Ceram. Soc.*, vol. 90, pp. 2824-2829, 2007.

[121] Y. L. Wang, A. K. Tagantsev, D. Damjanovic, and N. Setter, "Giant domain wall contribution to the dielectric susceptibility in BaTiO3 single crystals," *Applied Physics Letters*, vol. 91, Aug 2007.

[122] R. Suzuki, S. Uraki, H. Kakemoto, S. Wada, and T. Tsurumi, "Fabrication and piezoelectric properties of $(K_{0.5}Na_{0.5})NbO_3$-based ceramics doped with Bi-perovskites," *IEEE ISAF 2007*, vol. 1, pp. 649-650, 2007.

[123] J. Roedel, W. Jo, K. T. P. Seifert, E.-M. Anton, T. Granzow, and D. Damjanovic, "Perspective on the Development of Lead-free Piezoceramics," *J. Am. Ceram Soc.*, vol. 92, pp. 1153-1177, 2009.

[124] H. Du, W. Zhou, F. Luo, and D. Zhu, "Perovskite lithium and bismuth modified potassium-sodium niobium lead-free ceramics for high temperature applications," *Appl. Phys. Lett*, vol. 91, 2007.

[125] M. L. Dunn and M. Taya, "Electromechanical Properties of Porous Piezoelectric Ceramics," *J. Am. Ceram Soc.*, vol. 76, pp. 1697-1706, 1993.

[126] Y. Wang, Y. Li, K. Kalantar-zadeh, T. Wang, D. Wang, and Q. Yin, "Effect of Bi^{3+} ion on piezoelectric properties of $K_xNa_{1-x}NbO_3$," *J. Electroceram.*, vol. 21, pp. 1-4, 2007.

[127] P. Zhao, B.-P. Zhang, and J.-F. Li, "Enhancing piezoelectric d_{33} coefficient in Li/Ta-codoped lead-free $(Na,K)NbO_3$ ceramics by compensating Na and K at a fixed ratio," *Appl. Phys. Lett*, vol. 91, 2007.

[128] H. Du, F. Luo, S. Qu, Z. Pei, D. Zhu, and W. Zhou, "Phase structure, microstructure, and electrical properties of bismuth modified potassium-sodium niobium lead-free ceramics," *J. Appl. Phys.*, vol. 102, p. 054102, 2007.

[129] Y. H. Hu, H. M. Chan, Z. X. Wen, and M. P. Harmer, "Scanning Electron Microscopy and Transmission Electron Microscopy Study of Ferroelectric Domains in Doped $BaTiO_3$," *J. Am. Ceram. Soc.*, vol. 69, pp. 594-602, 1986.

[130] K. A. Schoenau, L. A. Schmitt, M. Knapp, H. Fuess, R.-A. Eichel, H. Kungl, and M. J. Hoffmann, "Nanodomain structure of $Pb[Zr_{1-x}Ti_x]O_3$ at its morphotropic phase boundary: Investigations from local to average structure," *Phys. Rev. B*, vol. 75, 2007.

[131] Y. Guo, K.-i. Kakimoto, and H. Ohsato, "Phase transitional behavior and piezoelectric properties of $(Na_{0.5}K_{0.5})NbO_3$–$LiNbO_3$ ceramics," *Appl. Phys. Lett.*, vol. 85, pp. 4121-4123, 2004.

[132] P. Zhao, B.-P. Zhang, and J.-F. Li, "High piezoelectric d_{33} coefficient in Li-modified lead-free (Na,K)NbO_3 ceramics sintered at optimal temperature," *Appl. Phys. Lett*, vol. 90, 2007.

[133] H. Du, W. Zhou, F. Luo, and D. Zhu, "An approach to further improve piezoelectric properties of $(K_{0.5}Na_{0.5})NbO_3$-based lead-free ceramics," *Appl. Phys. Lett*, vol. 91, 2007.

[134] X. Sun, J. Deng, J. Chen, C. Sun, and X. Xing, "Effects of Li Substitution on the Structure and Ferroelectricity of (Na,K)NbO_3," *J. Am. Ceram. Soc.*, vol. 92 pp. 3033–3036, 2009.

[135] H. E. Mgbemere, G. A. Schneider, and T. A.Stegk, "Effect of antimony substitution for niobium on the crystal structure, piezoelectric and dielectric properties of $(K_{0.5}Na_{0.5})NbO_3$ ceramics," *Funct. Mat. Lett.*, vol. 3, pp. 25-30, 2010.

[136] T. A. Skidmore, T. P. Comyn, and S. J. Milne, "Temperature stability of $([Na_{0.5}K_{0.5}NbO_3]_{0.93}–[LiTaO_3]_{0.07})$ lead-free piezoelectric ceramics," *Appl. Phys. Lett.*, vol. 94, 2009.

[137] H. E. Mgbemere, R. P. Fernandes, M. Hinterstein, and G. A. Schneider, "Temperature-dependent synchrotron powder diffraction phase studies of $(K_{0.37}Na_{0.52}Li_{0.03})(Nb_{0.87}Ta_{0.1}Sb_{0.03})O_3$ ferroelectric ceramics," *Z. Kristallogr.*, vol. 226, pp. 138-144, 2011.

[138] N. W. Thomas, "A Re-examination of the Relationship Between Lattice Strain, Octahedral Tilt Angle and Octahedral Strain in Rhombohedral Perovskites," *Acta Cryst.*, vol. B52, pp. 954-960, 1996.

[139] N. Zhang, A. M. Glazer, D. Baker, and P. A. Thomas, "Structures of $K_{0.05}Na_{0.95}NbO_3$ (50–300 K) and $K_{0.30}Na_{0.70}NbO_3$ (100–200 K)," *Acta Cryst.*, vol. B65, pp. 291-299, 2009.

[140] P. Zhao, B.-P. Zhang, and J.-F. Li, "Influences of Sintering Temperature on Piezoelectric, Dielectric and Ferroelectric Properties of Li/Ta-Codoped Lead-Free (Na,K)NbO_3 Ceramics," *J. Am. Ceram. Soc.*, vol. 91, pp. 1690-1692, 2008.

[141] U. Robels, J. H. Calderwood, and G. Arlt, "Shift and deformation of the hysteresis curve of ferroelectrics by defects: An electrostatic model," *J. Appl. Phys.*, vol. 77, pp. 4002-4008, 1995.

[142] D. C. Lupascu and U. Rabe, "Cyclic Cluster Growth in Ferroelectric Perovskites," *Phys. Rev. Lett.*, vol. 89, p. 187601, 2002.

[143] B. Noheda, D. E. Cox, G. Shirane, Z.-G. Ye, and J. Gao, "Phase diagram of the ferroelectric relaxor (1-x)$PbMg_{1/3}Nb_{2/3}O_3$-x$PbTiO_3$," *Phys. Rev. B*, vol. 66, pp. 1-10, 2002.

[144] R. D. Shannon, "Revised Effective Ionic Radii and Systematic Studies of Interatomie Distances in Halides and Chaleogenides," *Acta Cryst.*, vol. A32, pp. 751-767, 1976.

[145] T. Mitsui and W. B. Westphal, "Dielectric and X-ray studies of $Ca_xBa_{1-x}TiO_3$ and $Ca_xSr_{1-x}TiO_3$," *Phys. Rev.* , vol. 124, pp. 1354-1359, 1961.

[146] S. Zhang, R. Xia, and T. R. Shrout, "Lead-Free Piezoelectric Ceramics vs. PZT?," *J. Electroceram.*, vol. 19, pp. 113-126, 2007.

[147] A. Pramanick, D. Damjanovic, J. E. Daniels, J. C. Nino, and J. L. Jones, "Origins of Electro-Mechanical Coupling in Polycrystalline Ferroelectrics during subcoercive electrical loading," *J. Am. Ceram. Soc.*, vol. 94, pp. 293-309, 2011.

[148] H. E. Mgbemere, R.-P. Herber, and G. A. Schneider, "Effect of MnO_2 on the dielectric and piezoelectric properties of alkaline niobate based lead free piezoelectric ceramics," *J. Eur. Ceram. Soc.*, vol. 29, pp. 1729-1733, 2009.

[149] D. Damjanovic, "Contributions to the piezoelectric effect in ferroelectric single crystals and ceramics," *J. Am. Ceram. Soc.*, vol. 88, pp. 2663-2676, 2005.

[150] A. M. Glass, M. E. Lines, K. Nassau, and J. W. Shiever, "Anomalous dielectric behavior and reversible pyroelectricity in roller-quenched $LiNbO_3$ and $LiTaO_3$ glass," *Appl. Phys. Lett.*, vol. 31, pp. 249-251, 1977.

[151] M. J. Hoffmann, H. Kungl, J.-T. Reszat, and S. Wagner, "Characterization of PZT-Ceramics by High-Resolution X-Ray analysis," in *Polar oxides*, R. Waser, U. Boettger, and S. Tiedke, Eds. Weinheim: Viley-VCH, 2004, pp. 137-150.